UV nanoimprint lithography for fabrication of 1-D photonic crystal slabs and their application in OLEDs

Christian-Albrechts-Universität zu Kiel

Faculty of Engineering

Dissertation

Zur Erlangung des akademischen Grades Doktor der Ingenieurwissenschaften (Dr.-Ing.) der Technische Fakultät der Christian-Albrechts-Universität zu Kiel

Arfat Pradana

Kiel, May 2014

1. Gutachterin : Prof. Dr. Martina Gerken
2. Gutachter : Prof. Dr. Hermann Kohlstedt

Datum der mündlichen Prüfung: 23. July 2014

Abstract

Organic light-emitting diode (OLED) technology is developing and emerging rapidly since its introduction in 1987. In an OLED device, the light generated from the recombination process may internally reflect in the substrate and be waveguided either in the organic film or high refractive index oxide that serves as an anode. These optical phenomenona reduce the amount of the light exiting the device. One method to increase the efficiency is by embedding periodically nanostructured 1-D photonic crystal slabs into the OLED device. One-dimensional photonic crystal slabs (Bragg gratings) allow the extraction of waveguide modes in OLED devices. This dissertation employs ultraviolet nanoimprint lithography (UV-NIL) technology to fabricate 1-D photonic crystal slabs made from high refractive index hybrid nanoparticles-photoresist. High refractive index hybrid nanoparticles-photoresist is a blend of pristine UV-NIL photoresist with TiO_2 NP. As an alternative approach, dry etching technique is performed to transfer the UV-imprinted nanostructure to the Ta_2O_5 film.

Hybrid nanoparticles-photoresist is characterized by thickness, surface morphology, and optical characteristics. The thickness increased as a function of TiO_2 NP results for identical spincoat parameters. Surface characterization shows the imprint ability still remains to the pristine photoresist for up to 30% NP content. Optical characterization results are fitted using the Swanepoel method. As a result, the refractive index of hybrid nanoparticles-photoresist containing 30% TiO_2 is 1.869 at 552 nm wavelength. One-dimensional photonic crystal slabs made from hybrid nanoparticles-photoresist 0%, 3%, and 30% are integrated with a rigid planar OLED device. The emission spectrum from the Bragg grating made from hybrid nanoparticles-photoresist 30% shows an additional extraction mode. This mode depends on the emission angle. For grating periodicity of 370 nm, the effective refractive index in the device is 1.59 at 591.8 nm wavelength. The study also demonstrates the use of hybrid nanoparticles-photoresist 30% in flexible OLEDs. The results show that hybrid nanoparticles-photoresist is also successful in extracting the waveguide mode from the devices. Here, the emission characteristic is recorded while the device is under bending conditions. It suggests that geometrical changes in the films due to mechanical loads under bending conditions may alter the emission characteristics.

Acknowledgments

In this page, I would like to express my gratitude to all those who gave me the possibility to complete this PhD theses.

I would like to thank sincerely Prof. Dr. Martina Gerken for giving me the opportunity to work in her group. I really appreciated her guidance through the whole research work. In the mean time, I was encouraged to transfer my idea in the research work into practice.

Thank you so much to Dr. Michael Rädler and Dr. Jürgen Mikat for supervising my work.

Many thanks to Sigrid Thielbörger, Jülf Buschmann, and Janine Greve for making this work group more colorful. In the time that I have to face German burocracy, they helped me and gave some hint how to deal on it. Thank you for Jülf and Janine for their support in the clean room and laboratory. In the lunch time, you guys always made the atmosphere comfortable. Last but not least, I would like to thank them by forcing to improve my german language skill.

I would like to thanks Matthias Burmeister for his work in design, solution, and fabrication. It is impossible to do the experiment without his work.

Many thanks to Dr. Ing. Philipp Metz for programming simulation in Matlab and helping me to construct my wardrobe at home. Christian Kluge for his assistance in theories, discussions, and simulations. Our research assistants, Matthias Bremer and Sarah Schauer, for preparing my samples. Daniela Threm, Dr. Jost Adam, Torben Karrock, Sabrina Jahns, and Hendrik Block for a nice talk either in the lunch or coffee time.

I would like to thank my dear wife Citrasari Handayani Pradana for her support, encouragement, and patient during the difficult time and reminding me to stay focused to finish this PhD.

Many thanks to Nando Budhiman family for spending a lot of time to chat and did activities together.

I would like to thank my parents and parents in law for giving pray and support to finish my PhD and survive in Germany.

Finally, I would like to express my gratitude to all the people and friends whom I cannot

mention in this acknowledgments part for their help and advice during this PhD.

List of publications and other contributions

1. A. Pradana, C. Kluge, and M. Gerken. Nanostructured, ITO-free electrodes for OLED emission control. *MRS Proceedings*, 1699, 2014

2. A. Pradana, C. Kluge, and M. Gerken. Tailoring the refractive index of nanoimprint resist by blending with TiO_2 nanoparticles. *Optical Materials Express*, Vol. 4, Issue 2, pp. 329-337, 2014

3. D. Threm, J. L. Gugat, A. Pradana, M. Rädler, J. Mikat, M. Gerken. Self-aligned Integration of Spin-coated Organic Light-Emitting Diodes and Photodetectors on a Single Substrate. *IEEE Photonics Technology Letters*, Vol. 24, No. 11, pp. 912 - 914, 2012

4. C. Kluge, M. Rädler, A. Pradana, M. Bremer, P. Jakobs, N. Barié, M. Guttmann, M. Gerken. Extraction of guided modes from organic emission layers by compound binary gratings. *Optics Letters*, Vol. 37, Iss. 13, pp. 2646 - 2648, (2012)

5. M. Hansen, M. Ziegler, H. Kohlstedt, A. Pradana, M. Rädler, M. Gerken. UV capillary force lithography for multiscale structures. *J. Vac. Sci. Tech. B*, 30(3), 031601 (2012)

6. C. Kluge, P. Metz, A. Pradana, Y. Nazirizadeh, M. Rädler, M. Gerken. Influence of waveguide thickness on the angular color impression of nanostructured organic emission layers. *Proc. 16th European Conference on Integrated Optics*, Sitges 2012

7. A. Pradana, C. Kluge, M. Bremer, M. Rädler, M. Gerken. Multiperiod gratings in a high refractive index material for enhanced OLED outcoupling. *Renewable Energy and the Environment Congress*, Austin, TX, USA (2 -3 November 2011).

8. D. Threm, Y. Nazirizadeh, A. Pradana, M. Rädler, J. Mikat, M. Gerken. Integrated organic optoelectronic system for refractometric measurements. *Proc. 16th International Conference on Optical MEMS and Nanophotonics* - OMN 2011, Istanbul

9. A. Pradana, D. Threm, M. Rädler, M. Gerken. Integration of two different spin-coated optoelectronic devices on a single substrate. *Proc. International Symposium Technologies for Polymer Electronics - TPE 10*, Rudolstadt 2010 (2010)

Contents

List of Figures

List of Tables

Chapter 1

Introduction

1.1 Motivation

Since it was introduced 26 years ago by Tang and Vanslyke [1] and become popular, OLED technology has been developing and emerging rapidly. The OLED active stacks has a thickness of about 100-200 nm, on average, a thousand times thinner than a human hair. An OLED device has a total thickness of some millimeters, practically 100% of which comprises the support (substrate) and the encapsulation structure. It is a self-emitter, i.e., it does not require a background light. For the same brightness as that of the best inorganic light emitter on the market, it consumes much less energy, and it is also more efficient and has a viewing angle nearing 170° [2]. The most promising application of this technology is for the purposes of lighting and displays. For display technology, the advantages mentioned above may allow it to replace LCD technology and permit fabrication on a thinner substrate and with a high viewing angle. In lighting applications, the performance of white light OLEDs has greatly increased, from 4 lumens per watt (LPW) in 2001 to 100 LPW [3, 4].

Research and development around the world is focused on understanding the fundamental process and especially on the improvement of the efficiency and lifespan of the OLED itself. Increased efficiency can be obtained with an increase in internal and external efficiency. Internal efficiency focuses on material and electronic properties such as recombination of holes and electrons, the ratio of electron and hole concentrations, the effect of the cathode, electron quenching, etc. On the other hand, external efficiency focuses on the optical properties, such as effects of absorption or reflection from the device to light generated from the recombination process. As reported in [5], the light coming out of the device is only 20%, while the rest is internally reflected in the substrate and waveguided in the organic film. One of the techniques used to increase external efficiency is to sandwich one dimensional photonic crystal slabs that have nanostructures on wavelength scale between the OLED and glass substrate [5, 6].

1.2 Aim of this thesis

This work is a further development of the previous study mentioned above [5, 6] by employing 1-D photonic crystal slabs to enhance the external efficiency of OLEDs. The difference lies in the fabrication technology. In this work, ultraviolet nanoimprint tech-

nology (UV-NIL) was used to fabricate 1-D photonic crystal slabs. This technology offers simplicity in replicating the structure defined in the master stamp and later transferred to the photoresist. The structure is covered in a relatively large surface area. The illustration of my primary goal is illustrated in figure 1.1a. The integration of 1-D photonic crystal slabs into OLEDs may be successfully achieved by UV-NIL technology. However, the refractive index of the photoresist is approximately equal to the one of the materials covering it. Therefore, effect of the nanostructures disappears. In this condition, 1-D photonic crystal slabs failed to increase the OLED's external efficiencies. To solve this problem, the 1-D photonic crystal slabs should have a refractive index contrast to the covering materials.

Figure 1.1b illustrates two proposals to solve the problem. First, one may transfer the structure in the resist to the higher refractive index material by dry etching technique. In this study, Ta_2O_5 film was chosen. Ta_2O_5 has a high refractive index (n = 2.1) [6]. The second method is to blend high refractive index TiO_2 nanoparticles (NP) into pristine photoresist. This blend is called hybrid NP-photoresist. The advantage of this technique is not only that it is fast but also straightforward compared to the dry etching method. This method may have great potential to reduce fabrication costs. Figure 1.1c illustrates the integration of hybrid NP-photoresist into OLEDs. The illustration describes that a hybrid NP-photoresist can be integrated for rigid OLEDs as well as the flexible ones.

1.3 Organization of this thesis

This dissertation is organized into 8 chapters including the current one.

Chapter 2 discusses basics of fabrication equipment, theoretical concepts of organic semiconductors and fundamentals of Organic Light Emitting Diodes (OLEDs). This chapter includes the achievements of external efficiency enhancement for OLED devices from previous studies. One of the techniques to increase external efficiency is integrating 1-D photonic grating slabs into OLED devices. This technique becomes the basis of the current dissertation.

Chapter 3 discusses the materials that are used in this work. Substrate, anode, organic emitter, and cathode are selected. These architectures later become my standard OLED devices. A selection of Ultraviolet Nanoimprint Lithography (UV-NIL) resist becomes important. Therefore, an ITO-free OLED device on top of a coated UV-NIL resist glass was fabricated. This result became one of the reasons to choose AMONIL as an UV-NIL resist and was used throughout the study.

Chapter 4 discusses the fabrication of photonic crystal slabs by UV-NIL and dry etching. Two different working stamps in UV-NIL technique are demonstrated. One employs glass and the other is an elastomeric mold as a working stamp. Not only working stamps but also UV-NIL photoresist are applied in this chapter. This chapter also demonstrates a structure transfer to the Ta_2O_5 film by dry etching technique. Surface characteristics are recorded by Atomic Force Microscopy (AFM).

Chapter 5 demonstrates the photoresist refractive index is change to the higher value

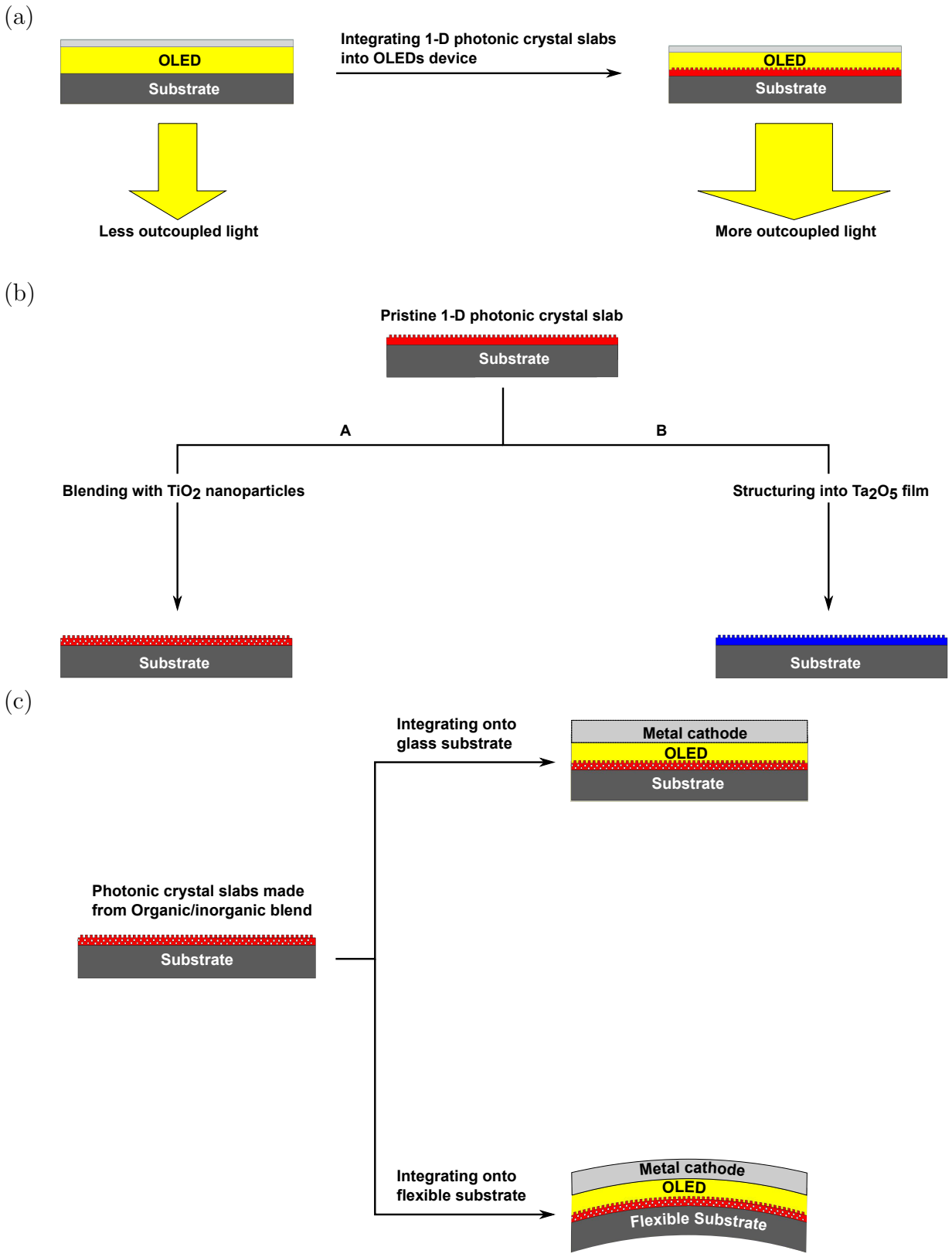

Figure 1.1: The illustration of the whole work. a) The main aim of this work. Integration of 1-D photonic crystal slabs into OLEDs for external efficiency enhancement. b) Two methods to obtain high refractive index 1-D photonic crystal slabs. Blue structure illustrates 1-D photonic crystal slabs in Ta_2O_5 film. Red-white dots structure illustrates hybrid photoresist-NP. c) The application of hybrid photoresist-NP in OLED device. This material is suitable for rigid and flexible OLEDs.

by blending TiO_2 nanoparticles (NP) into the photoresist. In this thesis, the mixture is called hybrid photoresist-NP. The changes in the refractive index are indicated by shifts in the transmission spectrum behavior. The transmission spectrum is later determined by Swanepoel simulation to reveal its optical characteristics. Apart from this, the ability to form in UV-NIL still remains. The surface morphology is characterized by AFM.

Chapter 6 demonstrates the application of high refractive index hybrid photoresist-NP to increase the external efficiency of an OLED. Here, an ITO-free OLED is fabricated onto 1-D photonic grating slabs made from pristine photoresist and hybrid photoresist-NP on top of the glass substrate. The emission characteristic is then recorded using a goniometer. For the purpose of comparison, ITO-free OLEDs are fabricated onto flat pristine photoresist and hybrid photoresist-NP. In this study electroluminescence (EL) and photoluminescence (PL) techniques are employed.

Chapter 7 demonstrates other applications of hybrid photoresist-NP. Hybrid photoresist-NP allows the fabrication of 1-D photonic grating slabs onto flexible substrate. The measurement conditions for flexible grating OLEDs are described in detail in this chapter. The 1-D photonic crystal deformation under mechanical load is predicted using a combination of bending theory and transfer matrix simulation. The theoretical calculation predicts the effective refractive index for TE_1 mode as well as the theoretical extraction angle. The theoretical extraction angle shows good agreement with the experimental data conducted for electroluminescence (EL) and photoluminescence (PL) results. The deviation of the theoretical resonance extraction wavelength as a function of central deflection for a fixed extraction angle of 25° and the experimental values are of a reasonable value. The shift of the extraction wavelength for a given central deflection is shown.

Chapter 8 is the conclusion of this PhD work. In this chapter, the challenges in UV-NIL technique to replicate the structure, the selection of UV-NIL photoresist, the replication transfer of 1-D photonic crystal slabs to Ta_2O_5 film by dry etching technique, and the integration to rigid and flexible OLED devices are summarized.

Chapter 2

Theoretical and experimental basis

Summary

This chapter discusses the basic theories of the fabrication and characterization techniques used in this PhD dissertation. The fundamentals of organic semiconductor and organic light-emitting diodes are explained in this chapter. The previous studies pertaining to OLED efficiency enhancement are summarized in this chapter. Earlier studies employing 1-D photonic crystals slabs to increase OLED external efficiency have formed the basis of the present dissertation.

2.1 Fabrication techniques

2.1.1 Spin coating

The spincoat technique has been the standard method for applying thin film deposition for several decades [7]. The steps are presented in figure 2.1: First, on the oxide surface a UV sensitive photoresist is deposited. It is dispensed on the static substrate lying on the spinner holder. The substrate is held in place by a vacuum chuck. During the dispensing step, it is recommended that the fluid is spread over the substrate at a low rotation speed, typically 500 rpm. It is then accelerated to high rotation speeds to approach the desired thickness. The final film thickness is defined by the combination of selected spin speed and time. The solution flows to the edges because of the centrifugal force at the selected speeds. The resulting polymer thickness, T, as a function of spin speed, solution, concentration, and molecular weight (measured by intrinsic viscosity) is expressed in [7]:

$$T = \frac{KC^{\beta}\eta^{\gamma}}{\omega^{\alpha}} \tag{2.1}$$

where

K = the overall calibration constant.

C = the polymer concentration in g/100 mL solution.

η = the intrinsic viscosity.

ω = the number rotation per minute.

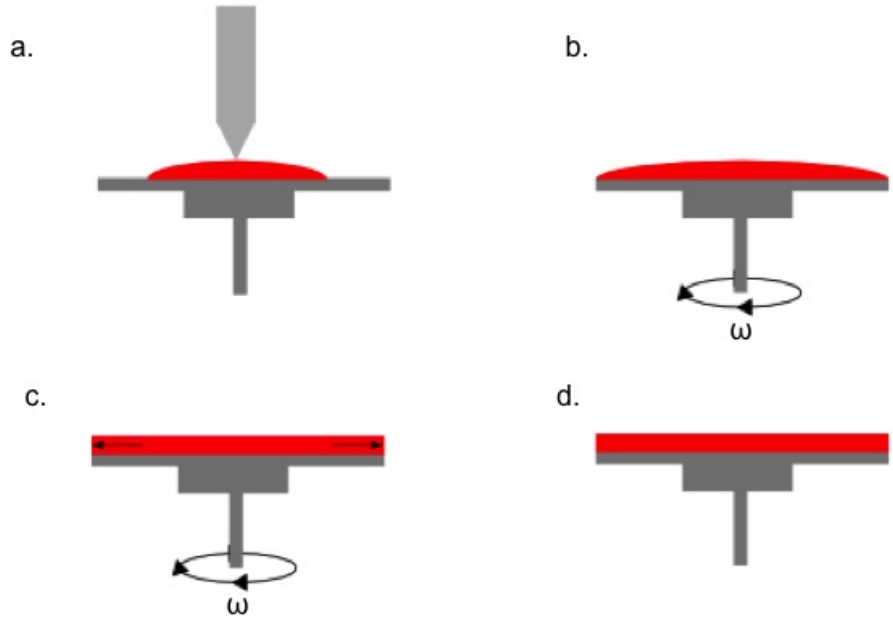

Figure 2.1: Spin coating stages: Dispense (a), Spread cycle (b), Spin cycle (c), Final film thickness (d). [7]

Once the various exponential factors (α, β, and γ) have been determined, equation 2.1 can be used to predict the thickness of the film that can be spun for various molecular weights and solution concentrations of a given polymer and solvent system [7].

2.1.2 UV-nanoimprint lithography

Photolithography and e-beam lithography (EBL) have become crucial techniques for surface pattern technique. However, both techniques are expensive and limited in resolution for optical lithography. Alternatively, Chou's group developed an inexpensive and high output technique, called Nanoimprint lithography in 1995. Nanoimprint lithography is able to replicate 3-Dimension and wide-area structures from nanometer to micrometer scale. It has great potential in OLED, LED, flexible display, and optical devices [8].

2.1.3 Thin film deposition by evaporation

Evaporation is part of the Physical Vapor Deposition (PVD) technique that remove atoms from the source using thermal.

The equation for the rate of evaporation [9]:

$$\Phi_e = \frac{\alpha_e N_A (P_e - P_h)}{\sqrt{2\pi M R T}} \tag{2.2}$$

where Φ_e is the evaporation flux in the number of atoms (or molecules) per unit area per unit time, and α_e is the coefficient of evaporation, which has a value between 0 and 1.

When $\alpha_e = 1$ and P_h is zero, maximum evaporation is realized. The expression for the maximum value of Φ_e is

$$\Phi_e = 3.513 \times 10^{22} \frac{P_e}{\sqrt{MT}} \qquad molecules.cm^{-2}.sec^{-1} \tag{2.3}$$

when P_e is expressed in torr, a useful variant of this formula is

$$\Gamma_e = 5.834 \times 10^{-2} \sqrt{\frac{M}{TP_e}} \qquad g.cm^{-2}.sec^{-1} \tag{2.4}$$

where Γ_e is the mass evaporation rate. At a pressure of 10^{-2} torr, a typical value of Γ_e for many elements is approximately 10^{-4} g.cm^{-2}.sec^{-1} of evaporant. Temperature is the key variable that affects the rate of evaporation, which greatly affects the equilibrium vapor pressure. Resistance-heated evaporation and electron-beam evaporation are widely used in the laboratory. Contamination, reaction, or alloy of the evaporant by the heater should be avoided. During evaporation, the heater should not release any gases such as nitrogen, hydrogen, or oxygen. Evaporation sources are available in tungsten wire, refractory metal sheet, sublimation furnace and crucible [9].

2.1.4 Dry etching in general

As explained in great detail in Madou et al. [7], etching is widely used as a substractive technique for micromachining after the lithography steps. Etching can be defined as pattern transfer by the chemical/physical removal of a material from a substrate. A pattern usually defined by a resist or an oxide. Dry etching is also commonly used for differentiating between chemical plasma etching (PE), reactive ion etching (RIE), and physical ion-beam etching (IBE).

A desired etched profile can be generated in single crystalline, polycrystalline, and amorphous materials for the dry etching process. It requires careful consideration to achieve the etched profile and the selectivity of the process. The selectivity refers to the etch rate differences between the mask and the film to be etched, which is controlled by plasma conditions [7].

2.2 Characterization Techniques

2.2.1 Atomic Force Microscopy (AFM)

According to Friedbacher [10], Atomic Force Microscopy (AFM) is a member of the group of scanning force microscopy (SFM) techniques. The working principles are based on the interaction of different forces between the sample surface and a sharp tip. The interaction may be caused by van der Waals, magnetic, electrostatic, repulsive, and attractive forces

Figure 2.2 shows the measurement setup. In this figure, the interaction of different forces has been measured via deflection of a soft cantilever while the tip is scanning across the surface. Later, the interaction force as a function of surface area produces the image.

The interaction between the tip and sample can be described by force-distance curves as shown in figure 2.3 [10]. If the distance is large, the interaction and the observed

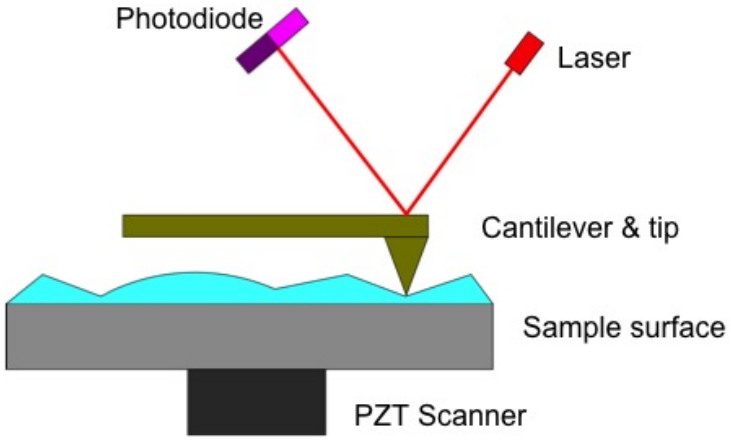

Figure 2.2: AFM Instrumentation. [11]

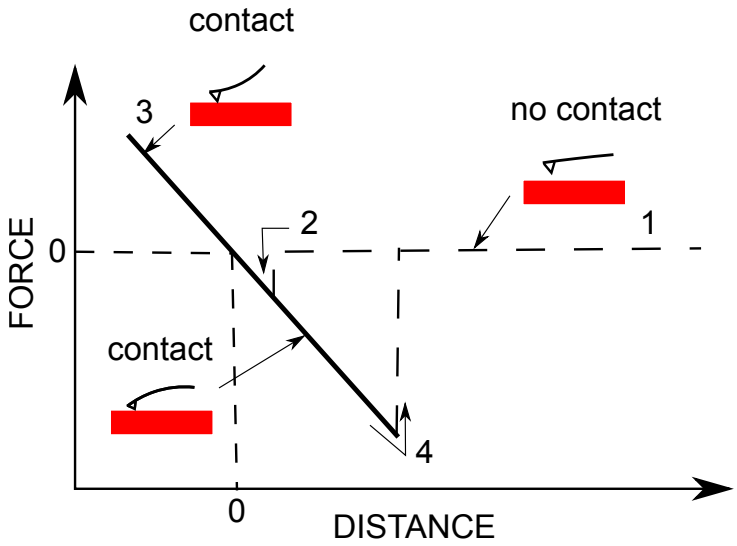

Figure 2.3: Force-distance curve depicting the interaction of the AFM tip with the sample surface. The operation range of the AFM is between points 3 and 4. [10]

force is zero. At point 2, the attraction force made the tip jump into contact mode. The attraction force is caused by van der Waals interactions. If the sample moved further toward to the tip, a repulsive force dominates. The repulsive force is reduced as the sample is retracted along the line 3 to 4. The cantilever experienced attractive force because of adhesion between the tip and the surface. This situation is indicated in the diagram below the zero force line. At point 4, the adhesion force and the cantilever load are balanced. When the sample is further retracted, the tip may flip off the surface. An ideal setup in contact mode is to set the force along the curve between point 3 and 4, but in order to minimize the contact force it should be closer to 4 [10].

The surface topography can be analyzed by region analysis and line analysis. It is characterized by maximum peak to valley (R_{p-v}), the root mean square roughness (R_{rms}) and the average roughness (R_{ave}): [12] R_{p-v}: It gives the maximum peak to valley (p-V) distance within the selected area. R_{p-v} is given by the highest data point in a mask minus the lowest point:

$$R_{p-v} = z_{max} - z_{min} \tag{2.5}$$

R_{rms}: The root mean square roughness, given by the standard deviation of the data. It is determined using the standard definition:

$$R_{rms} = \sqrt{\frac{\sum_{n=1}^{N}(z_n - \bar{z})^2}{N-1}} \tag{2.6}$$

where $\bar{z}$ is the mean z height. R_{ave}: The average roughness given by the average deviation of the data, referenced to the average of the data within the included area.

$$R_{ave} = \sum_{n=1}^{N} \frac{|z_n - \bar{z}|}{N} \tag{2.7}$$

where $\bar{z}$ is the mean z height. N is given by the number of data points in the selected areas.

2.2.2 UV-Vis spectroscopy

UV-Vis spectroscopy is a device that allows the characterization of optical properties of thin film in the range from near infrared to ultraviolet [13]. Figure 2.4 explains the device's working principle schematically.

In order to avoid significant error caused by lamp drift during long time measurement, dual beam spectrophotometers have been used. A chopper is fixed in the optical path close to the light source. The chopper adjusts the light path between a reference and a sample optical path to the detector. The rotation speed alternate the measurements of blank and sample several times per second, thereby reducing drift effects [14]. Once the beam passed through or was reflected from a sample, the amount of transmitted radiation (I) was different from the incidence radiation (I_0) due to absorption. Transmittance is defined in the following equation [14] and usually a fraction of 1 or a percentage is given.

$$T = \frac{I}{I_0} \quad \text{or} \quad \%T = \frac{I_o}{I} \times 100 \tag{2.8}$$

Absorbance is defined as follows:

$$A = -log \quad T \tag{2.9}$$

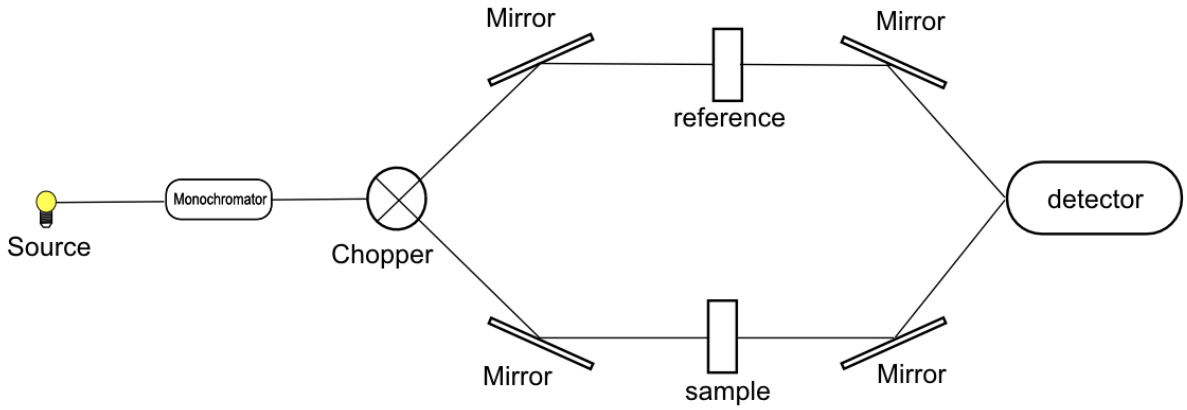

Figure 2.4: An illustration of UV-vis working principle. [14]

2.2.3 Goniphotometer

In this work, the sample was mounted onto a goniometer that allows an object to be rotated to a precise angular position. This technique was used to analyze the scattered emission intensity as a function of angle due to 1-D photonic crystal slabs that were planted in the OLED device. Emission characterizations were carried out using electroluminescence (EL) and photoluminescence (PL) techniques. A current flow was connected to the device for EL measurement, while PL was obtained by injecting UV laser with a wavelength of 405 nm into the sample. The emitting light passed through a polarizer. After that, the light propagates through the optic fiber that was connected to the spectrometer. The characterization principle can be seen in figure 2.5:

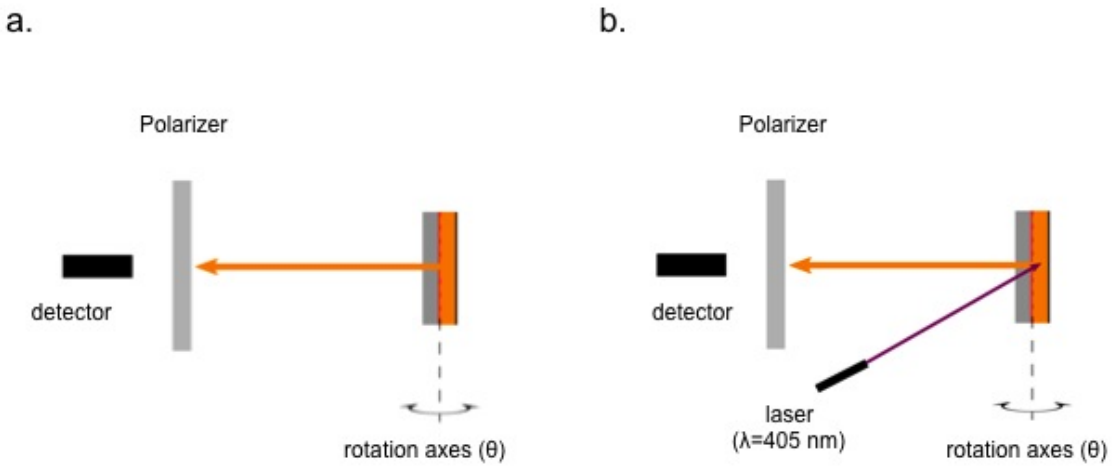

Figure 2.5: OLED's emission characterization using goniometer. Two techniques were employed: electroluminescence (a) and photoluminescence(b).

2.3 Organic Semiconductor

There are two classes of organic semiconductors: polymers and low molecules materials. In general, both have conjugated π-electron system being assembled by the p_z-orbitals of p^2 C atoms that hybridized in the molecules. The π bonding is weaker compared to the σ bonds. This class of materials absorb and emit light in the visible spectral range. The energy gap is around 1.5 to 3 eV citebrutting. The processes for forming thin film of both

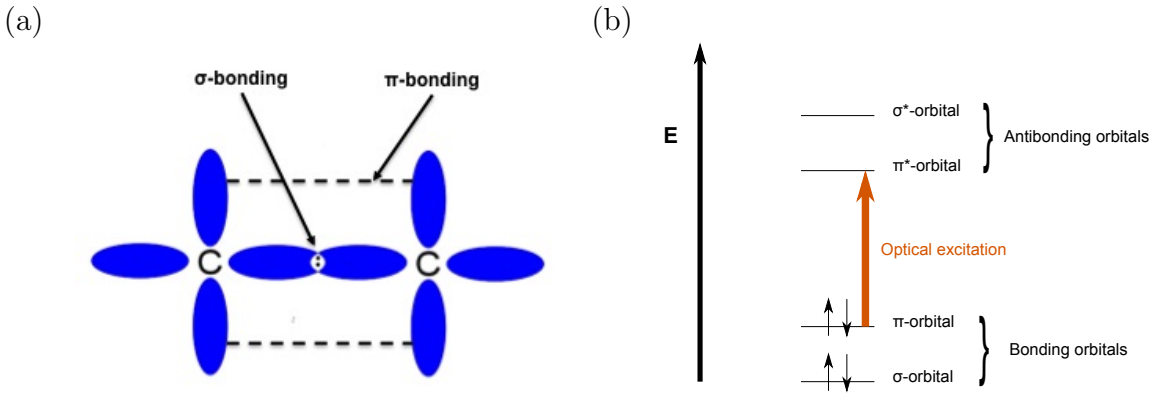

Figure 2.6: An ethene that has σ and π-bonds, as an example of the simplest conjugated π electron system (a). The right side shows the energy level of π-conjugated molecule (b). The nearest electronic excitation is from the π bonding orbital to the π^* antibonding orbital. [15]

classes of materials are significantly different. The evaporation or sublimation technique in an ultra high vacuum chamber is very common for low molecular weight materials deposition, while the spincoating and printing technique can only be used for conjugated polymers [15]. Klessinger et al. [16] explain the photophysical processes by Jablonski diagram. Figure 2.7 schematically displays the singlet ground state S_0, the excited singlet states S_1 and S_2 as well as the triplet states T_1 and T_2 [16].

The emission or luminescence referred to as fluorescence depends on a spin-allowed transition, while phosphorescence is the result of a spin-forbidden transition. Internal conversion (IC) and intersystem crossing (ISC) are known as radiationless transitions. [16]. From figure 2.7 a molecule may be excited to the vibrational level of the electronically excited state S_1 either by the absorption of a sufficient photon energy or by internal conversion from one of the vibrational levels of a higher electronic state such as S_2. Fluorescence is a result of molecules that returning from the zero-vibrational level of the S_1 state to the ground state S_0. Phosphorescence, on the other hand, is a result of molecules in S_1 experiencing intersystem crossing (ISC) to reach the triplet state T_1, before returning to the ground state S_0 after losing excess vibrational energy [16]. Fluorescence lifetime is typically in the nanosecond range, while phosphorescence may remain for several seconds [17].

2.3.1 Energy Transfer

Energy transfer refers to a photophysical process whereby the excitation energy of an excited donor (D) moves to acceptor (A) [18]. This process can occur by either a non-radiative process or a radiative process and is typically thermodynamically spontaneous.

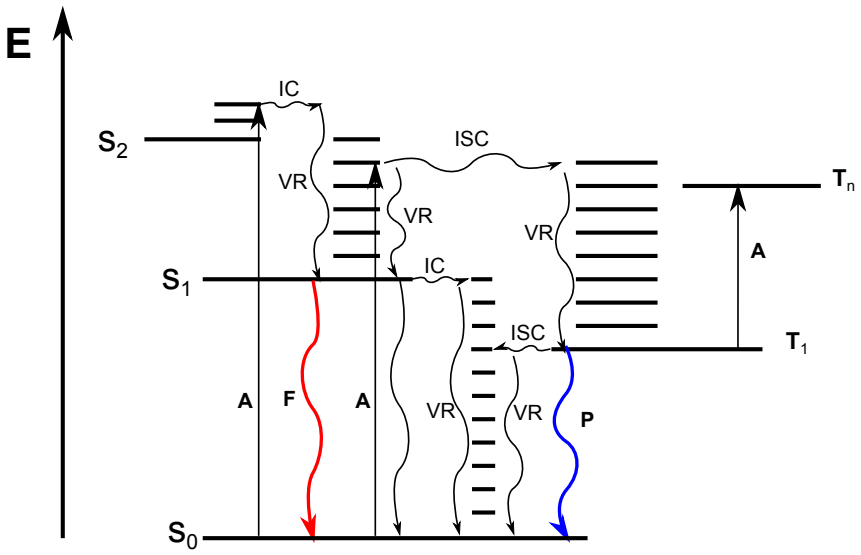

Figure 2.7: Jablonski diagram. Absorption (A) is determined by straight arrows, emission processes fluorescence (F) and phosphorescence (P) by red and blue wavy arrows, radiationless process by sinuous arrows (IC = internal conversion, ISC= intersystem crossing, VR =vibrational relaxation). [16]

Within a unimolecular system, including macromolecules and one-dimensional polymer systems, this process is called electronic energy migration [18]. Electronic excitation is also called exciton [18]. An electron is excited into a conduction band from the valence band and leaves a hole behind when a semiconductor absorbs light. An exciton is mobile in a homogeneous one-dimensional system, resulting in a 'hopping' of the exciton state among identical particles with equal energy rather than localizing on one chromophore. Therefore, energy migration can also be called 'exciton migration' or 'exciton hopping' [18]. Organic semiconductors have two non-radiative energy transfer mechanisms: Förster and Dexter transfer [18]. The Förster transfer is non-radiative, long range ($\simeq 40\mathring{A}-100\mathring{A}$), dipole-dipole coupling of donor (D) and acceptor (A) molecules [19]. The Dexter transfer process, conversely, is a short-range one. Here the diffusion of excitons from D to A sites is driven by intermolecular electron transfer [20]. As presented in figure 2.8, the Förster mechanism only transfers energy to the singlet state of the acceptor molecule because the transition from the ground to the excited state is allowed for both D and A species [16].

2.3.2 Interfacial Electronic Structure

An interface of two solid materials can be formed either by contact of two solids or the deposition of one material onto another solid surface. In this condition, an adjustment of energy level at the interface and band bending in the organic-metal layer may occur citeIshii. Figure 2.9 illustrates metal and organic band energy level alignment at the interface as both materials come into contact. In this system, a dipole film may be formed right at the interface, originating in a variety of chemical reactions between the interface such as, electron cloud redistribution, charge transfer across the two different phases, and any types of electronic charge. This phenomena is explained in detail by Ishii et al. [22]. Ishii et al. suggest that for an interface with a thick organic layer, band bending should

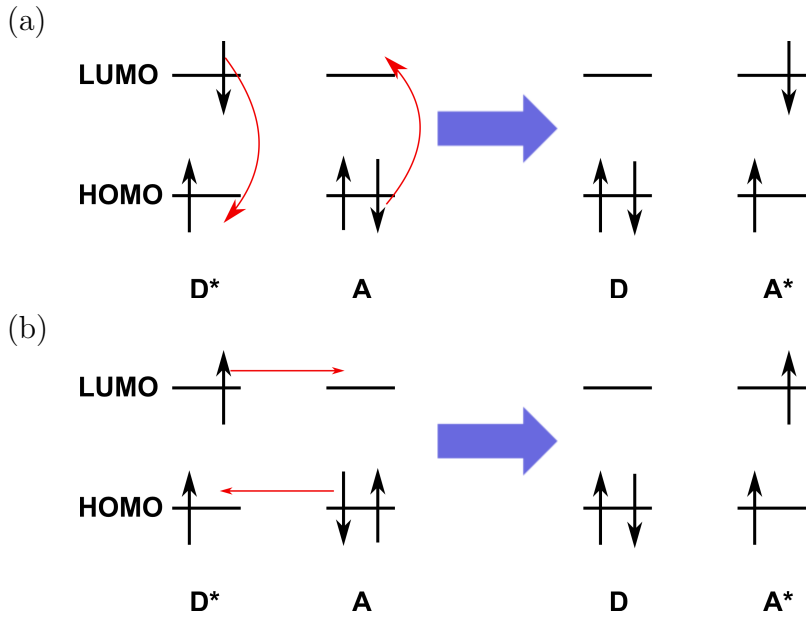

Figure 2.8: Non-radiative energy transfer. Förster (a) and Dexter (b) transfer mechanism. [21]

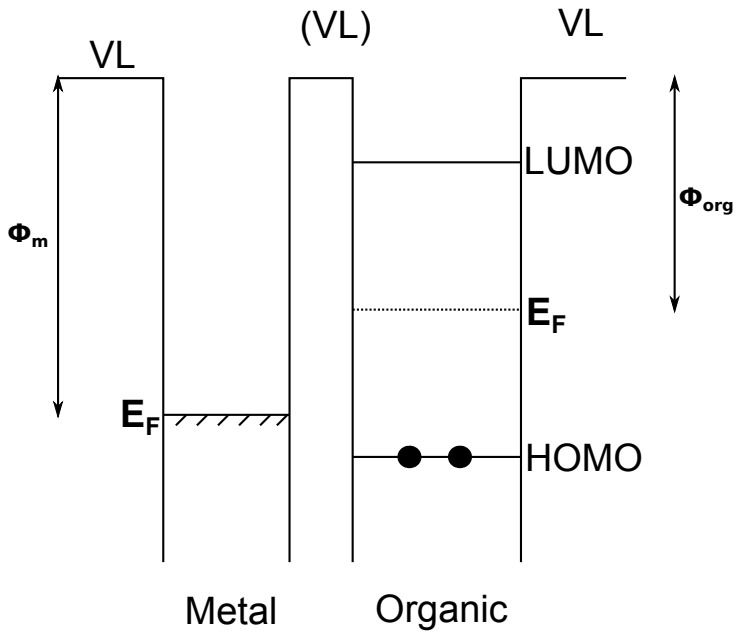

Figure 2.9: Interface band diagram as both metal and organic semiconductors come into contact. ϕ_m and ϕ_{org} denote metallic and organic work function, respectively. VL is abbreviated as vacuum level and (VL) means the virtual vacuum level at the interface. [22]

also be considered [18]. In general, work functions for the metal and organic layers are different, and the interfaces are not in electrical equilibrium where the Fermi levels would be at the same energy. In figure 2.9, the metal work function is larger than the organic layer, and metal is more favorable to the electron. As a result, some electrons may move from organic to the metal layer, leading to positive and negative charging of the organic and the metal layer, respectively [22]. This charging makes the metal less comfortable for the negatively charged electron. Mobile charge carriers may redistribute in the organic layer. This flow and distribution of charge continues until the Fermi levels are aligned between the metal and the bulk of the organic layer as presented in figure 2.10 [22].

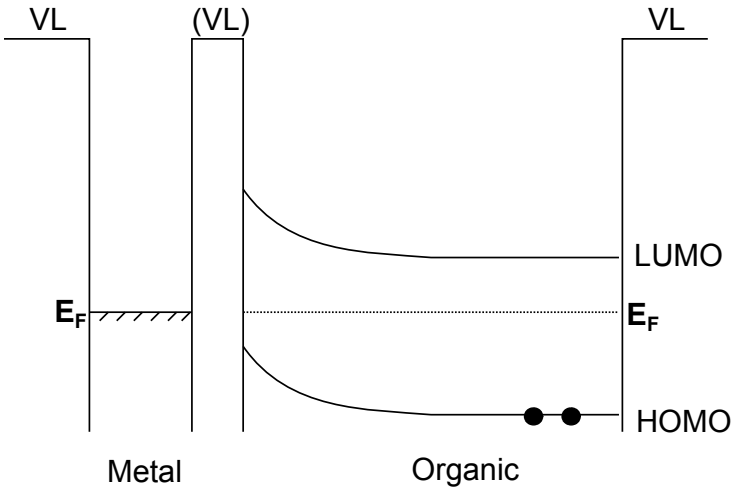

Figure 2.10: The alignment of the metal and organic layer Fermi level leads to the charge redistribution in the organic layer to achieve electrical equilibrium. As a result a band bending in the organic layer occurs. [22]

2.4 Organic Light Emitting Diodes

Electroluminescence (EL) in organic semiconductors results from the electrically driven emission of light. The selection of EL material for OLED becomes crucial because of limitation factors such as charge injection and transport, for determining operating voltages and luminance efficiency. In organic light-emitting diodes (OLEDs), injection produces the hole current, and the electron current is formed by the presence of the traps in metal-organic interactions [23]. A phosphorescent emitter via triplet-triplet energy transfer was chosen and applied in order to increase OLED efficiency [23]. The extraction of emitted light is determined by the device architecture and the refractive indices of layers composition. Increasing extraction efficiency can be made through surface modifications, while the issues of light trapping remains unsolved for display application [23].

2.4.1 Device configuration

Basically, two-layer OLED structure is sandwiched by two electrodes. As illustrated in figure 2.11, one organic layer serves as the hole-transport layer (HTL), transporting holes, and the other as the electron-transport layer (ETL), transporting electrons. The

location to facilitate an efficient recombination site of the injected electron-hole pair is in the interface between two organic layers. In this location electroluminescence appears [23]. As different electrical potential is applied to the anode and the cathode, the injected holes take place from the anode to the HTL. At the meantime, electrons are repelled into the ETL from the cathode. The heterojunction design should allow holes to move from HTL into ETL and block electrons on the opposite side, thereby increasing the probability of recombination and exciton formation in the emission interface region [23].

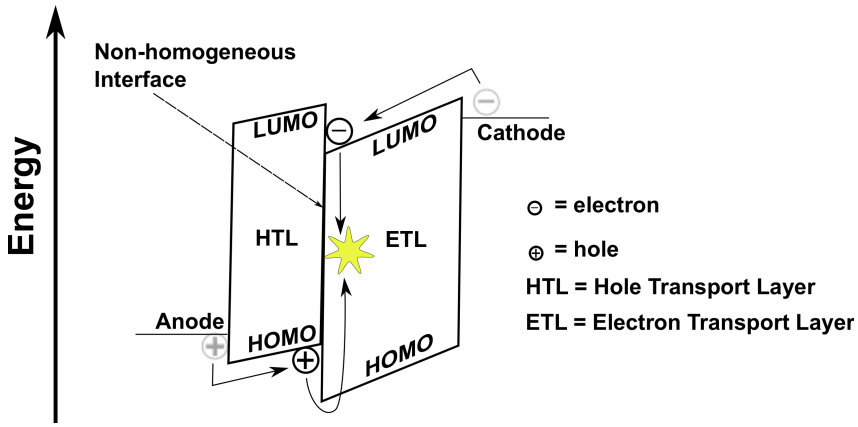

Figure 2.11: Recombination process in OLEDs heterojunction system. HOMO stands for Highest Occupied Molecular Orbital whereas LUMO is abbreviated from Lowest Unoccupied Molecular Orbital [23].

2.4.2 Organic materials

As explained in 2.4.1, OLED efficiency depends on the heterojunction design [24] which follows the implementation of the doped emitter employing high fluorescent organic polymers for color adjustment and efficiency improvement [24, 1]. Further research regarding the architectures and material development has been established to enhance OLED efficiency. Material development includes:

Emitters. The use of low molecular and polymeric electroluminescent materials [25, 26, 27, 28] is very common. Widely used for low molecular emitter is Alq3.

Hole-injection and transport materials. The polymer commonly used for promoting hole injection is PEDOT:PSS (poly(3,4-ethylenedioxythiophene)-poly(styrene)).

Hole-transport materials. Mostly used is NPB [23].

Electron transport materials. An example is Alq_3 [23].

Fluorescent dopants. The discovery of guest-host doped emitter system [29] is one example of progress in the improvement of OLED based display technology. The enhancement in operational stability has been reported in Shi et al. [30] and Baldo et al. reported the improvement of internal efficiency close to 100% [31].

Triplet emitting materials. The invention of electrophosphorescence breaks the maximum limit of the internal quantum efficiency of fluorescent based devices from 25% up to nearly 10% [23]. Such materials were proposed by Baldo et al. [32] and O'Brien et al. [33].

2.4.3 External quantum efficiency

Various loss mechanisms in OLEDs need to be considered in order to understand and, therefore, maximize efficiency. Carriers that do not recombine are considered the first loss process. This factor is commonly referred to as the charge balance, defined as γ. The second is excitons that are formed into singlets that have radiative decay and triplets that decay through nonradiative processes. The ratio of singlets and triplets is referred to as r_{st}. Luminescence efficiency due to the exciton quenching mechanism is considered the third loss (q). Finally, a large amount of the light generated in the OLED device is unable to escape, referred to optical outcoupling ($\eta_{coupling}$) [34]. Therefore, the external quantum efficiency (η_{ext}) is determined from these four major losses and expressed in equation 2.10 [34]:

$$\eta_{ext} = \gamma \times r_{st} \times q \times \eta_{coupling} \tag{2.10}$$

whereas the equation may be simplified as:

$$\eta_{ext} = \eta_{internal} \times \eta_{coupling} \tag{2.11}$$

Charge balance. As discussed earlier in the 2.4.1 section, the following processes can describe the basic principle of operations of an OLED. Holes and electrons are injected into HOMO and LUMO levels of the organic layer. Once the charges enter the organic layer, they move under the presence of the applied electric field, pass through the device or recombine to form neutral excitons and undergo radiative recombination generating photons with an energy determined by the energy difference between the energy of the excited state and the ground state of the molecule. Ideally, under voltage bias, the maximum quantum efficiency is satisfied if the mobility of the two carriers is identical and there is no barrier from the metal into polymer layer for the injected charge. Excluding any interaction of the charges and the excitons with the electrodes, this condition would produce the maximum charge balance and, therefore, the maximum efficiency achievable [34]. However, barriers are mostly present at metal and polymer interface, and the mobility of the two carriers in organic semiconductors is barely matched [34].

Singlet and triplet ratio. The emission process of OLEDs involves the recombination of injected electrons and injected holes, which forms one of two types of states; singlets and triplets. An important distinction of these two states is that singlets can relax radiatively. In triplet states the process is forbidden, therefore the relaxation process is non-radiative. Simple spin statistics suggest that the ratio of singlets to triplets is 1:3, although studies have shown that this is not applicable in polymeric materials [35, 34].

Luminescence efficiency. The competition between radiative and nonradiative decay processes is of fundamental importance in OLEDs, since it is directly related to the device efficiency. The photoluminescent quantum efficiency is a measure of this ratio, which can vary significantly for different materials. A typical value is 40% for polymer devices but this can rise to above 80% for some polymers and small molecules. In addition to this intrinsic photoluminescent efficiency of the emissive material, there are a number of additional factors that lead to further reduction in the luminescent efficiency, which

are discussed in more detail by Patel et al. [34].

The reduction of luminescent efficiency in OLED devices may be caused by impurities in the organic layer. It may be caused by diffusion process from the metal electrodes into the organic layer and the internal reaction between excitons and the metal electrodes. One example, a metal like Ca can diffuse from the cathode, interact with the polymer, and remain inside the film in the Ca^{2+} form [36, 37].

Optical output coupling. A great deal of research work has been done to increase OLED's internal efficiency ($\eta_{internal} = \gamma \times r_{st} \times q$). Surface modification on the anode, Indium Tin Oxide (ITO), using plasma treatment [38, 39], employing high work function polymer onto ITO [40, 41], electron injection from cathode into polymer LUMO level using low work-function metals or alloy [34, 42] and utilizing phosphorescence materials [17, 31, 32] have all been investigated. All this work may increase internal efficiency, $\eta_{internal}$, close to 100% [43, 44] but it is still not enough to achieve high external efficiency because of an optical output coupling factor. The emitted light from organic films is propagating at the air-film interface because of internal reflection. It may be scattered as edge emission. This is one of the main explanations that addresses why OLEDs luminous power efficiency remains low [23].
OLED architecture typically build in a multilayer sandwich of a transparent substrate made from glass ($n_{sub} = 1.51$), a layer of transparent anode, i.e. ITO ($n_{ITO} = 1.9$), an organic layer ($n_{sub} = 1.6 - 1.8$), and a metal cathode. The index of refraction is refered as n. The contrast in the refractive indices of the polymer and the air leads to a total internal reflection (TIR). In this situation, light propagated in high refractive index material that is surrounded by low refractive index materials [23]. Figure 2.12 illustrates internal reflection of rays in the planar OLED system. Light emitted from the organic layer may escape to the air at an angle less than organic-air critical angle, θ_1, given by $sin^{-1}(n_{air}/n_{org})$. Light is propagated in the substrate when the emitted light has angle larger than θ_1 but smaller organic-substrate critical angle, θ_2, given by $sin^{-1}(n_{sub}/n_{org})$. Light will propagate in the organic and conductive oxide layers when the angle of emitted light is larger than θ_2 and immediately absorbed in conductive oxide or cathode layer [45]. A loss at the metal cathode due to surface plasmon polaritons might also occur [46]. In order to figure out the modes distribution of emitted light and to simulate the effects of conductive oxide film thickness and the refractive indices of the substrate, a quantum mechanical microcavity theory has been established as a base model [47].

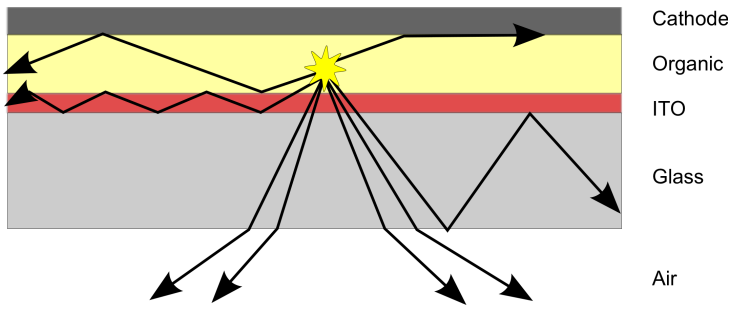

Figure 2.12: Ilustration of optical losses in planar OLED.

Enormous efforts have been made to reduce external optical loss. One is by using

micro-cavities to alter the EL characteristics of organic materials which have been studied by several groups [48, 49, 50, 51, 52, 53]. Another approach involves using substrate modification techniques such as surface roughening [34], employing square glass mesas with truncated right circular cone [54], spherical shape [45, 55], high refractive index substrate [47, 56], luminaire [57], substrate structuring surface by means of arrays with small lenses and pyramids and scattering layers [58], and photonic crystals and nano-cavities [59]. These techniques are presented in figure 2.13 below.

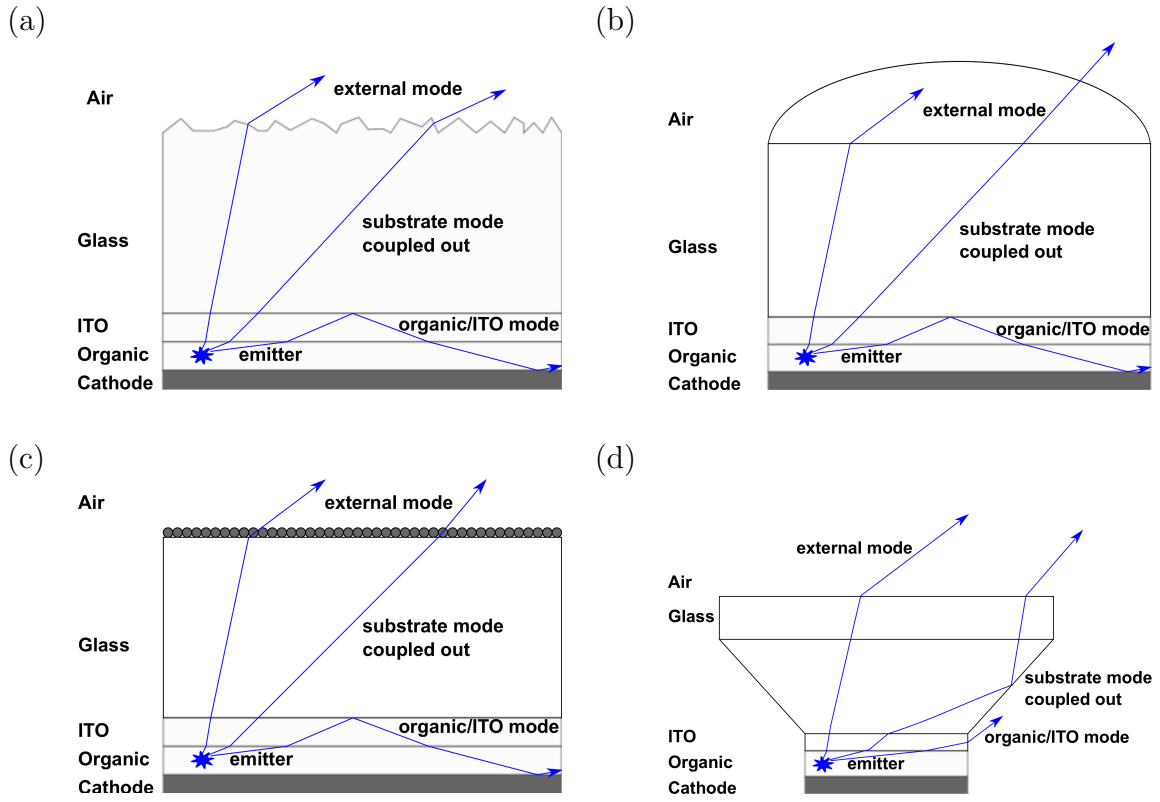

Figure 2.13: OLEDs substrate modification. a) Substrate roughening, b) Half sphere attached onto glass substrate, c) Silica microspheres, d) Shaped mesa. [34]

2.5 Photonic structures in OLEDs : background and previous work

The introduction of periodic structures on the wavelength scale is implemented to control the photonic density of states. The periodic structures alter the interaction of light with the matter [60]. The fabrication process of the photonic structure with a sufficient contrast in refractive indices between photonic structures and OLED devices becomes a significant problem [61]. As shown schematically in 2.12, only 20% of the emitted light is coupled out to the air, while the remaining light is propagated in the device due to TIR [5]. Some work employing periodic structures on the wavelength scale or 1-D periodic photonic structure to increase OLED external efficiency is reported in [6, 5, 62, 63]. Since the refractive indices of the organic layer in OLED is greater than in glass substrate, the probability of waveguide mode in the organic layer is high. In figure

2.14, waveguide modes are described by their in-plane propagation vector, β, and the polarization of the electric field [63].

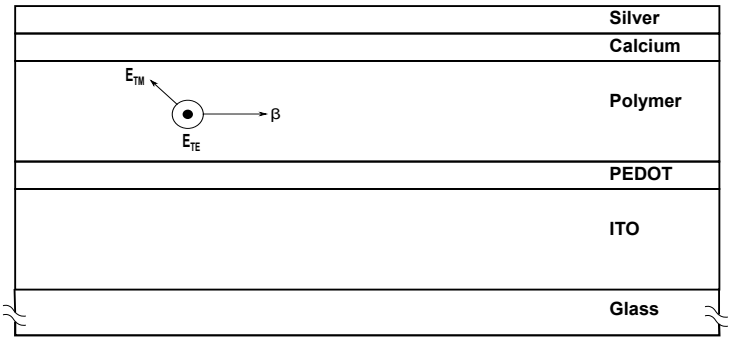

Figure 2.14: The representation of wave vector β, in the OLEDs polymer layer. The two possible electric field polarizations are also shown. [63]

Introducing Bragg grating in the emitting layer allows the waveguide mode to scatter and split as a function of angle. This condition also increases the external efficiency. The angle of the outcoupled emission is given by [63]:

$$k_0 \, sin\theta = \beta \pm ({}^{2\pi m}/_{\bigwedge}) \tag{2.12}$$

The free-space wave vector is indicated by k_0, θ is the angle of extraction to the normal, $\bigwedge$ is 1-D photonic crystal slab (Bragg gratings) periodicity and m is integer of the scattering order. Bragg gratings efficiency to couple out the waveguide mode in the device depends on the Bragg grating location, thickness, and refractive indices of the material layers [63]. The thickness dependency, shown in the experiment by Ziebarth et al. [63], indicates that the variation of the thickness of the emitting layer produces different results.

This PhD work is continuing previous research that employs 1-D photonic structures or Bragg grating using UV-Nanoimprint lithography (UV-NIL) as a fabrication technique. In this work, UV-NIL technology is exploited for structure replication and transfer into different material. The introduction of high refractive index TiO_2 nanoparticles into UV-NIL photoresist may tune the refractive index. This blend is later referred to as hybrid photoresist. Integrating hybrid photoresist into planar OLEDs shows identical results to the previous work [5, 6].

2.6 Flexible OLEDs : background and previous work

The invention of OLED by Tang and VanSlyke [1] allows the fabrication of a thinner display compared to the predecessors such as LCD and CRT technology. The arrival of portable electronic devices has put an increasing premium on durable, lightweight and inexpensive display components. In recent years, research and development of a flexible display technology has emerged rapidly [64]. In parallel to the flexible display, organic light emitting diode (OLED) technology has grown rapidly over the last decade and has become an interesting research topic due to its potential applications in flat panel displays, domestic lighting, etc. Much research has been done on fundamental operation principles, such as internal quantum efficiency (η_{int}) enhancement to external

coupling efficiency (η_{ext}). Some novel approaches have been implemented to improve the external coupling in OLEDs such as substrate modification techniques, scattering medium, micro-lenses, micro-cavity structure, photonic crystals and nano-cavities, surface plasmon, nano-structured films, nano-wires, and nano-particles and aperiodic dielectric mirrors as reported in [59]. As reported in [5], Bragg grating results in different angle intensity as a function of periodicity. Another approach is to employ Bragg gratings with high refractive index materials, Ta_2O_5 (n=2.1), between glass substrate and polymer anode by reason of a differently contrasted refractive index [6]. Both techniques require complex manufacturing route schemes and the production cost is relatively high. Most Bragg gratings for light enhancement purposes have been fabricated on rigid substrate or glass [59, 5, 6]. The development progress is not limited to the rigid substrates only but can also be carried out on flexible substrates. Research and development on flexible substrate OLEDs has been done in some areas. **Anode selection**. The use of brittle materials as anodes in flexible OLED devices, mostly ITO, requires the understanding of mechanical limitations of the materials. As reported in [65, 66, 67], the ITO anode fractured after the stress-strain as well as the bend test. On the contrary, a conductive polymer serving as an anode has shown stable electrical performance even under bending conditions [68]. Therefore, a conductive polymer is recommended as an anode for flexible OLEDs [69, 70]. **Flexible substrate materials**. In [71], a substrate made from a steel foil was used to support top-emitting organic light-emitting diodes (TOLED). But in general, flexible substrates made from plastics are still favorable. In [72], a Polyimide substrate was employed to support flexible OLEDs. In this work, a polycarbonate (PC) has been used as an OLED substrate. It is an ideal candidate since the transmission is above 90% [64] in visible range. Even though the chemical resistance is an issue, the fabrication was successful and no damage was caused by chemicals. **Device enhancement**. In [73], the operation lifetime of OLED devices increased when employing inorganic-organic barrier films. Present flexible OLED displays encounter relatively poor contrast due to a reflective metal electrode at the rear of the stack [74]. Introducing a contrast-enhancing-stack (CES), a circular polarizer (CP), and combining a multilayer dielectric metal anti-reflection (AR) structure on the top semi-transparent cathode [74, 75] was successful in enhancing the device. But so far, light extraction efficiency of flexible OLEDs has only been reported in [76], by employing antireflection nanopillars on Polycarbonate substrate. The antireflection nanopillars structure coupled out the substrate mode in the Polycarbonate.

This PhD work is continuing previous work that employed 1-D photonic structures or Bragg gratings using UV-Nanoimprint lithography (UV-NIL) as a fabrication technique. In this work, the combination of UV-NIL technique and hybrid UV-NIL photoresist allows Bragg gratings fabrication into flexible OLEDs and successfully couples out waveguide modes in the device.

Figure 2.15: A prototype of white flexible OLED lighting panels manufactured by LG chem. [77]

Chapter 3

OLED process compatible with UV-NIL

Summary

This chapter discusses the basic materials for OLED fabrication and investigates its compatibility with UV-NIL photoresist. The materials, such as substrate, anode, emitter and cathode are carefully selected for OLED devices. After careful study of the PhD thesis of Boris [78], an ITO-free OLEDs design is chosen . It is demonstrated that ITO-free OLEDs work properly on UV-NIL photoresist.

3.1 OLED materials

3.1.1 Anode

In this work, a composite film of poly (3,4ethylendioxythiophene):poly(styrenesulfonate) (PEDOT:PSS) served as an anode. PEDOT:PSS is usually deposited on the substrate by spin-coating from waterborne colloidal dispersion in which small discrete particles of PEDOT are prevented from coalescing by surrounding chains of PSS [79]. Optimised PEDOT:PSS is relatively stable in dry environments and has moderately high conductivity for Baytron P formulation [79]. Care must be taken since PEDOT:PSS films are extremely hygroscopic; thermal annealing in an inert environment is therefore necessary [80]. Highly conductive PEDOT:PSS was purchased from Heraeus Clevios GmbH (previously H.C. Starck GmbH) with commercial name Clevios PH500. It has a conductivity of up to 300 S/cm [81] and a refractive index below 1.6 over the entire visible spectrum [82]. The highest occupied molecular orbital (HOMO) and lowest occupied molecular orbital (LUMO) are located around -4.9 eV and -2.4 eV respectively [83, 82, 79, 80].
Additional DMSO into PH500 could also increase the conductivity. As demonstrated by Fehse et. al [82], PEDOT:PSS has potential to substitute ITO in OLEDs. One of the advantages of using PEDOT:PSS as an anode over ITO is the application for flexible OLEDs.

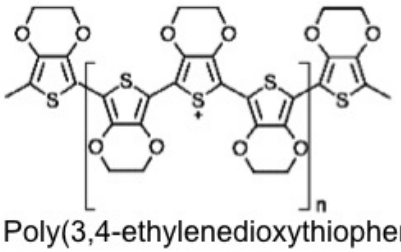

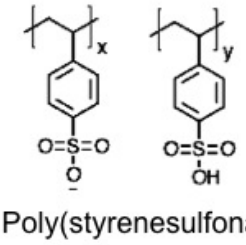

Figure 3.1: Chemical structure of poly (3,4-ethylendioxythiophene)(PEDOT) and poly(styrenesulfonate) (PSS). [81]

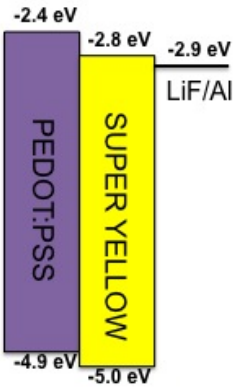

Figure 3.2: OLED's energy level. [78]

3.1.2 Emitter

Emitting layers made from polymer films have made unexpectedly dramatic progress in comparison with classical semiconductor LEDs and have potential to provide an innovative low-cost technology for illumination and display application [84]. A new class of soluble electroluminescent poly(p-phenylenevinylene)s(PPVs) [84, 85], Super Yellow, is used in this work. It exhibits very good solubility in its conjugated state, good mechaninal film forming properties, high molecular weight which improves mechanical stability, and excellent electroluminescence performance [84]. The energy level for HOMO and LUMO is located at 5 eV and 2.8 eV respectively [83]. The emission spectra maximum is located at 550 nm, in the yellow-green color region.

3.1.3 Cathode

EL devices strongly depend on the electron injection process. Therefore, low work function metals and alloys are suitable as the injecting current increases and operational voltages decrease [86, 42]. However, metals that have such properties are always susceptible to atmospheric oxidation if exposed to the atmosphere [86]. Lithium Floride and Aluminum (LiF/Al) is one of the alloys that fulfills the criteria. LiF acts as a tunneling barrier layer since it is an insulating material because of its highest band gap energy. However, in thin film form backed by an Al layer, it becomes an effective electron injector [86]. LiF thickness also affected the performance of EL devices [42]. The work function of LiF/Al alloy is 2.9 eV [87].

3.1.4 Substrate

All OLED substrates used in this work are generally transparent in visible range. They have a dimension of 25 mm x 25 mm x 1 mm. The first substrate is made from Selected White Float glass purchased from Präzisions Glass & Optik GmbH. This type of substrate is used for planar OLEDs. The second substrate is made from Polycarbonate (PC). This type of material is used for flexible OLEDs. All glass substrates are cleaned using acetone and isopropanol for 15 minutes each. They are subsequently dehydrated for 10 minutes at 160 °C to remove the remaining residue on the substrate. This is the standard cleaning process for glass in this work. On the other hand, PC substrates are cleaned using isopropanol for only 15 minutes without any further dehydration process.

3.2 ITO-free OLED on polymer resist

Before patterning photoresist polymer (AMONIL MMS4, AMO GmbH, Germany), its compability with the OLED material was tested. This is a very important step in order to observe whether there is any chemical interaction between AMONIL with PEDOT:PSS that serves as an anode because this might influence the performance of the device. The glass substrate was cleaned using standard procedure, as already mentioned in subsection 3.1.4. An adhesion layer, Amoprime, was spin-coated on the cleaned surface glass substrate at 3000 rpm for 30 seconds and heated at 115 °C on the hotplate for 2 minutes. Afterwards, AMONIL is spin-coated onto the adhesion layer at 3000 rpm for 30 seconds, and the resist is exposed using a 2 J/cm^2 dose of a UV light source (Beltron

GmbH, Rödemark, Germany). The AMONIL layer thickness is 200 nm. Afterwards, 70 nm of anode polymer (PH500 purchased from H.C.Starck) is deposited using spin-coat techniques on the nanostructured polymer. Then, an 80 nm light-emitting layer, PDY-132 (SuperYellow) purchased from Merck OLED Materials GmbH, is spin-coated on the anode polymer. As a cathode, 1 nm LiF and 200 nm Al were deposited using thermal evaporation technique. The OLED's active area is 5 x 5 mm^2. As presented in figure 3.3a, the electrical properties show diode characteristics, and figure 3.3b shows an operated OLED under bias voltage based on presented stacks.

(a) (b)

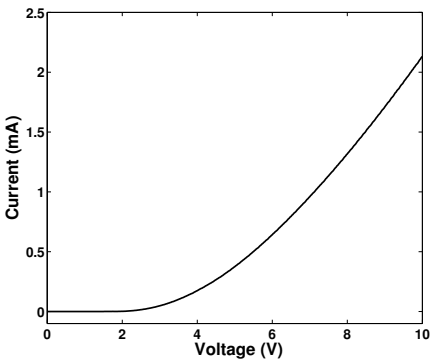

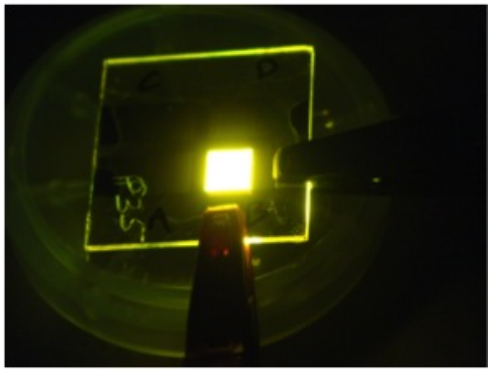

Figure 3.3: An ITO-free OLED fabricated on AMONIL photoresist. a) Electrical characteristic and b) photograph.

The result indicates that this stack performed very well under bias voltage. It is observed that there is no degradation in the device performance unless affected by atmosphere. In this work, AMONIL becomes an important functional material on most of the fabrication steps. Structuring AMONIL into Bragg gratings presents another challenge in this work even though this material is commercially prepared and purposed for UV-nanoimprint technology.

Chapter 4

Photonic crystal slabs: fabrication and dry etching

Summary

This chapter discusses the process of fabrication of 1-D photonic crystal slab structure by UV-NIL technique. In this experiment, two UV- NIL stamps were prepared. A rigid and flexible stamp. A rigid stamp employed by a rigid transparent glass. On the other hand, a flexible stamp is made from an elastomeric polymer, Polydimethylsiloxane (PDMS). Mask aligner (MA-6 from SUSS MicroTec) is the fabrication equipment that was used in this experiment. Two types photoresist specifically for UV-NIL were selected and tested. Challenges and solutions during UV-NIL processes are described in more detail in this section. The next step is to transfer the replica structure obtained from the UV-NIL process to another structure that has a high refractive index employing Reactive Ion Etching (RIE) technique.

4.1 UV-nanoimprint lithography

A glass master stamp, 25 mm x 25 mm x 1 mm in size with 1-D photonic structure (Bragg grating) on the surface was fabricated by laser interference lithography (LIL) in previous work [5]. The master stamp was cleaned using piranha solution (3:1, concentratic H_2SO_4 to 30% H_2O_2 (purchased from Sigma Aldrich, Germany)) for 10 minutes and rinsed thoroughly with DI water and dried with nitrogen gun. Subsequently, the stamp was coated with anti-sticking film, F13-TCS, which is also known as tridecafluoro-(1,1,2,2)-tetrahydrooctyl-trichlorosilane (purchased from Sigma Aldrich, Germany) in the glove box to avoid water contamination, which could react with chlorosilanes that polymerize the material. Therefore, less than 1 ppm of water content in the glove box is necessary. The coating process was carried out in closed glass petri dishes, as illustrated in figure 4.1, at 250 °C for 2 hours. Finally, the master stamp was washed using anhydrous hexane (purchased from Sigma Aldrich, Germany) to prevent polymerization of F13-TCS.

Figure 4.2 shows a coated master stamp bonded onto a reticle glass (65 mm x 65 mm x 5.01 mm in size) using transparent crystal-bond adhesive at 120 °C. This will be referred to as a working stamp. The substrates were cleaned using standard procedure (chapter 3, subsection 3.1.4). Two types of photoresist, specifically for UV-NIL, are

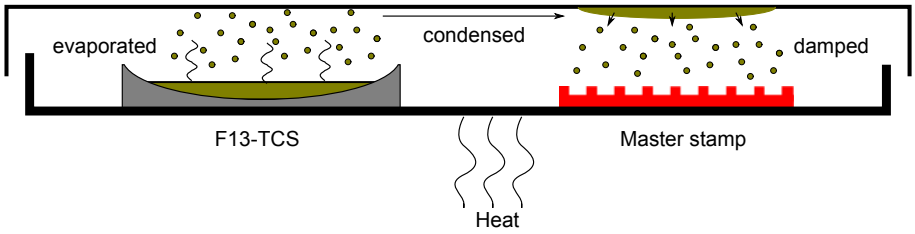

Figure 4.1: Silanization process.

selected and tested in this work. These are mr-UVCur21 (micro resist technology GmbH, Germany) and Amonil (AMONIL MMS4, AMO GmbH, Germany). In order to avoid mr-UVCur21 being torn during the separation process, it is strongly recommended to deposit adhesion promoter (mr-APS1) onto the glass surface prior to mr-UVCur21. For AMONIL photoresist, the adhesion promoter is Amoprime. Each photoresist will be deposited onto clean surface glass using parameters that is given the table 4.1 for mr-UVCur21 and table 4.2 for AMONIL.

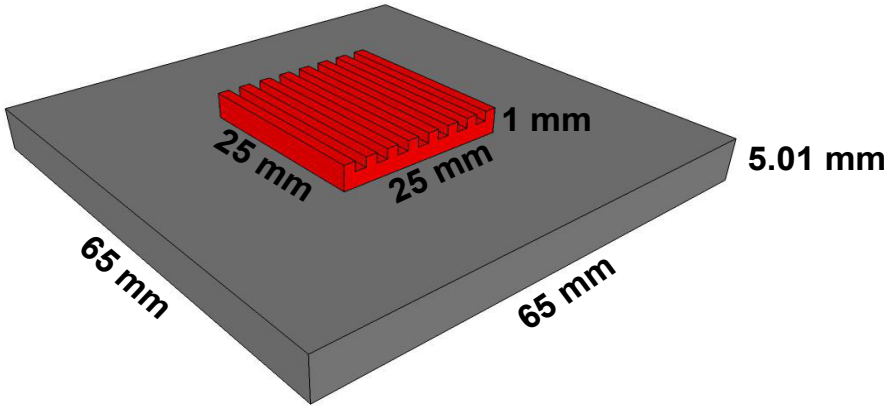

Figure 4.2: Working stamp glass.

recipe:	mr-APS1	mr-UVCur21
spin speed/time	5000 rpm / 60 sec	3000 rpm / 60 sec
softbake/time	150 °C / 60 sec	80 °C / 60 sec
Exp. Dose	-	700 mJ/cm^2 @ 320-420 nm

Table 4.1: mr-APS1 and mr-UVCur21 parameters

The printing process is illustrated on figure 4.3a. The replica shows inhomogeneity on the surface even after an anti-sticking layer is applied onto the glass stamp. This is presented on figure 4.3b. This phenomenon occurred frequently in both photoresists. During the printing step, it was observed that Newton's ring appeared between the working stamp and the resist coated onto glass substrate. Newton's ring occurs because of the interference pattern caused by the thin film of air formed between the working stamp and resist coated glass substrate. This phenomenon still appeared frequently during the printing

recipe:	Amoprime	Amonil
spin speed/time	3000 rpm / 30 sec	3000 rpm / 30 sec
softbake/time	115 °C / 2 min	-
Exp. Dose	-	2 J/cm^2 @ 320 nm

Table 4.2: Amoprime and Amonil parameters

process; even after numerous printing parameters in MA-6 were applied (appendix A.3). Therefore, it is concluded that the surface flatness differences between the working stamp and the sample substrate are obvious. As a result, the UV-NIL reproducibility is very low. Learning from this result, a flexible working stamp is proposed and demonstrated in order to compensate for the surface flatness differences of the working stamp and the coated substrate. In this way, the Newton's ring that builds up from the air film could be avoided and a wide area replicated structure delivered.
A transparent elastomeric polymer called Polydimethylsiloxane (PDMS) was chosen because of its well-known properties and ability to perform UV-NIL [88, 89, 90, 91, 92]. The PDMS precursor (Sylgard 184, Dow Corning) was blended with a curing agent at a ratio of 8:1 in a mix bottle (IKA ST-20) for 20 minutes. Afterwards, the mixture was cast onto the glass stamp, bubbles were removed by vacuum treatment, and the stamps were cured in an oven at 130 °C for 20 minutes. In this experiment an anti-sticking layer, BGL-GZ-83 (PROFACTOR GmbH, Switzerland), was spin coated onto the clean surface of the glass master to facilitate the separation of master and mold. A printing process using PDMS mold is schematically shown in figure 4.4. In this work, the photoresist is AMONIL. AMOPRIME is spin coated onto glass using parameters shown in table 4.2 It is spun on onto pre-coated surface glass with AMOPRIME. As demonstrated by Hansen et.al [88], AMONIL resist is suitable for capillary force based lithography. Therefore, placing a PDMS mold onto AMONIL resist without any further external pressure is applicable. Using previous work parameters [88], a heating process at 75 °C for 5 minutes continued with UV exposure using MA-6 for 100 second. Table 4.3 shows the results of this experiment. When exposed to light perpendicular to the grating direction, it gives a poor grating effect. This means the quality of replicated structure in the AMONIL resist is poor. On the other hand, extending the UV-exposure time (900 second) using MA-6 without heating process shows better grating effect. Table 4.4 shows the result of this experiment.

Sample	Stamp	Fabrication date	UV exposure	Result
P79	b	28.01.11	100 sec	structured (low grating effects)
P89	a	31.01.11	100 sec	structured (low grating effects)
P74	b	31.01.11	100 sec	structured (low grating effects)
P81	c	31.01.11	100 sec	structured (low grating effects)

Table 4.3: a, b, and c have 300 nm, 350, and 460 nm in periodicities respectively. A heat treatment is performed at 75 °C for 5 minutes during printing process. Subsequently exposed by UV source (MA-6).

Sample	Stamp	Fabrication date	Treatment	UV exposure	result
P15	b	2.11.11	without heating	900 sec	structured (better grating effects)

Table 4.4: A "b" stamp that defines 350 nm in periodicity was used. Extended UV exposure time without involving heat treatment. UV source: MA-6.

This result shows that a longer exposure time is necessary to obtain better replication structure in the AMONIL resist. The results of this experiment allow Bragg grating replication of the master stamp on the glass to be realized. The Bragg grating morphology structure on the master stamp, PDMS mold, and AMONIL resist is characterized by Atomic Force Microscopy (AFM) as presented in figure 4.5. Since AMONIL resist takes 15 minutes to cure, another UV source (Beltron GmbH, Rödemark, Germany) was chosen. The distance between UV source and sample was kept fixed at 10 cm. The use of PDMS molds as a working stamp and AMONIL as a resist followed by enough UV exposure dose has become a standard process in this PhD work.

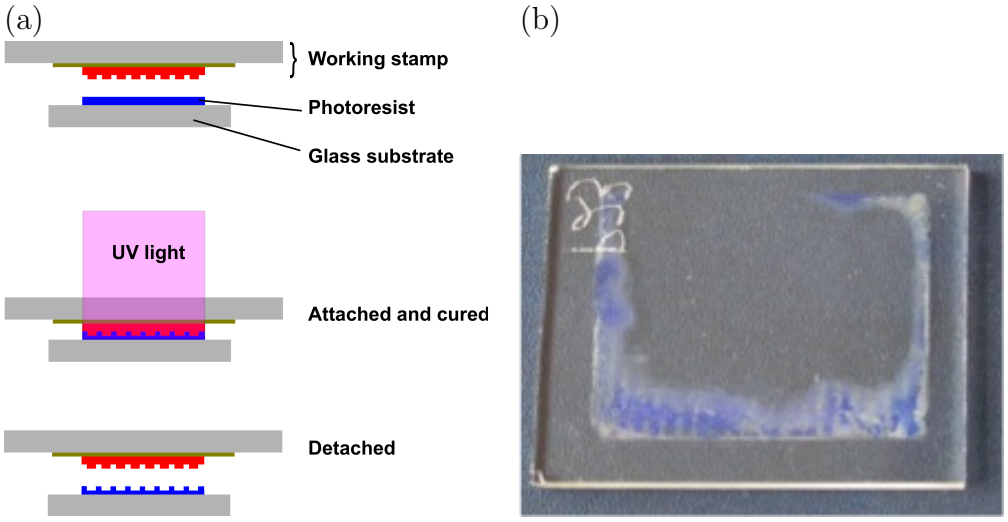

Figure 4.3: (a). Imprinting step employing working stamp glass. (b) Bragg grating transferred on the glass substrate. Inhomogeneous printed area, resulted of bumpy surface.

4.2 Dry Etching

Even though a Bragg grating was successfully replicated onto the Amonil layer, its properties to extract light in OLED devices were inadequate. In order to extract light in OLED systems, a high refractive index material between glass and anode should be added [6]. Commercially, AMONIL's refractive index is around 1.5, very similar to glass [93]. Two proposals to solve this problems are either to transfer the structure into a high index material beneath the AMONIL layer or to increase Amonil refractive index by introducing high refractive index nanoparticles, such as TiO_2, into the Amonil matrix. Pattern transfer in this work employs dry etching technique and will be presented in the following subsection 4.2.1.

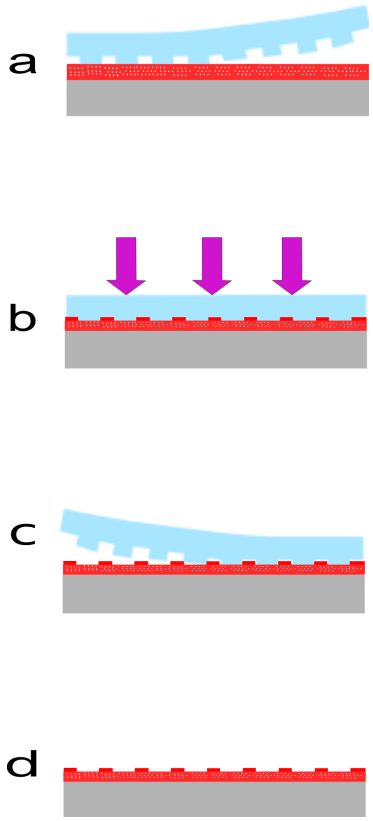

Figure 4.4: PDMS mold: amonil being attached by mold (a), UV exposure (b), Demolding (c), Pattern replicated onto photoresist (d).

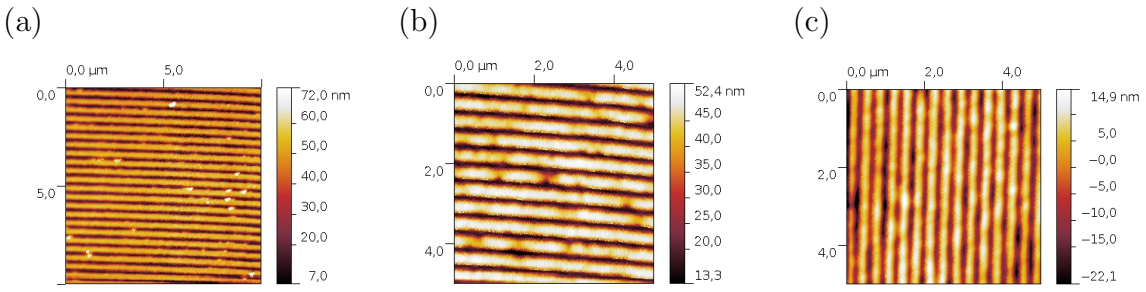

Figure 4.5: Master stamp (a), Bragg gratings replication on PDMS (b), and bragg gratings replicated on glass (c).

4.2.1 Experiment

A PDMS mold is fabricated using the same parameters as described in the previous section 4.1. Glass substrates with a Ta_2O_5 layer of 150 nm in thickness were cleaned using acetone and isopropanol for 15 minutes each. Subsequently, they were dehydrated on a hot plate at 160 °C for 10 minutes. Afterwards, an adhesion promoter (AMOPRIME) is necessary to avoid tearing during the separation process. The parameter is following 4.2. Subsequently, 200 nm AMONIL was spincoated on the substrate. The patterned PDMS mold is transferred into the photoresist without additional pressure and afterwards the photoresist is exposed to the UV light source (Beltron GmbH, Rödemark, Germany). Figure 4.6a-b shows the printing and curing process. In figure 4.6c-d, the PDMS mold is removed and the remaining structure replicated on the photoresist.

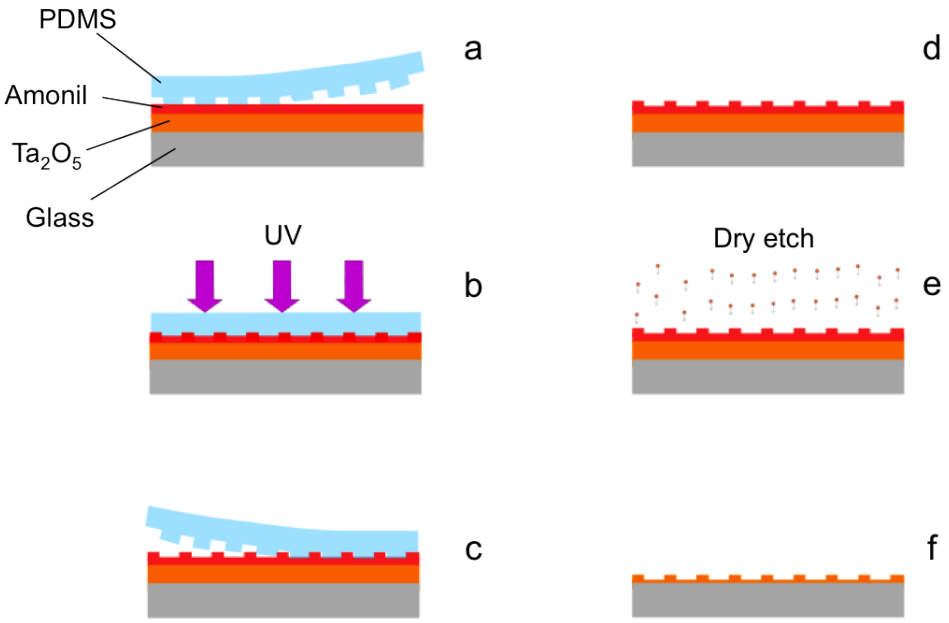

Figure 4.6: (a-d) Imprinting process steps. A Polydimethylsiloxane (PDMS) working stamp which contains a gratings structure, is replicated into photoresist. (e-f) Dry etching was performed in order to transfer the structure into a Ta_2O_5 layer. The process was carried out using the reactive ion etching technique.

In figure 4.6e, the structure in the photoresist is transferred into the Ta_2O_5 layer by Reactive Ion Etching (RIE). Since the photoresist is not designed for dry etching techniques, the selection of the reactive gas becomes crucial. In this experiment, a gas mixture of CHF_3/Ar that is also recommended by AMO GmbH [93], but with different ICP power of 100 Watt was used. These parameters are adjusted in ICP-RIE SI-500 manufactured from SENTECH Instruments GmbH, Germany. ICP-RIE standard parameters are given in table 4.5.

Further treatment was done using piranha solution to clean the surface of remaining organic residues, which could be left from the whole process. The obtained nanostructures were characterized using Atomic Force Microscopy (AFM) in the contact mode.

Gas	Concentration (sccm)	Pressure (Pa)	ICP (W)	RF (W)
CHF_3/Ar	25/75	3.99	100	150

Table 4.5: ICP-RIE parameter

4.2.2 Results and Discussions

Table 4.6 shows a number of experiment parameters in order to transfer the structure in the photoresist into Ta_2O_5 film. To avoid a number of unknown parameters, the experiment was limited to etching duration only, whereas pressure chamber (3.99 Pa), RF power (150 W) and gas composition concentration (CHF_3/Ar with ratio of 25/75 in sccm) remained constant. The effect of Inductively Coupled Plasma (ICP) in RIE systems was also introduced in this experiment and shows good replication into Ta_2O_5 film. Lift off process using piranha solution is performed to clean remaining AMONIL residue. The results are presented in table 4.7. Surface morphology was recorded using AFM and is presented in figure 4.7. The best depth profile that can be obtained using these parameters is 25 nm on average. Deeper penetration is difficult since Ta_2O_5 etch rate is lower compared to the AMONIL resist.

Sample	Time (minutes)	treatment	Result
10	20		Structured on the glass
11	10		no structure
12		25 sccm CHF_3 for 5 min, subsequently with 50/50 sccm Ar/CHF_3	no structure
T12	30		Structured
T7	35		Ta_2O_5 layer was completely
T14	25		etched but in the middle
T6	10		area still remain
T10	8		Structure still remain
T11	5		Structure still remain
T9	10		Structure still remain
T8	6		Structure still remain

Table 4.6: ICP-RIE work parameters

Sample	result
T8	only some part but structured areas were broken
T9	structured on Ta_2O_5, edge part better.
T10	not completely structured. Only in some part.
T11	Completely lifted, no structure

Table 4.7: AMONIL lift off using Piranha solution

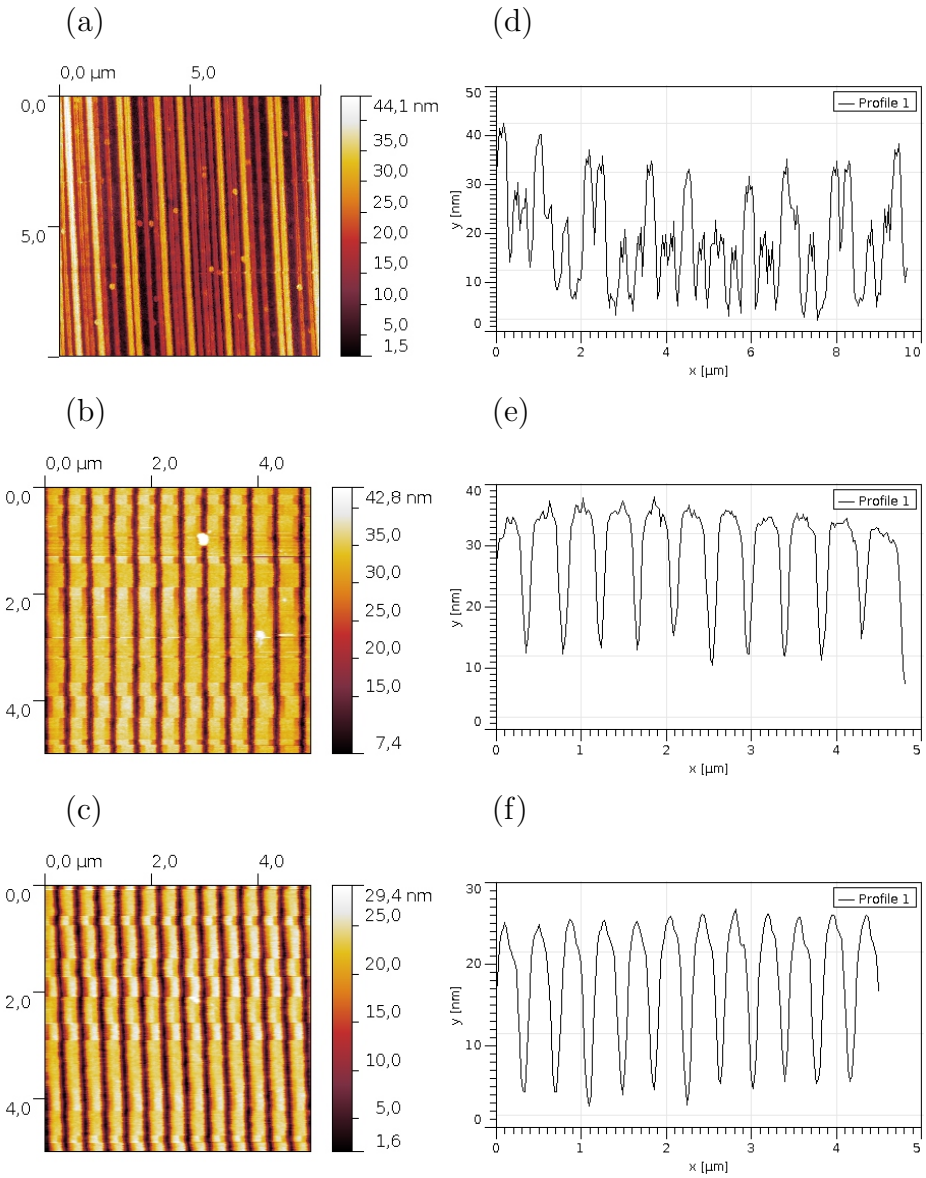

Figure 4.7: Images of multiperiodic grating structures replicated into Ta_2O_5 film recorded by AFM. (a) Superimposed Bragg grating with 500/400/300 nm periodicities. (b) A serial Bragg grating with 500/450/400 nm and (c) 450/400/350 nm in periodicities. (d-f). A depth profile of the multiperiodic grating structures after etching of 25 nm in depth on average.

4.3 Conclusion in this chapter

Elastomeric polymer or PDMS in combination with AMONIL resist are the best choice for use as a working stamp in UV-NIL technique. Next, with the right UV exposure dose Bragg fabrication using UV-NIL becomes more effective and reproducible. To enhance its potential, one proposal is to transfer the pattern from the resist into a Ta_2O_5 film which has high refractive index (n=2.1). Pattern transfer using the dry etching technique is promising to obtain an optimum result. The technique is not straightforward but some parameters must be adjusted in order to gain a good profile. Since there are many process parameters, the degree of freedom in terms of optimization is still broad and further investigation should be carried out.

Chapter 5

Hybrid NP-photoresist for UV-NIL

Summary

This chapter demonstrates that the introduction of TiO_2 nanoparticles into AMONIL resist will increase AMONIL phototresist. In the experiment, 1%, 2%, 3%, 5%, 10%, 20% and 30% TiO_2 nanoparticles (NP) in volume, are blended into AMONIL resist. This mixture is called a hybrid NP-photoresist. This hybrid material has higher index of refraction than that available by the original manufacturer. Furthermore, the ability in UV-NIL techniques does not experience significant changes. First, all films are deposited onto wafer with 1 μm thick oxide on top by spin coating technique. Then it is characterized by a profilometer and compared with reflectometer to determine the occurrence of a change of optical properties. The surface morphology is characterized by AFM. Afterwards, an optical property of the film is characterized with a UV-Vis spectrophotometer. For this method, samples are spin coated onto transparent glass. Finally, the Swanepoel method is performed to reveal the refractive index of the film.

5.1 Introduction

Transparent high refractive index material plays an important role in improving the performance of many solid state devices, including optoelectronic devices, integrated optical circuits, optical sensors and light emitting diodes [94]. Specifically to increase OLED's external efficiencies, a Bragg grating with high refractive index was sandwiched between glass and OLED in order to scatter the light which is trapped as a waveguide mode [5]. These techniques have been demonstrated in [5, 6]. Although both techniques are very good, the process requires a complex manufacturing scheme and is relatively expensive. For example, the production cost of Ta_2O_5 and Indium Tin Oxide (ITO) is expensive in terms of material and deposition technique. In order to reduce the complexity of manufacturing scheme and production cost, a high refractive index photoresist and deposition using spin coating technique is the first priority. UV-NIL technology is one of the promising candidates for fabricating Bragg gratings and fulfill the criteria demonstrated previously in chapter 4. Nanoimprint technology is described very well in ref [95]. After studying [96] carefully, the elastomeric mould of polydimethylsiloxane (PDMS) polymer was chosen. The main problem with this technology is on the photoresist, which has a refractive index similar to that of the glass substrate (n$\simeq$ 1.5). Therefore, in order to

increase its refractive index, TiO_2 nanoparticles, which have a refractive index around 2.4 - 2.6 depending on the crystal structure [94], are introduced. Modifying the polymer's refractive index by adding high refractive index nanoparticle materials such as zirconia and titania has been proposed and successfully increased its refractive index in some literature [97, 98, 99, 100, 101], but its use for UV-nanoimprint technology has still not been reported. This work demonstrates an easy way to increase photoresist refractive index by introducing high refractive index TiO_2 nanoparticles (NP) without losing its ability to form in UV-nanoimprint process. The hybrid NP-photoresist properties are characterized. Optical and surface characteristics are demonstrated.

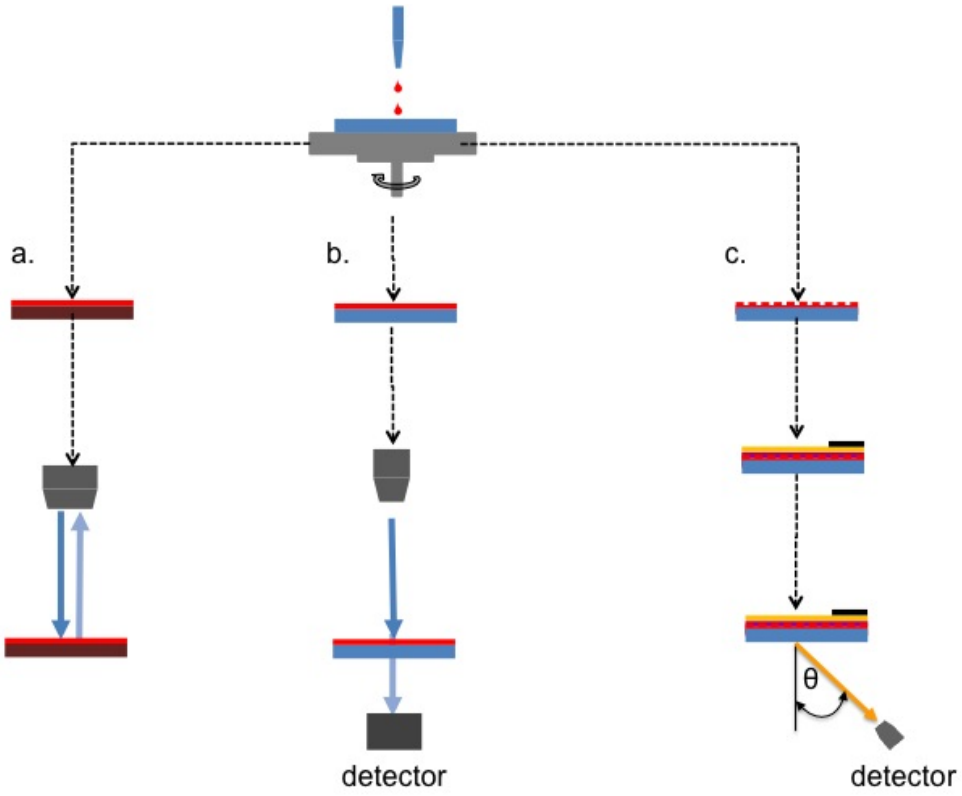

Figure 5.1: Modified polymer photoresist contained a variation of TiO_2 NP concentration deposited on the substrate using the spin-coat technique. (a) SiO_2/Si wafer was deposited with the modified polymer. A reflectometer measurement was performed on this substrate to determine its refractive index. (b) Modified polymer resist was deposited on the glass substrate. Transmission characterization was recorded using a UV-vis spectrometer. (c) UV Nanoimprint lithography was performed using modified polymer. Afterwards, OLED was fabricated on the Bragg grating layer. Angle resolve measurement from OLED emission character was performed on a plane perpendicular to the grating grooves.

5.2 Experiment

Bragg gratings were fabricated on the glass using Laser Interference Lithography (LIL) which is then used as a master stamp [5]. A flexible elastomeric mold, PDMS, is fabricated using the standard parameter as described earlier in chapter 4. In this work, a PDMS mold

is replicated from a master stamp with 1-D photonic structure. The periodicity is 460 nm. Glass substrates in this work are cleaned using a standard procedure already mentioned in chapter 3, subsection 3.1.4. An adhesion promoter, AMOPRIME, is spin coated onto all glass substrates. TiO_2 nanoparticles (NP) are blended into Amonil photoresist by adding TiO_2 NP dispersed in xylene, purchased from Sigma Aldrich, to the Amonil resist directly. In order to understand TiO_2 NP effects in the Amonil resist, blendings of 1%, 2%, 3%, 5%, 10%, 20% and 30% TiO_2 NP in volume are prepared and determined. The hybrid NP-photoresist and pristine AMONIL are spin coated onto the pre-coated glass substrate. Afterwards, a PDMS mold is placed onto pristine and hybrid resist with its own weight. All resists are exposed to a UV light source (Beltron GmbH, Rödemark, Germany) by ensuring a dose of 2 J/cm^2. The spin coating parameters of AMOPRIME, AMONIL, and hybrid NP-photoresist are the same as written in table 4.2 in chapter 4. Investigation of hybrid NP-photoresist refractive index is carried out using a reflectometer (Sentech Instruments GmbH) and UV-Vis spectrometer (Perkin Elmer, lambda 900) to characterize its transmission properties. The reflectometer characterizes hybrid NP-photoresist film thickness and refractive index on silicon wafers with 1 μm oxide on top as shown in figure 5.1a. In figure 5.1b, UV-Vis spectrometer is used to characterize hybrid NP-photoresist film on the glass substrate. Photoresist thickness was physically measured by profilometer (Ambios Technology XP2).

5.3 Thickness and grating characterization

Our commercial photoresist (Amonil) was designed only for nanoimprint purpose; which has a refractive index of approximately 1.5 [93]. In order to extract the light, a layer beneath the OLED serves as light extractor, the refractive index contrast should be significantly different [102]. TiO_2 nanoparticles are selected because of their high refractive index property. After the TiO_2 NP addition, a change in viscosity occurred. An AFM image in figure 5.2 proved that its potential to form and be cured still remained. The image shows that the Bragg gratings on Amonil and hybrid NP-photoresist 30% are similar. Viscosity change caused thicker film such as TiO_2 NP concentration to increase, at the same angular velocity. Its properties deteriorate as more than 30% mixture is applied. Refractive indeces and thicknesses changed as a function of TiO_2 NP, as presented in table 5.1.

%vol TiO_2 in Amonil	Thickness (profilometer)(nm)	Thickness (reflectometer)(nm)	Refractive index, n at 632.8 nm	calculated average refractive index at 900 nm
1	205	210	1.514	1.51
2	215	210	1.59	1.52
3	219	219	1.59	1.53
5	239	244.52	1.59	1.55
10	287,33	272.86	1.597	1.6
20	391	390.31	1.65	1.7
30	555.8	579.37	1.71	1.8

Table 5.1: Compositions, thickness measurement using profilometer, reflectometer, measured refractive index, and refractive index in concentration averages. Silicon wafer was used as a substrate in this experiment.

(a)

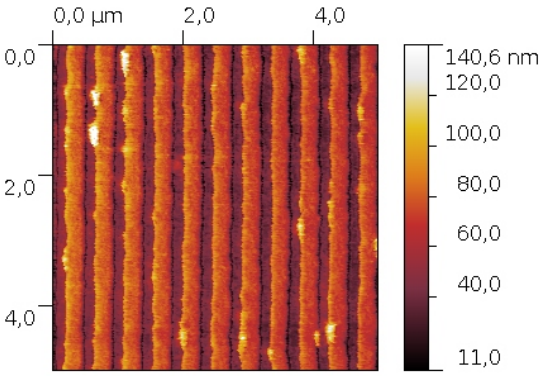

(b)

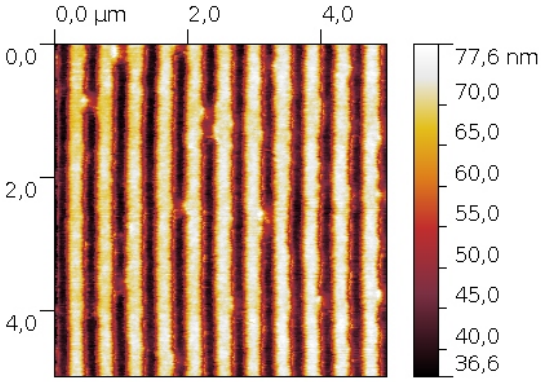

(c)

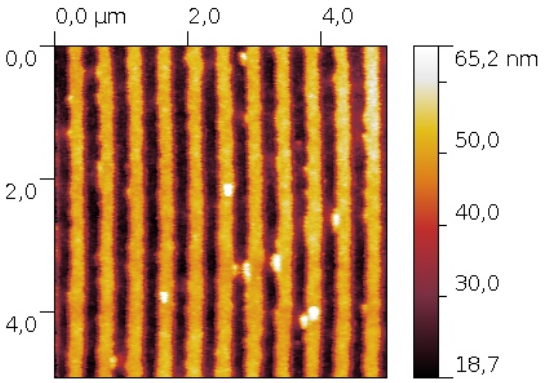

Figure 5.2: AFM image of Bragg gratings from a) Master stamp on glass (460 nm in periodicity), b) pristine Amonil, c) hybrid NP-photoresist 30%.

Since the profilometer has 5% to 10% deviation in nm range, the thickness of the sample films measured using a reflectometer was still within the tolerance range. Table 5.1 shows that the refractive index changed as a function of TiO_2 NP concentration in the Amonil resist. Originally, a reflectometer is designed to characterize a thin film thickness by its optical properties. In this method, thin film refractive index is an input. If the reflectivity obtained in experiment fits the simulation, then the film thickness is supposedly accurate. This experiment is to investigate whether there are any changes in the refractive index after TiO_2 NP addition and to confirm the thin films thickness obtained by profilometer technique. In table 5.1, average refractive index is obtained from the sum of known refractive index times the concentration for each component. The refractive indexes of TiO_2 and Amonil are 2.5 and 1.5 respectively.

5.4 Refractive index characterization

The optical transmission characteristics at UV-Vis range of our film were also recorded. It was shown that TiO_2 NP addition changes its transmission properties. As can be seen in figure 5.3, the increase in TiO_2 NP concentration also increased absorption levels at UV range. Refering to [103] and [104], TiO_2 has a band gap of around 3.2-3.8 eV, depending on the crystal structure. Regarding the TiO_2 band gap, the strong absorption was located at around 326.31 - 387.5 nm in wavelength. In the hybrid NP-photoresist 10% to 30% cases, the film experienced interference fringe effects on the transmission curves. Stronger effects occurred in hybrid NP-photoresist 20% and 30%. Interference fringes in our film indicated the changes in the optical properties. In order to analyze the

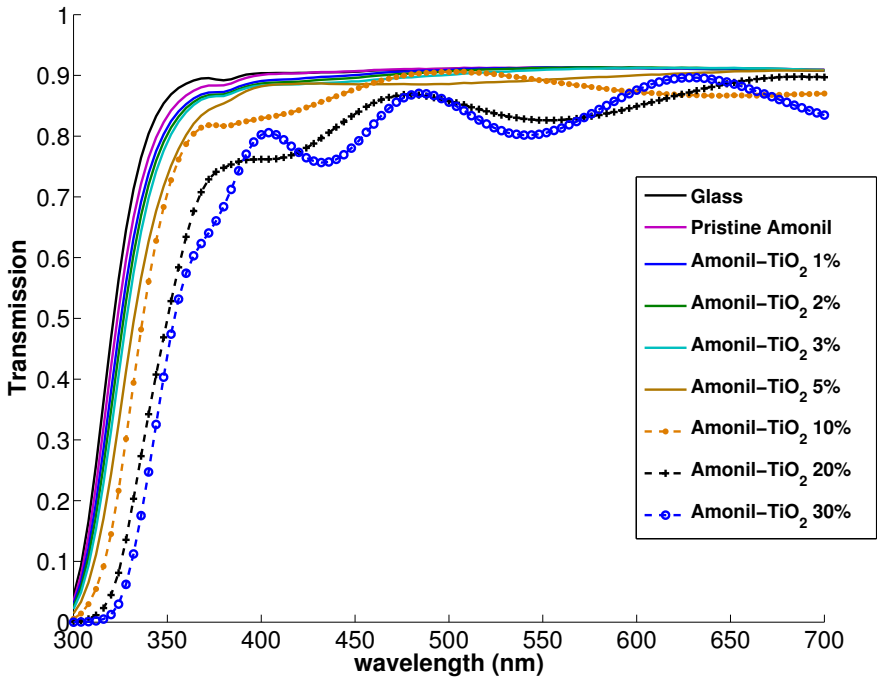

Figure 5.3: Transmittance spectra of glass, pristine Amonil resist and hybrid NP-photoresist composite

optical transmission of fabricated films, a simulation proposed by Swanepoel [105] was performed. The refractive index, $n(\lambda)$, of the film can be determined using the following equation:

$$n(\lambda) = [N + (N^2 - s^2)^{\frac{1}{2}}]^{\frac{1}{2}} \tag{5.1}$$

where

$$N = 2s\frac{T_M - T_m}{T_M T_m} + \frac{s^2 + 1}{2} \tag{5.2}$$

The value of s is determined by using equation 5.3 with T_s being glass transmittance:

$$s = \frac{1}{T_s} + (\frac{1}{T_s^2} - 1)^{\frac{1}{2}} \tag{5.3}$$

A parabolic interpolation between three nearest points should be done to obtain T_M and T_m from the interference curve. In this work, the interference fringe shows only 2 points maxima and 2 points minima. Thus, a parallel parabolic fit is used. As presented in figure 5.4 the parabolic fit applies to TiO_2 20% and TiO_2 30%.

As T_M and T_m fitted, then the refractive index of each film was determined using equation 5.1. The results are plotted in figure 5.4c. The curve is abnormal since it hikes at 650 nm to 700 nm in the wavelength. A normal refractive index curve should give either a straight line or a downturn. Since the parabolic interpolation should involve three nearest points instead of two, the validity of the equation 5.2 becomes inapplicable. As a result, an abnormal curve appears.
Another approach was chosen, constructive peaks were used and put into the following equation to determine film thickness, refractive index, and m [105]:

$$l/2 = 2d(n/\lambda) - m_1 \qquad l\text{=}0,\ 1,\ 2,\ 3,\ ... \tag{5.4}$$

Equation 5.4 is in the form of a straight line. A plot of $l/2$ versus n/λ, a straight line will appear with slope 2d and a cut off on y axis of $-m_1$ [105]. The average refractive index value is used from the table 5.1. The value of m_1 shows 2 and 3 for TiO_2 20% and 30% in the transparent region. As m_1 is known, the value into the interference fringes basic equation is plotted to obtain the refractive index, $n(\lambda)$ [105]:

$$m\lambda = 2nd \tag{5.5}$$

One of the observed results from equation 5.5 are presented in table 5.2 and 5.3:

λ	m	Thickness (d) (nm)	Refractive index (n)
630	3	508	1.86
540	3.5	508	1.86
484	4	508	1.91
432	4.5	508	1.91

Table 5.2: Refractive index of TiO_2 30% obtained from equation 5.5.

A least-square fit using the following equation was performed for $n(\lambda)$ and generated as shown in figure 5.6:

(a)

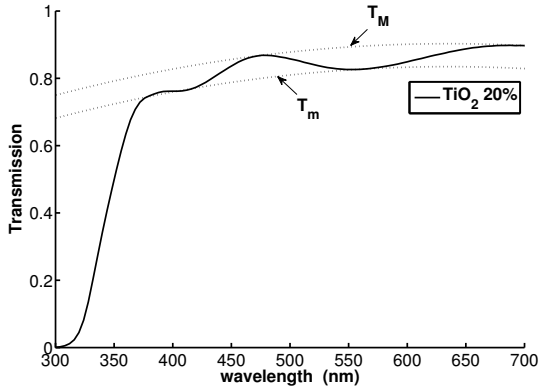

(b)

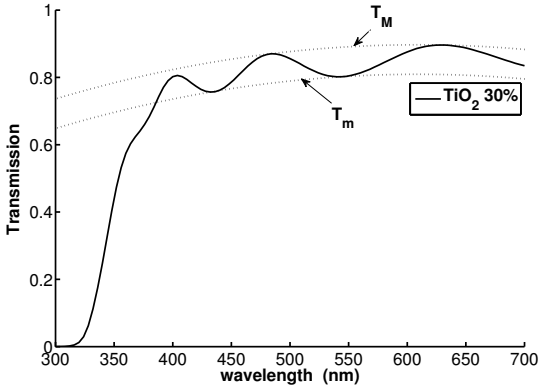

(c)

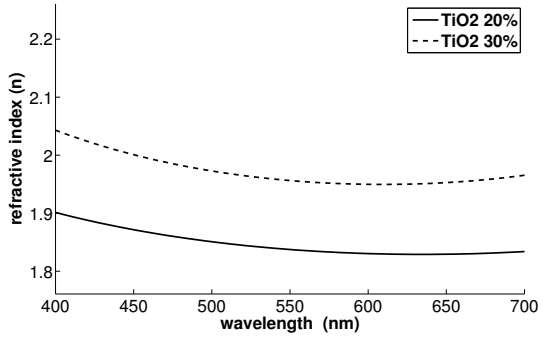

Figure 5.4: Two nearest points parabolic interpolation curves of transmission interference fringes of (a). hybrid NP-photoresist 20% , (b). hybrid NP-photoresist 30%, and (c). thin film refractive index

λ	m	Thickness (d) (nm)	Refractive index (n)
684	2	383	1.79
556	2.5	383	1.81
476	3	383	1.86
404	3.5	383	1.85

Table 5.3: Refractive index of TiO_2 20% obtained from equation 5.5.

$$n(\lambda) = a + b/\lambda + c/\lambda^2 \tag{5.6}$$

For hybrid NP-photoresist 20% the values of a, b and c is 1.696, 68.95 nm, and -796 nm^2 respectively. And the constant values of a, b, and c for hybrid NP-photoresist 30% is 1.76, 44.45 nm, and 8710 nm^2, respectively. Obtained n(λ) was then used in algorithm [105] to simulate the interference fringe and compare it with the experiment as presented in figure 5.5.

(a)

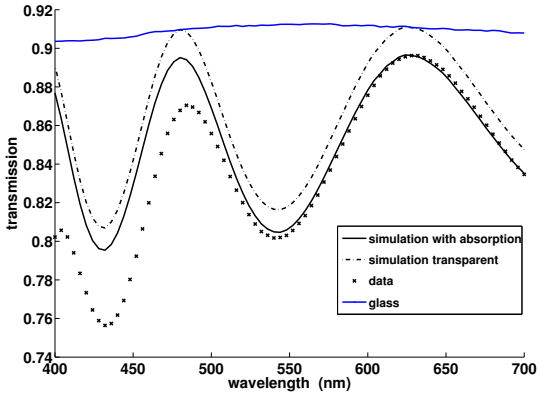

(b)

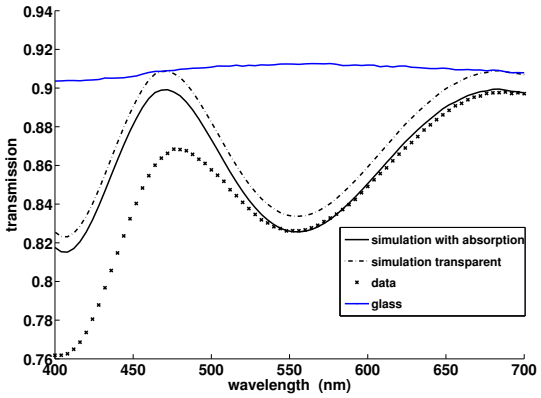

Figure 5.5: (a) The experimental and simulation transmission of hybrid NP-photoresist 30%. and (b) hybrid NP-photoresist 20% film with a transmission of glass as a reference. Simulations are performed in transparent and absorption conditions.

Two conditions in the simulation were performed in order to identify A-TiO_2 optical characteristic. A transparent condition and absorption coefficient were included in the simulation. Figure 5.5 shows that simulation in transparent condition gave similar amplitude to the experiment, especially in the transparent region (550-700 nm). The transparent simulation maximum peak touch with glass transmission, as indicated in this simulation's validity. In order to fit experimental data using this simulation, an absorption coefficient ($\alpha(\lambda)$) condition should be included in the equation. I assume ($\alpha(\lambda)$) to be constant. As a result, simulation interference shifted down and fit exactly with our

experiments data in the transparent region. On the other hand, the unfitted interference area, 500-400 nm, shows that the absorption is higher than transparent region. From this simulation, $n(\lambda)$ and $k(\lambda)$ can be derived from the equation in [105] and plotted in figure 5.6a and 5.6b.

(a)

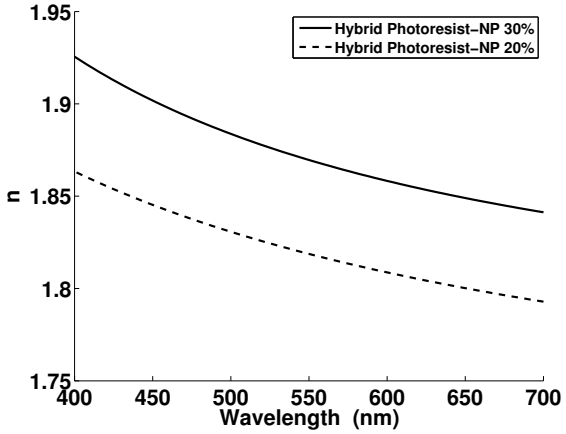

(b)

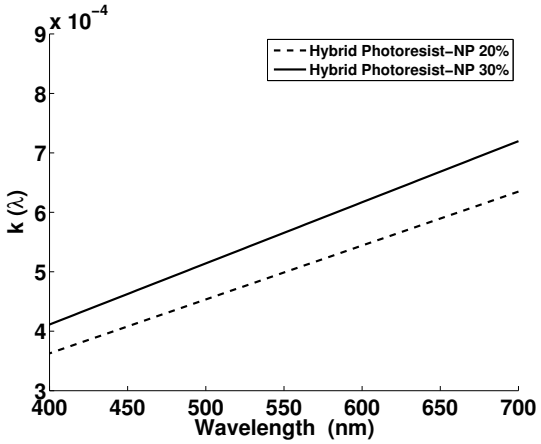

Figure 5.6: (a) The refractive index of the thin films. For hybrid NP-photoresist 30%, a=1.76, b=44.45 nm and c=8710 nm^2. For hybrid NP-photoresist 20%, a=1.696, b=68.95 nm and c=-796 nm^2. and b) extinction coefficient.

5.5 Conclusion in this chapter

Nanoimprint technique allows fabrication of Bragg gratings in a large area and at relatively low production cost. The addition of TiO_2 NP increases the refractive index of AMONIL photoresist without sacrificing its imprint ability. Pristine AMONIL photoresist and hybrid NP-photoresist are characterized by profilometer and reflectometer. The thickness values are in the deviation range. The refractive index obtained for the wavelength range of interest from 520-650 nm (Superyellow emission) is 1.878-1.84 for 30% and 1.826-1.801 for 20% NP contain. Hybrid NP-photoresist values at 550 nm are 1.869 and 1.818 for 30% and 20% NP contain respectively.

Chapter 6

Nanostructured hybrid NP-photoresist in OLEDs

Summary

Previous work in chapter 5 demonstrated that TiO_2 NP may tailor the refractive index of AMONIL resist. A blend of AMONIL resist and TiO_2 NP is called hybrid photoresist-NP. This chapter focuses on its application to improve OLED external efficiency. TiO_2 NP concentrations variation in AMONIL resist are the same as used in chapter 5. Subsequently, the resists are structured by UV-NIL technique. ITO-free OLEDs are then fabricated onto structured hybrid photoresist-NP. The emission characteristics were recorded by a goniometer. Emission is generated by means of photoluminescence (PL) and electroluminescence (EL) technique. Electrical (I-V) characteristics of the OLEDs for each different resist were also recorded. Effective refractive indices obtained from the experiment are compared to the theory that is simulated in a transfer matrix simulation (TMM).

6.1 Experiment

Bragg grating (BG) is fabricated onto an identical glass substrate using the same preparation techniques as demonstrated in chapter 5. Here, the BG has 370 nm in periodicity and is fabricated with blending 1%, 2%, 3%, 5%, 10%, 20% and 30% TiO_2 NP in volume into AMONIL resist. Grating fabrication was done by UV-NIL technique and is schematically shown previously in chapter 5 and in figure 5.1. Subsequently, oxygen plasma (SI-100, Sentech GmbH, Germany) is applied onto resists to modify BG's surface wettability for 1 minute. In this process, 8 sccm oxygen is used. The RF power is 100 Watt. Afterwards, 70 nm of anode polymer (PH500 purchased from H. C. Starck, Germany) was deposited onto the BG resist by spin-coat techniques. Then the 80 nm light emitting layer, PDY-132 (SuperYellow) purchased from Merck OLED Materials GmbH, was spin-coated on the anode polymer. As a cathode, 1 nm LiF and 200 nm Al was deposited using the thermal evaporation technique. The OLED's active area is 5 mm x 5 mm. All fabricated OLEDs are encapsulated using epoxy resin adhesive and glass cover in order to allow electrical measurements and electroluminescence (EL) characterization of the devices in ambient conditions. Electrical measurements of I-V curves and electrolu-

minescence of the devices were made using a source-measure unit (SMU, Keithley). Angle resolved EL measurements are carried out using the same SMU and spectrophotometer. Each sample was attached in the goniometer and rotated on the vertical axis, while a multimode optic fiber with lens system was kept fixed perpendicular to the active area. A TE polarizer was attached between the sample and multimode optic fibers.

6.2 Results and discussion

6.2.1 Photoluminescence measurement

In figure 6.2 we can see the emission characteristics of the OLED devices with integrated 1-D photonic grating (Bragg grating) slab waveguide. The emission is recorded by goniometer. The gratings are made from pristine AMONIL and hybrid photoresist-NP with 1%, 2%, 3%, 5%, 10%, 20% and 30% TiO_2 NP in volume concentration. Here, the photoluminescence (PL) emission is characterized. PL technique employed UV laser with 405 nm in wavelength. Figure 6.2h shows a sharp peak on the spectrum. This indicates that the device experienced some leaking. Bragg grating in this layer successfully coupled out the emitted light in the waveguide mode in the hybrid photoresist-NP 30%. Compared to the BG made from pristine AMONIL and with a lower refractive index hybrid photoresist-NP, the sharp peak or leaking mode in the spectrum did not appear. As expected, there is no waveguide mode in pristine AMONIL and low TiO_2 NP concentration in hybrid photoresist-NP. Since the refractive index in pristine AMONIL and hybrid photoresist-NP is similar to the surrounding materials, glass substrate and anode layer, facilitating the radiation energy in this layer is not enough. On the other hand, hybrid photoresist-NP 30% has a high refractive index contrast to the surrounding materials, where most of the radiation energy is concentrated in this layer [106]. The concentrated radiation energy propagating in the high refractive index layer is simulated by the transfer matrix method. The result is presented in figure 6.1.

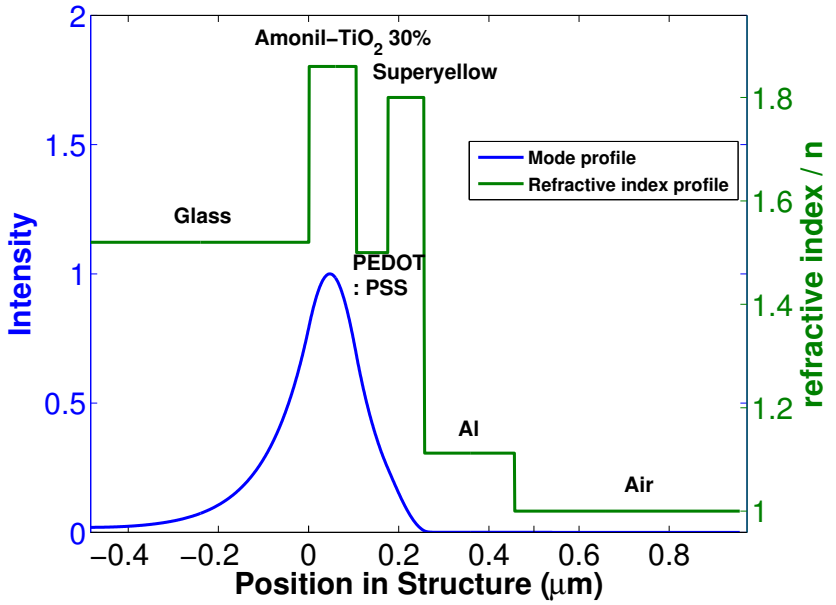

Figure 6.1: Transfer Matrix Simulation (TMM) intensity profile of TE_0 mode in the layer structure of the device.

6.2.2 Electroluminescence measurement

Besides the PL technique, the electroluminescence (EL) technique was also used. In this method, BG made from pristine AMONIL, hybrid photoresist-NP 3% and 30% con-

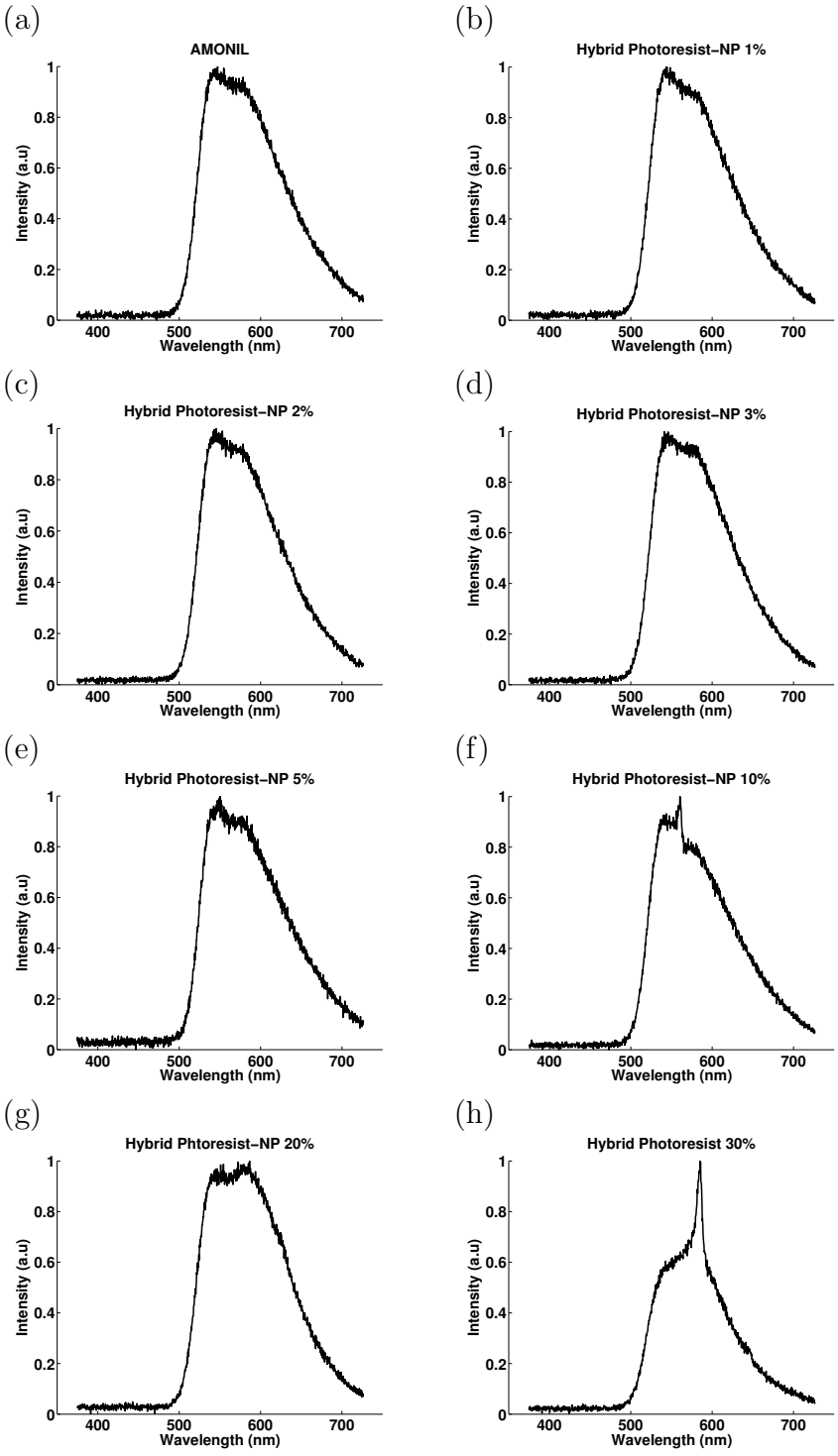

Figure 6.2: PL emission spectra of devices containing nanostructured hybrid photoresist with 0%, 1%, 2%, 3%, 5%, 10%, 20% and 30% NP content at $\theta = 0°$. The devices containing low concentration hybrid photoresist-NP showed no change in the spectrum (a-g). On the other hand, the device with 30% hybrid photoresist-NP can couple out the waveguide mode into air

taining TiO_2 NP in volume were fabricated and sandwiched between the glass and the OLEDs. For the purpose of comparison, an unstructured (reference) and structured film (nanostructured) were also fabricated and characterized. Figure 6.3 shows the electrical property of the reference and nanostructured devices. The electrical characteristics of every sample showed different results. It is interesting that the threshold voltages for every material shifted. Low threshold voltage was obtained by the device with hybrid photoresist-NP 3%, while AMONIL reference and hybrid photoresist-NP 30% are identical. The lowest threshold voltage was found for the nanostructured AMONIL device. On the contrary, the highest threshold voltage was obtained by hybrid photoresist-NP 30%. It seemed that internal efficiency of the devices was affected. It is likely that this was caused by the charge balance in the device.

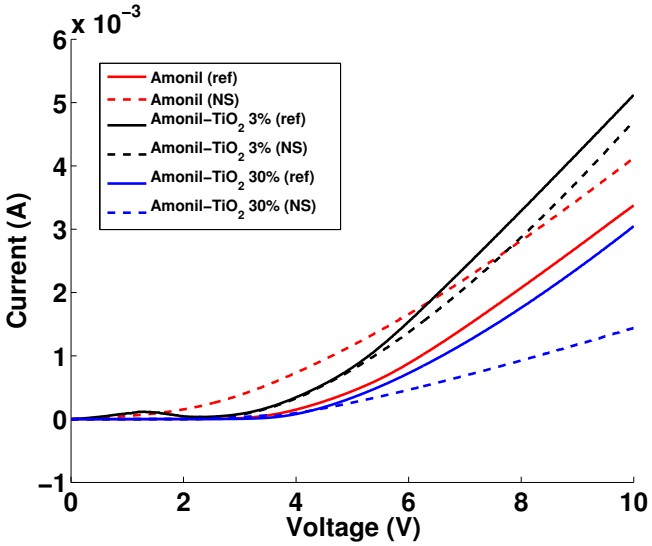

Figure 6.3: Electrical characteristic of the device containing pristine AMONIL, hybrid photoresist-NP 3% and hybrid photoresist-NP 30%. A dashed line indicates nanostructure and a continuous line is used for reference (without structure). The threshold voltage differs from one sample to another, indicating changes in internal efficiency of the OLED.

Figure 6.4 shows that the device with high refractive index (hybrid photoresist-NP 30%) experienced outcoupled emission from the device as a function of the angle. The angle of the outcoupled emission is given by [63]:

$$k_0 \, sin\theta = \beta \pm (^{2\pi m}/_{\bigwedge}) \tag{6.1}$$

Where k_0 is the free-space wavevector of the scattered light, θ is the angle of emission with respect to normal, $\bigwedge$ is the grating period and m is the scattering order. Using equation 6.1 the effective refractive index (β/k_0) of the first order outcoupling (m =1, θ=0°, period=370 nm, λ = 591.8 nm) is 1.599. A sufficient contrast in refractive index is experimented and demonstrated. In order to compare the experimental result, a numerical simulation (transfer matrix method) can predict the power distribution of emitted light into waveguide mode in the device as a function of material properties such as thickness, refractive index, and extinction coefficient. Waveguide modes are described by their in-plane propagation vector, β, and the polarization of the electric field. Since PDY 132 (SuperYellow) is PPV derivative, the anisotropic nature is high, and therefore all the

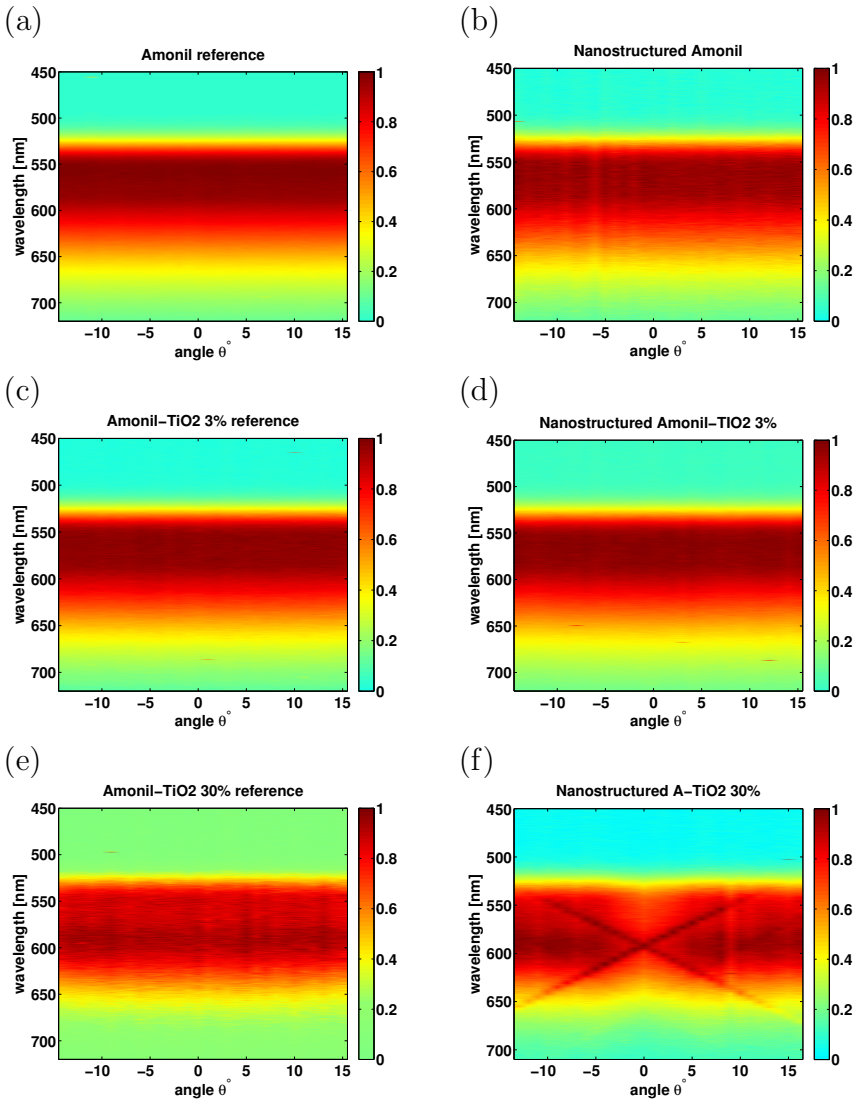

Figure 6.4: EL emission spectrum for pristine AMONIL, hybrid photoresist-NP 3% and 30% in the device. The EL spectrum of AMONIL (a), hybrid photoresist-NP 3% (c) and 30% (e) did not indicate the presence of outcoupling mode. The emission spectrum in nanostructured AMONIL (b) and hybrid photoresist-NP 3% (d) remained unchanged. The outcoupling mode occurred in hybrid photoresist-NP 30% (f).

waveguide light has its electric field in the plane of OLED (transverse electric (TE)-polarized) [63]. Figure 6.1 shows that TMM simulation predicted the distribution of the in-plane electric field (TE) intensity as a function of the location in the device at 591.8 nm in the wavelength. The hybrid photoresist-NP film underwent a concentrated electric field in the device. In this layer, the introduction of Bragg grating has a significant effect. The effective refractive index in this simulation is 1.598 for TE_0 mode.

6.3 Conclusion in this chapter

This work shows that hybrid photoresist-NP 30%; sandwiched by low refractive index materials allows radiation energy to propagate in this layer. Placing Bragg grating in this layer results in coupling out the waveguide mode into leaking mode. The angular emission of PL and EL technique confirms the advantage of hybrid photoresist-NP 30% once embedded in OLEDs. The emission spectrum shows a sharp peak and depends on the angle.

This experiment results in figure 6.2 and figure 6.4 verified that the concentrated radiation energy will not propagate in the system as the refractive index of the slab waveguide is similar to the surroundings (glass substrate and PEDOT:PSS film).

Grating periodicity in this layer is 370 nm. Putting this number into the Bragg equation, the effective refractive index in this system is 1.59 at 591.8 nm in the wavelength. The experimental and theoretical results show good agreement. Electrical characteristics differ from one sample to another, which is probably caused by internal efficiency. The advantage of hybrid photoresist-NP is not only that it is straightforward and eliminates complexe fabrication schemes but that it can also be potentially applied on the flexible substrate as a slab waveguide. This will be demonstrated in chapter 7.

Chapter 7

Hybrid NP-photoresist for flexible OLEDs

Summary

Chapter 6 demonstrates the advantages of 1-D photonic crystal slab (Bragg grating) made of hybrid photoresist-NP 30% for waveguide mode extraction in planar OLEDs. One challenging task is to integrate Bragg grating into flexible OLEDs. Recent efficiency enhancement developments in flexible OLEDs are introduced in chapter 2 section 2.6. None of these integrate Bragg gratings into flexible OLEDs. In this chapter, Bragg gratings are integrated into flexible OLEDs using the knowledge already developed in the previous chapters in this work. Here, hybrid photoresist-NP 30% is implemented to facilitate light extraction in flexible OLEDs. The emission characteristic in flat and bend condition is recorded by a goniophotometer. The bend condition influences Bragg grating periodicity and the thickness of the films due to material deformation. The effects are studied in theory and experiment. Substrate deformation is calculated by beams bending theory. Putting the theoretical results into the transfer matrix simulation (TMM) then gives theoretical effective refractive index (n_{eff}) of the device for all bending conditions. As a result, the theoretical n_{eff}, shows a good agreement with the experiment. This is plotted in figure 7.5 and figure 7.6. This work is reproducible and the emission characteristics are recorded in appendix C and D.

7.1 Theory of 1-D photonic crystal slab deformation

The deformation in the hybrid photoresist-NP 30% is modeled using beam bending theory [107]. Depicted in figure 7.1a, the bending system is a carried out by two screws in combination with anchors on two sides of the substrate. The screw is adjustable from 0 mm to 2.2 mm. The force (F) can be measured through deflection equation 7.1. The deflection simply measures the distance of the screw that pushed the probes (Δz). The value of a and b is l/2, with l=25 mm. Young modulus is represented as E and inertia moment for this system is Iy. The moment of inertia in this system is calculated using equation 7.2. The total length of the probe is L. Once F is calculated, the stress in x-direction may be predicted using equation 7.3. Since our probe has 1 mm in the thickness, the value of z in equation 2 is 0.5 mm. As follows, strain in x-, y-, and z-direction may be

calculated using equation 7.4, 7.5, and 7.6. At z=0.5 mm σ_y is assumed to be 0, equation 7.6 becomes equation 7.7. Poisson ratio (ν) and Young modulus (E) for PC in this work is set to 0.37 and 2 GPa, respectively.

$$w(a) = \frac{Fa^2b^2}{3EI_yL} \tag{7.1}$$

$$w(a) = \frac{b.h^3}{12} \tag{7.2}$$

$$\sigma_x = \frac{w(a)}{I_y.z} \tag{7.3}$$

$$\varepsilon_x = \frac{\sigma_x}{E} \tag{7.4}$$

$$\varepsilon_y = -\nu\frac{\sigma_x}{E} \tag{7.5}$$

$$\varepsilon_z = -\frac{\nu}{E}(\sigma_x - \sigma_y) \tag{7.6}$$

$$\varepsilon_z = -\frac{\nu}{E}.\sigma_x \tag{7.7}$$

In this bending mechanism, the strain across the substrate is not uniform, depending rather on the position. In figure 7.1b, the bending mechanism is assumed to be fixed in y- and z-directions below the anchors while in x-direction it is free to move. At the screw position, the displacements in x-direction and y-direction are assumed to be zero (Δx=0 and Δy=0). The purple dot in the picture indicates the measurement position. In this position, the strain values in x-direction ε_x and z-direction ε_z for Δz = 2.01 mm are 1.46% and -0.5386%, respectively. The strain values in x- and z-direction as a function of Δz are tabulated in table 7.1. The deformation leads to the change in the Bragg grating periodicity and the thickness. Strain in x-direction increases Bragg grating periodicity ($\bigwedge$) and compression in z-direction shrinks the thickness (d_{WG}). In table 7.1, $\bigwedge$ an increase from 460 nm to 467.2 nm for every Δz and d_{WG} shrinks from 450 nm to 447.4 nm. Putting d_{WG} values into the TMM simulation, the effective refractive index (n_{eff}) values in TE_1 mode show very small change. This shows that the n_{eff} is nearly constant for every Δz. As n_{eff} is assumed to be constant, the change in the waveguide mode extraction angle θ under bending conditions may be calculated using equation 6.1. As given in table 7.1, the values of waveguide mode extraction angle (θ_{th}) increase as a function of Δz.

Table 7.2 shows the parameters that are used in TMM simulation. In this table, the refractive indices and the thicknesses of the OLED materials are given except the thickness of Amonil-TiO_2 30% selected as a free parameter. The given refractive index is dependent on the wavelength (λ).

In figure 7.2a, the simulation of TE and TM modes as a function of Amonil-TiO_2 30% or hybrid photoresist-NP thickness are plotted. From the graph, thicker hybrid photoresist-NP layer, i.e. 650 nm, is able to support three TE (TE_0, TE_1, TE_2) and three TM (TM_0, TM_1, TM_2) modes at 550 nm in the wavelength. On the contrary, a thinner layer, i.e. 100 nm, is only able to support one TE (TE_0) and one TM (TM_0) at 550 nm in wavelength. In figure 7.2b, the resonance wavelength mode as a function of hybrid photoresist-NP 30% thickness are plotted for $\bigwedge$ = 460 nm and $\theta_{th} = 25°$. Figure 7.2c is a

(a)

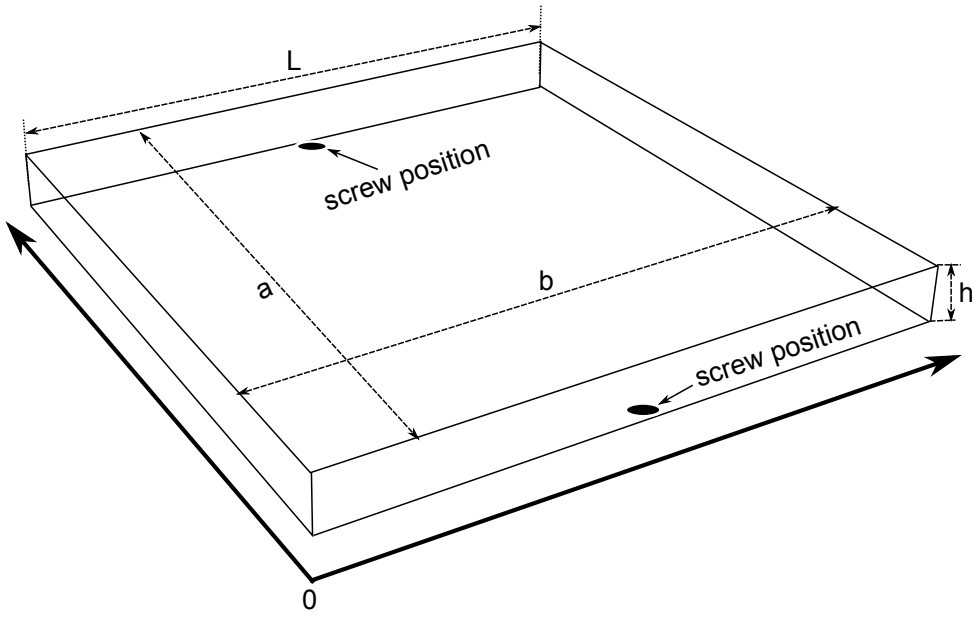

(b)

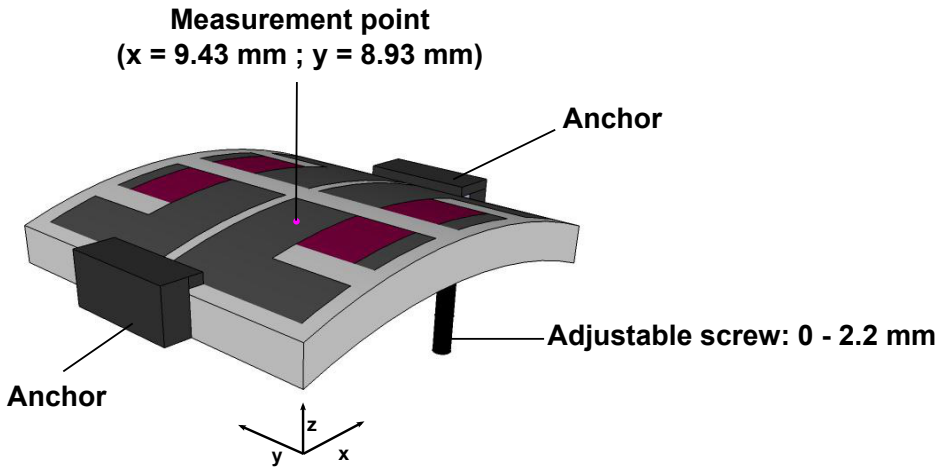

Figure 7.1: (a) A schematic diagram of PC substrate in flat condition. (b) PC in bend condition.

Δ z (mm)	ε_x%	ε_z%	$\bigwedge$ (nm)	d_{WG} (nm)	TE_1 (λ =550 nm)	θ_{th} (λ =550 nm)
0	0	0	460	450	1.672	28.45
0.93	0.67	-0.2492	463.082	448.88	1.672	28.96
1.23	0.89	-0.3296	464.094	448.52	1.671	29.13
1.505	1.09	-0.4033	465.014	448.18	1.671	29.29
2.01	1.46	-0.5386	466.716	447.57	1.671	29.57
2.165	1.57	-0.58	467.222	447.39	1.67	29.66

Table 7.1: Theoretical analysis of strain in x-direction and compression in z-direction as a function of screw displacement (Δz) in figure 7.1. The change of grating period ($\bigwedge$) and waveguide thickness (d_{WG}) is calculated from ε_x and ε_z, respectively. An effective refractive index, n_{eff} at λ = 550 nm, is calculated for TE_1 mode using TMM simulation. The expected theoretical resonance emission angle (θ_{th}) is subsequently calculated from the Bragg equation 6.1

.

Material	d (nm)	n_{500}	n_{550}	n_{600}	n_{650}	n_{700}
Polycarbonate [108]		1.6	1.59	1.58	1.58	1.58
Amonil-TiO_2	d	1.884	1.87	1.858	1.849	1.841
PEDOT [109]	70	1.6	1.58	1.57	1.56	1.55
Superyellow [109]	80	2	1.9	1.82	1.78	1.76
Al [108]	200	0.78833 + i5.8655	0.96526 + i6.3996	1.1414 + i6.9256	1.3424 + i7.4737	1.662 + i8.0439
air		1	1	1	1	1

Table 7.2: TMM simulation parameters for given material in thickness and refractive index for 500, 550, 600, 650 and 700 nm in wavelength. The Amonil-TiO_2 thickness (d) is selected as a free parameter for the given refractive index (500, 550, 600, 650, and 700 nm in wavelength). The refractive index of Amonil-TiO_2 is obtained from figure 5.6a.

plot of the theoretical mode extraction angle (θ_{th}) for a grating with period $\bigwedge = 460$ nm at a wavelength of $\lambda = 550$ nm. This calculation will subsequently be used to analyze the emission characteristics obtained from EL and PL experiment.

(a)

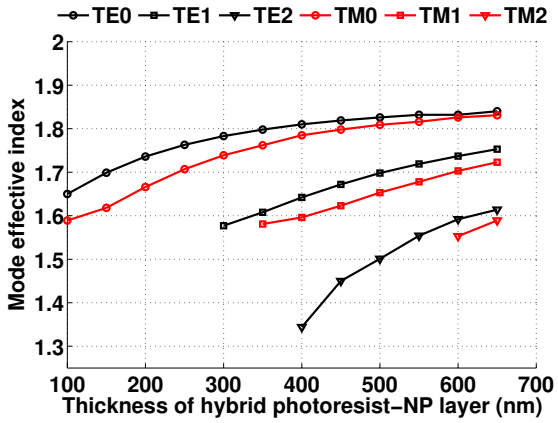

(b)

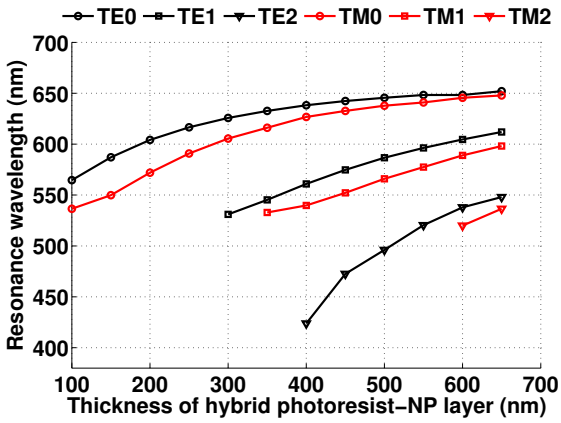

(c)

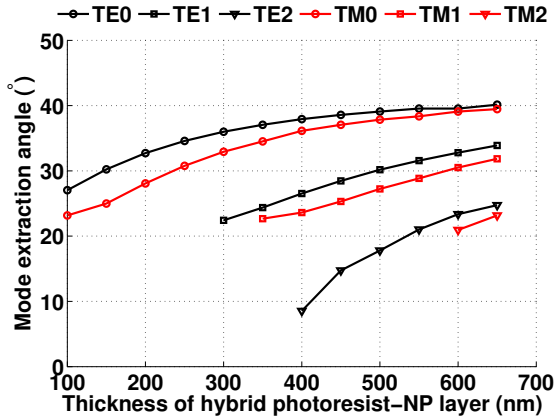

Figure 7.2: (a) Calculated mode effective refractive index (n_{eff}) as a function of the hybrid photoresist-NP 30% for a wavelength of $\lambda = 550$ nm. Since the polycarbonate (PC) substrate has a refractive index of 1.59, the modes with n_{eff} below 1.59 are not truly guided. (b) The resonance wavelength mode as a function of hybrid photoresist-NP thickness is calculated from the Bragg equation for $\bigwedge = 460$ nm, $\theta_{th} = 25°$ and n_{eff} from the figure 7.2a. (c) Theoretical mode extraction angle (θ_{th}) for grating with period $\bigwedge = 460$ nm at a wavelength of $\lambda = 550$ nm.

7.2 Experiment

In this work, the substrate is made from Polycarbonate (PC). The preparation is explained in chapter 3 subsection 3.1.4. PDMS mold fabrication parameters are the same as described in chapter 4 section 4.1. The preparation of hybrid photoresist-NP 30%, spin-coating parameters and stamping process onto substrates are explained clearly in chapter 5. Hybrid photoresist-NP 30% is hydrophobic to the polymer anode (PH500 purchased from H.C.Starck) dispersed in the water. Therefore, 1% volume fluorosurfactant, Zonyl FS-300 purchased from Sigma Aldrich, is added to the polymer anode to increase its wettability [110]. The mixture was shaken for 1 minute and refrigerated for 24 hours. Afterwards the polymer anode mixture was deposited using 0.45 μm PVDF filter (Carl Roth GmbH, Germany), attached to the syringe and spun on at a speed of 2000 rpm onto nanostructured hybrid photoresist-NP films, resulting in a layer thickness of 70 nm. To cure the polymer anode mixture, the substrate was baked in oven at 80 °C for 1 hour. Afterwards, it was partly covered with a stainless steel mask and exposed to oxygen plasma at 200 W for 3 minutes. All processes were carried out in the ambient atmosphere. Since the polymer anode is very hygroscopic [80], all substrates were again baked at 80 °C for 24 hours in the glove box under a nitrogen atmosphere for dehydration. On the following day, 200 nm of silver is evaporated onto the polymer anode serving as a contact pad. Subsequently, the process of light emitting layer and cathode deposition are the same as in the experiment section of chapter 6. Figure 7.3a shows the details of the fabricated OLED device from the top side. The Bragg grating groove direction in this device is also shown by the blue arrow. The bottom side of the device is presented in figure 7.3b. Here, the device has four active areas with 25 mm^2 each. The screw position for the bending mechanism is shown in this picture. The measurement position is defined as x=9.43 mm and y=8.93 mm on one of the OLED areas. In this position, a UV laser at λ = 405 nm, is pointed. Figure 7.3c shows the device architecture in three dimension.

In figure 7.4, the measurement setup of an OLED device under bending conditions is illustrated. In this system, the screw positions (Δz) are adjustable from 0 mm to 2.2 mm. During adjustment Δz, the other edges of the substrate are pinned by two anchors at the same time. The Bragg grating grooves direction, shown by blue arrow, is perpendicular to the rotation angle (θ) direction. In this condition, a UV laser with a 405 nm wavelength is attached to the rotation stage. This setup allows constant illumination during stage rotation. A bare fiber light collection is placed 50 mm away from the device and kept fixed. During angle-resolved measurement, the bare fiber light collection gathers photoluminescence (PL) emissions excited by the UV laser. This setup is also applicable for electroluminescence (EL) measurement. Electrical and electroluminescence (EL) characteristics of the device are measured using source measurement unit (SMU, Keithley).

(a)

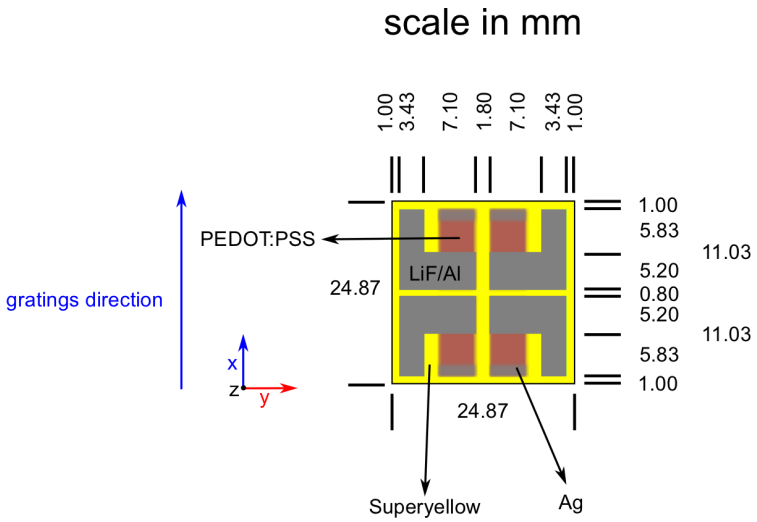

(b)

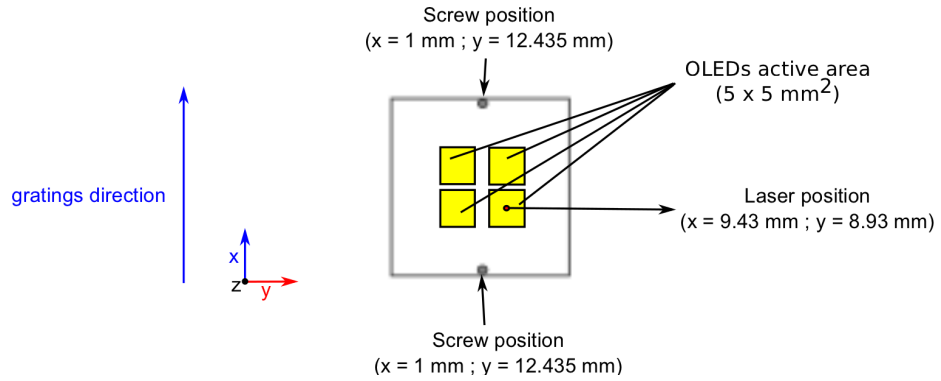

(c)

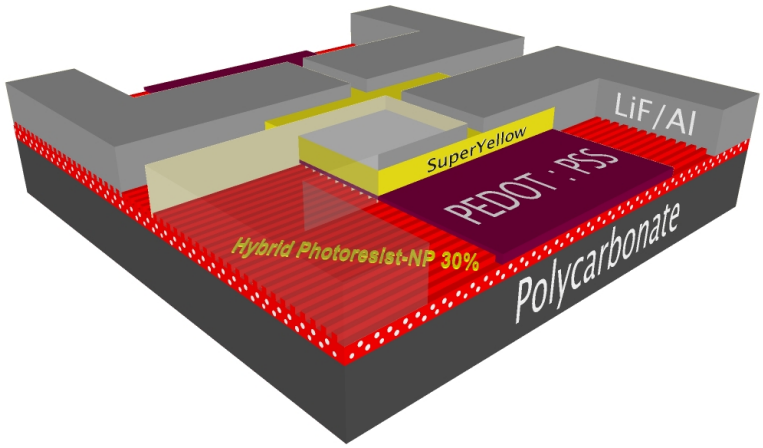

Figure 7.3: An illustration of the OLEDs device dimensions. The top side (a), the bottom side (b), and in three dimension (c).

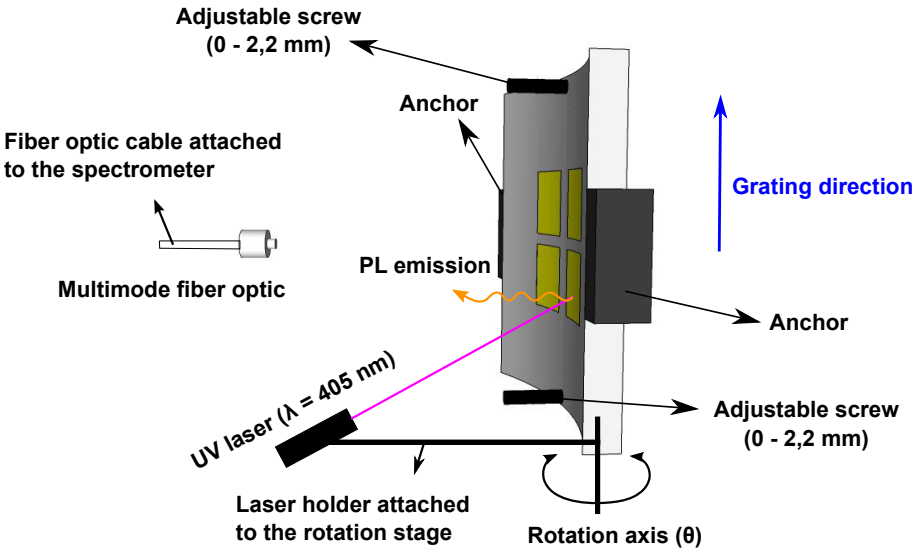

Figure 7.4: A detailed schematic diagram of the measurement setup for OLEDs under bending condition. The Bragg grating direction is perpendicular to the rotation angle (θ) direction. Two anchors are pinned to the substrate to avoid any movement during bending condition that initiated by two adjustable screws. A bare multimode fiber optic is attached 50 mm away from a flat sample substrate and acting as a light collector. In the front of the fiber light collection, a polarizer filter can be attached as presented in figure 2.5 previously. This filter allows either TE or TM mode passing through to the fiber light collector. A UV laser at $\lambda = 405$ nm is attached to the rotation stage that allows a small part of the OLED to be constantly illuminated during angle-resolved measurement. The emission excited by UV laser is gathered by a bare fiber light collection.

7.3 Electroluminescence results

In this work, the electrical characteristics and the electroluminescence of the OLED were observed under flat and bend operation. Depicted in figure 7.5a, the current-voltage (I-V) curve of the OLED shows a small differences for flat and bending conditions. Figure 7.5b is a photograph of an OLEDs device in bend operation. Wavelength- and angle-resolved electroluminescence measurements were performed using the same goniophotometer setup as shown in figure 7.4. In this situation, a constant electrical current (I) is applied. As a result the active area (5 x 5 mm^2) of an OLED is emitted. Afterwards, the emitted light is gathered by a bare fiber light collection which is placed at 50 mm away from the sample. Before the light travels into a bare fiber light collection, it is filtered by a TE polarizer. Therefore only TE modes are allowed to pass and travel to the spectrophotometer. In figure 7.5c the electroluminescence emission is shown for a flat substrate. On the other hand, figure 7.5d shows a substrate bent by screws displacement of $\Delta z = 1.48$ mm. Both pictures show that the outcouple waveguide mode by Bragg grating is clearly recognized.

The leaking mode positions are analyzed and simulated by TMM simulation using the given parameters in table 7.2. As previously plotted theoretically in figure 7.2a, three TE (TE_0, TE_1, TE_2) modes are predicted to occur in the spectrum. Since the PC substrate has a refractive index of 1.59, the modes with n_{eff} below 1.59 are not truly guided. As a consequence, only TE_0 and TE_1 modes are predicted to occur in the emission spectrum. From the mode positions, the hybrid NP-photoresist layer of 450 nm is fitted. The theoretical extraction angles (θ_{th}) of the TE_0 and the TE_1 are plotted. The calculated and the experimental result show good agreement. Observing figure 7.2a and figure 7.2b, the extracted resonance peak for bend operation has higher relative intensity to the flat operation. This effect occurs throughout my samples and is recorded in appendixes (C,D). The EL improvement operation under strain is reported in [111]. A further investigation should be carried out to explain this phenomena.

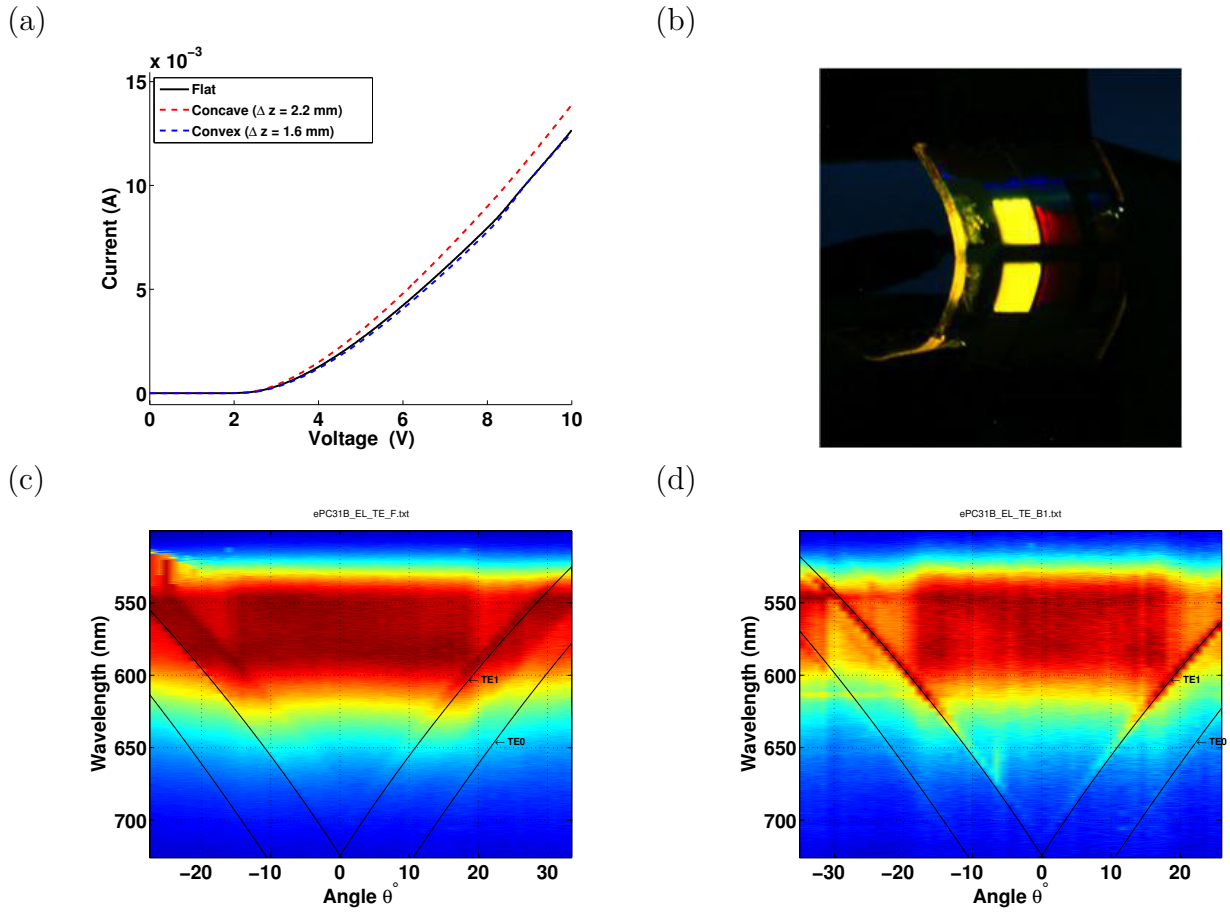

Figure 7.5: (a) Electrical characterization of the device under flat, concave, and convex operation. The I-V curve plot shows slight differences for flat and bend operation. (b) A photograph of OLEDs under bending operation. (c) The electroluminescence emission spectrum for flat and bend operation (d). Both picture (c-d) is normalized to the intensity. The black lines indicate theoretical mode extraction angle for TE_0 and TE_1. The calculated extraction angle shows good agreement to the experiment for hybrid NP-photoresist layer of 450 nm.

7.4 Photoluminescence results

As discussed previously in section 7.1, the strain is in-homogeneous across the OLED device for the used bending mechanism. Therefore, a photoluminescence measurement is performed. As depicted in figure 7.4 and figure 7.1, a UV laser at 405 nm excites a small spot at the position in x = 9.43 mm and y = 8.93 mm. In that position, one can compare quantitatively the effect of Bragg grating slab deformation in experiment and theory. The two examples of PL spectra as a function of angle are shown in figure 7.6. Figure 7.6a presents a PL spectra for flat condition ($\Delta z = 0$) and figure 7.6b for bend condition ($\Delta z = 2.165$ mm). In both images, the leaking mode is clearly visible. In this experiment, the hybrid photoresist layer thickness is also fitted to 450 nm. Comparing photoluminescence emission for flat and bend condition, TE_2 mode appears in the bending position. The experiment and the calculated extraction angle shows good agreement. However, the leaking mode for both conditions is dominated by TE_1 mode. Therefore, it is reasonable to analyze the angle- and wavelength-dependent extraction of the TE_1 mode. Since the wavelength resolution in the measurement is far better than angular resolution, a fixed emission angle has been chosen to analyze the results. In figure 7.7a, the resonance wavelength is plotted as a function of central deflection for a resonance extraction angle of 25° The theoretical value of changing the refractive index of the mode and the grating period in deformed condition is described in section 7.1. The comparison of experimental and theoretical calculation for change in resonance wavelength as a function of central deflection is plotted in figure 7.7a. The observed experimental and theoretical values have a deviation average range of 1.11% for the given central deflection. As presented in figure 7.7b, the Bragg grating deformation results in the changes of resonance wavelength for all measured fixed angles. The resonance wavelength changes increase as a function of the central deflection. The theoretical resonance wavelength change for extraction angle of 25° is located above experimental resonance wavelength change in 15°, 20°, 25°, and is slightly above the 30° line.

The deviations are in the manner of screw displacement accuracy and the extraction of the experimental data. The theoretical description of the Bragg grating deformation presented in section 7.1 verifies the experimental results, therefore the fundamental theory descriptions are a suitable basis for predicting the behavior of the fabricated flexible grating OLEDs.

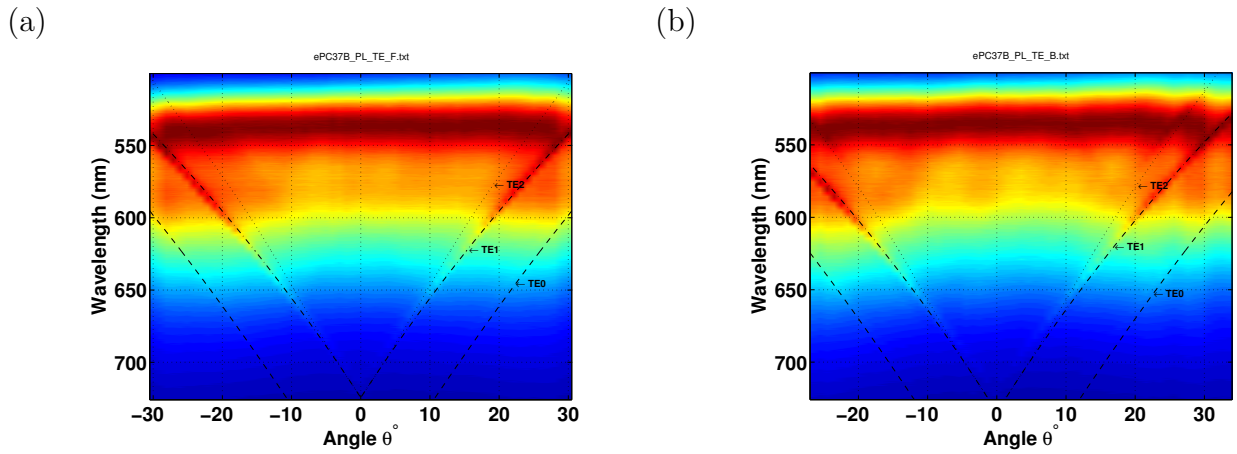

Figure 7.6: The images of photoluminescence intensity of flexible grating OLEDs as a function of angle and wavelength. The intensity is normalized to the maximum intensity at a given angle. (a-b) A flat substrate ($\Delta z = 0$) (a) and a bend condition ($\Delta z = 2.165$ mm) are obtained by screw displacement. The resonance wavelengths are clearly visible for both strain conditions. A small shift in the resonance wavelength caused by strain is recognized.

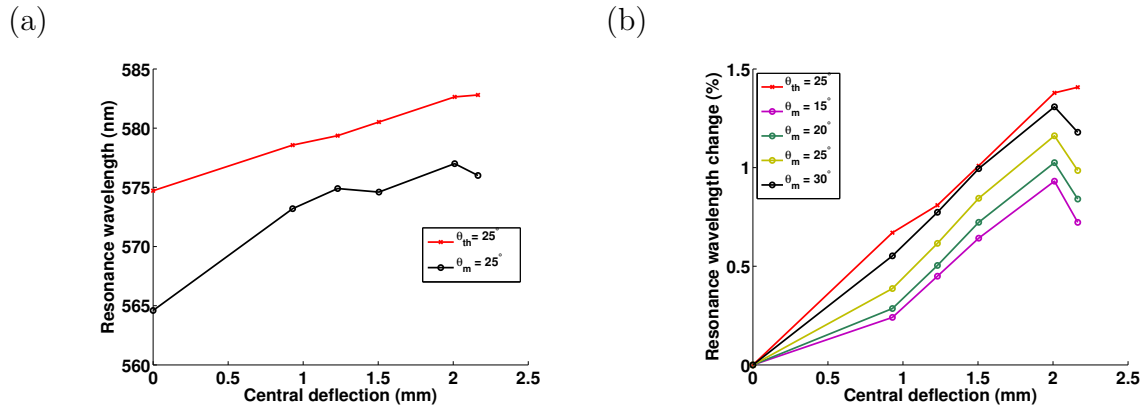

Figure 7.7: (a) Theoretical and experimental resonance wavelength of the TE_1 mode as a function of the central deflection (Δz). These are obtained by screw displacement as shown in 7.1b. The emission angle for this graph is fixed at 25°. A comparison of the experimental value and the theoretical prediction of resonance wavelength change. The theoretical prediction is obtained from the Bragg equation and the effective refractive index is given in table 7.1. (b) The change of relative resonance wavelength under deflection for extraction angles of 15°, 20°, 25°, and 30°.

7.5 Conclusion in this chapter

A combination of UV-NIL technology and high refractive index hybrid NP-photoresist offers not only a simplification in the fabrication scheme compared to a well known technique such as the work in Geyer et.al [5] and Riedel et.al [6]. In addition, it allows a fabrication of 1-D photonic grating (Bragg grating) into flexible OLEDs for light extraction. The external loads change the Bragg grating geometry in the fabricated flexible OLEDs and lead to a shift in the grating resonance wavelength. The theoretical predictions, in the manner of extraction angle, show good agreement with the experimentally fabricated nanostructured flexible OLEDs for EL and PL emission. TMM simulation reveals that n_{eff} for TE_1 is almost constant for a given deflection range. Combining the results of TMM simulation and Bragg equation one can predict that the shift of resonance wavelength is mainly caused by the change in Bragg grating periodicity, while the substrate was exposed under bend conditions. The theoretical prediction from section 7.1 represents a good basis for predicting the behavior of fabricated flexible nanostructtructured OLEDs on the deformation state. Departing from this fundamental theory, I propose a finite element modelling (FEM) to simulate and predict the behavior of fabricated flexible nanostructured OLEDs in a better way. Flexible hybrid NP-photoresist has wide application. One example is in optical tunable devices.

Chapter 8

Conclusions

The aim of this work is to integrate one-dimensional photonic crystal slabs (Bragg gratings) into OLED devices as a light extractor. The difference to previous work in the field is the utilization of ultraviolet nanoimprint lithography technology (UV-NIL) for 1-D photonic grating fabrication. This technology offers a shorter fabrication route and a relative reduction of the production cost. The result is reproducible and the replicated structure covers a large area. However, there are many methods in UV-NIL technology for delivering the structure in the master template to the substrate or thin film that we require. In the most successful technique, an ITO-free OLED is fabricated onto AMONIL resist. The emitted light from the device under voltage bias confirmed that this architecture worked properly. In this work, two methods to transfer the structure onto photoresist-coated glass have been presented. One method is employing master stamp glass, as a working stamp, to deliver the structure to the photoresist-coated glass directly. Since the reproducibility is very low, one can conclude that this method is not suitable for this study. The surface in the substrate and working stamp glass is rough, which is indicated by the Newton's ring that appeared when the working stamp glass and the glass substrate were stacked together during the printing step. Immediately after exposure to the UV source in the curing step, the area covered by Newton's ring was destroyed. This applies for mr-UVCur21 and AMONIL resist 4. To compensate for the waviness of the glass substrate, an elastomeric polymer mold (PDMS) was chosen. This method produced a successful result because the replication covers a large area and is reproducible.

A high refractive index material surrounded by low refractive index materials is needed to facilitate waveguide mode emitted from the OLEDs. Introducing 1-D photonic crystal slabs in this material may scatter the waveguide mode, which increases the external efficiency of the OLEDs. The natural refractive index of AMONIL resist is 1.5. Since the surrounding materials have a similar refractive index to the AMONIL resist, no waveguide mode would appear in this layer. There are two possibilities for achieving this criterion. One is to transfer the nanostructured AMONIL resist to the high refractive index film (Ta_2O_5) by dry etching. In this work, Inductively Coupled Plasma-Reactive Ion Etching (ICP-RIE) technology was used. Pattern transfer using this technique is very promising. However, the technique is not straightforward and some parameters must be adjusted in order to obtain an optimum result. Since there are a lot of process parameters, the degree of freedom in terms of optimization is still broad and further investigation should follow.

Another alternative is to blend TiO_2 nanoparticles (NP) to the AMONIL resist in order to increase the refractive index. TiO_2 NP's refractive index is approximately 2.5. A blend of 1%, 2%, 3%, 5%, 10%, 20%, and 30% TiO_2 NP may increase the refractive index up to 1.869 at 550 nm. Thickness characterizations are carried out by profilometer and reflectometer technique. The thickness values are in the deviation range. The refractive index is characterized by UV-Vis spectrometer. Swanepoel simulation is performed to reveal the refractive index from the experimental transmission spectra. Refractive index obtained for wavelength range of interest from 520-650 nm (Superyellow emission spectrum) is 1.878-1.84.

Hybrid photoresist-NP 30%, sandwiched by low refractive index materials, allows radiation energy to propagate in this layer. Placing 1-D photonic structure (Bragg grating) in this layer results in coupling out the waveguide mode into leaking mode. The emissions of photoluminescence (PL) and electroluminescence (EL) techniques confirm the advantage of hybrid photoresist-NP 30% once embedded in OLED devices. The emission spectrum shows a sharp peak and depends on the angle. This experiment also proved that when a slab waveguide has similar refractive index to the surroundings (glass substrate and PEDOT:PSS film), no concentrated radiation energy will propagate in this system. Grating periodicity in this layer is 370 nm. Putting the number into Bragg equation, the effective refractive index in this system, experimentally, is 1.59 at 591.8 nm in the wavelength. Transfer matrix simulation (TMM) is performed to calculate theoretical n_{eff} as a function of wavelength. The experimental and theoretical results show good agreement. Electrical characteristics differ from one sample to another, which is probably caused by internal efficiency. The advantage of hybrid photoresist-NP is not only its straightforwardness and the elimination of complex fabrication route schemes but also its potential for application on the flexible substrate as a slab waveguide.

A combination of UV-NIL technology and high refractive index hybrid photoresist-NP offers not only a simplification in fabrication route scheme compared to a well known technique such as the work in Geyer et. al [5] and Riedel et. al [6], but allows above all the fabrication of 1-D photonic grating (Bragg grating) into flexible OLEDs for light extraction. The external load changes the Bragg grating geometry in the fabricated flexible OLEDs and leads to a shift in the grating resonance wavelength. The theoretical predictions, such as extraction angle, show good agreement with the experimentally fabricated nanostructured flexible OLEDs for EL and PL emission. TMM simulation reveals that n_{eff} for TE_1 is almost constant for a given deflection range. Combining the result from TMM simulation and Bragg equation, one can predict that the shift of the resonance wavelength is mainly caused by the change in Bragg grating periodicity while the substrate was exposing under bend condition. The theoretical prediction from section 7.1 provides a good basis for predicting the behavior of fabricated flexible nanostructured OLEDs in the deformation state. Departing from this fundamental theory, a finite element modelling (FEM) to simulate and predict the behavior of fabricated flexible nanostructured OLEDs in a better way is proposed. As an alternative to OLED applications, flexible hybrid photoresist-NP is potentially useful in optical tuneable device.

Appendix A

Nanoimprint using mask aligner (Süss MicroTec, MA-6)

A.1 Glass master stamps

Table A.1: Stamps

Stamps	periodicities (nm)
a	300
b	350
c	460
S3	370
S7	370
10	370
12	370
13	350
14	350
15	350

A.2 Chuck parameters

Table A.2: Chuck stack in this work is 2 mm

Chuck level	Stack thickness (mm)
0	6.2 - 7.3
1	7.2 - 8.3
2	8.2 - 9.3

A.3 Glass to glass imprint parameters

Table A.3: Imprint Parameters. Adhesion and Photoresist are mr-APS1 and mr-UVcur21

Sample no.	Chuck level	Vac Sealing (bar)	Process chamber (bar)	Pressure Chamber (bar)	Exposure (sec)	Results
40	1	1	-0.5	0.7	30	- some photoresist still exist - not uniform - some pattern was created - stamp and substrate couldn't separated
38	1	0.6	-0.5	0.6	30	not uniform, sticking
41	1	0.7	-0.5	0.7	30	not uniform, sticking
39	1	0.8	-0.6	0.6	30	not uniform, sticking

Table A.4: Imprint Parameters. Adhesion and Photoresist are mr-APS1 and mr-UVcur21. Oxygen plasma treatment onto substrate for 15 min.

Sample no.	Chuck level	Vac Sealing (bar)	Process chamber (bar)	Pressure Chamber (bar)	Exposure (sec)	Results
9	1	0.7	-0.8	0.7	30	separated, ununiform
10	1	0.7	-0.8	0.7	30	sticking, ununiform
11	1	0.6	-0.5	0.6	30	sticking, ununiform

Table A.5: Imprint parameters for mr-UVcur21 pre-treated with mr-APS1. VS=Vacuum Sealing, Proc. C=process chamber, Press. C= Pressure Chamber, Exp = Exposure, C.L= Chuck Level, S. N =Sample Number.

S. N	C. L	Imprint process				Separation process			
		VS (bar)	Proc. C (bar)	Press. C (bar)	Exp (sec)	VS (bar)	Proc. C (bar)	Press. C (bar)	Results
12	1	0.7	-1	0.7	120	0.8	0	-0.6	sticking, ununiform
13	1	0.7	-1	0.7	120	0.8	0	-0.6	sticking, ununiform
14	1	0.7	-1	0.7	120	0.8	0	-0.6	sticking, ununiform
15	1	0.7	-1	0.7	120	0.8	0	-0.6	sticking, ununiform

Table A.6: Imprint parameters for Amonil MMS4 pre-treated with Amoprime. VS=Vacuum Sealing, Proc. C=process chamber, Press. C= Pressure Chamber, Exp = Exposure, C.L= Chuck Level, S. N =Sample Number.

S. N	C.L	Imprint process				Separation process						
						T.evacuation			N2 Purge T			
		VS (bar)	Proc. C (bar)	Press. C (bar)	Exp. (sec)	VS (bar)	Proc. C (bar)	Press. C (bar)	VS (bar)	Proc. C (bar)	Press. C (bar)	Results
18	1	0.8	-1	0.7	180	0.8	-1	-0.6	0.85	0	-0.6	ununiform
17	1	0.8	-1	0.5	180	0.8	-1	-0.6	0.8	0	-0.6	ununiform
16	1	0.8	-1	0.5	180	0.8	-0.35	-0.6	0.8	0.1	-0.6	ununiform
19	1	0.8	-1	0.6	180	0.8	-0.35	-0.6	0.8	0.1	-0.6	ununiform

Table A.7: Imprint parameters for Amonil MMS4 without Amoprime. Substrate Stamp 15 is used. An anti-sticking layer, BGL GZ-63, deposited using spin coating technique onto stamp 15. It was stored in the glovebox for 48 hours. VS=Vacuum Sealing, Proc. C=process chamber, Press. C= Pressure Chamber, Exp = Exposure, C.L= Chuck Level, S. N =Sample Number.

S. N	C.L	Imprint process				Separation process						
						T.evacuation			N2 Purge T			
		VS (bar)	Proc. C (bar)	Press. C (bar)	Exp (sec)	VS (bar)	Proc. C (bar)	Press. C (bar)	VS (bar)	Proc.C (bar)	Press. C (bar)	Results
P8	1	0.8	-0.7	0.7	120	0.8	-1	-0.6	0.85	-0.2	-0.6	Sticking, un-uniform
P7	1	0.7	-1	0.7	120	0.8	-1	-0.6	0.8	0	-0.6	Sticking, un-uniform
P6	1	0.75	-0.8	0.8	120	0.7	-0.7	-1	0.8	0	-0.7	Sticking, un-uniform
P5	1	0.75	-0.8	0.8	120	0.7	-0.7	-1	0.8	0	-0.7	Sticking, un-uniform

Appendix B

Fabrication protocols

B.1 Nanostructured PLED on rigid OLEDs

Table B.1: Process parameters for nanostructured rigid PLED

Nr.	Process step	Process parameter
1	Substrate dehydration	Hotplate, 10 min, 160° C, 2 min cooling
2	Spincoating Amoprime	Program Amonil: 30 sec, 3000 rpm
3	Softbake Amoprime	Hotplate: 2 min at 115° C, 2 min cooling
4	Spincoating Amonil	160 μl per substrate. Program Amonil: 30 sec, 3000 rpm
5	Spin coating Amonil + TiO_2 3%	160 μl per substrate. Program Amonil: 30 sec, 3000 rpm
6	Spin coating Amonil + TiO_2 30%	160 μl per substrate. Program Amonil: 30 sec, 3000 rpm
7	PDMS stamp	PDMS mold from M1.
8	Exposure	UV source, 3 min pre-heated, 3 min exposure, distance 10 cm.
9	Plasma treatment	8 sccm O_2, 100 W, 1 min
10	Spincoat PEDOT:PSS (PH500) + DMSO 10%	Program PEDOT
11	Hardbake	Hotplate: 5 min 150° C
12	Structuring PEDOT:PSS (PH500) + DMSO 10% by plasma	8 sccm O_2, 200 W, 3 min. Mask M08-1.2
13	Ag evaporation as a contact pad	30 nm, Mask M03-2.1
14	Spin coating Super Yellow	P2 in glovebox. 5 sec - 500 rpm 60 sec - 1000 rpm
15	Lif evaporation	1 nm thick
16	Al evaporation	200 nm thick

B.2 Nanostructured PLED on flexible substrate

Table B.2: Process parameters for nanostructured flexible PLED

Nr.	Process step	Process parameter
1	PDMS mixing	Sylgard 184, Curing agent, a mixture of 8:1 for 20 min, level 1-2 (IKA Tube Drive) PDMS onto template casting.
2	Evacuation	15-20 min in Vacuum, evacuate until no bubbles in the PDMS mixture.
3	Cured	20 min at 130° C in Oven.
4	Cutting	Cured PDMS detached from the template carefully and cut.
5	Cleaning Polycarbonate	Isopropanol, 15 min in Ultrasonic bath level 3.
6	Spincoating Amonil + TiO_2 30%	160μl per substrate, Program Amonil: 30 sec, 3000 rpm.
7	PDMS stamp	PDMS mold from stamp C.
8	Exposure	UV source, 3 min pre-heated, 3 min exposure, distance 10 cm.
9	PEDOT:PSS + DMSO 10% + Zonyl FS 300 Fluorosurfactant 1%	Shake and store in the refrigerator for 2 hours
10	Spin coating PEDOT:PSS modification with PVDF filter	Program PEDOT: 5 sec - 500 rpm 60 sec - 2000 rpm
11	Hardbake	1 hour at 80° C in oven.
12	Structuring PEDOT:PSS modification by plasma treatment.	8 sccm O2, 200 W, 3 min. Mask M08-1.2
13	PEDOT:PSS dehydration in glove box	1 day at 80° C on hotplate.
14	Ag evaporation as contact pad	30 nm, Mask M03-2.1
15	Spincoating SuperYellow	Program SY in glovebox: 5 sec - 500 rpm, 60 sec - 2000 rpm.
16	LiF evaporation	1 nm, Mask M06-1
17	Al evaporation	200 nm, Mask M06-1

Appendix C

Electroluminescence measurements

C.1 Polycarbonate probe number 17

$\bigwedge$= 370 nm

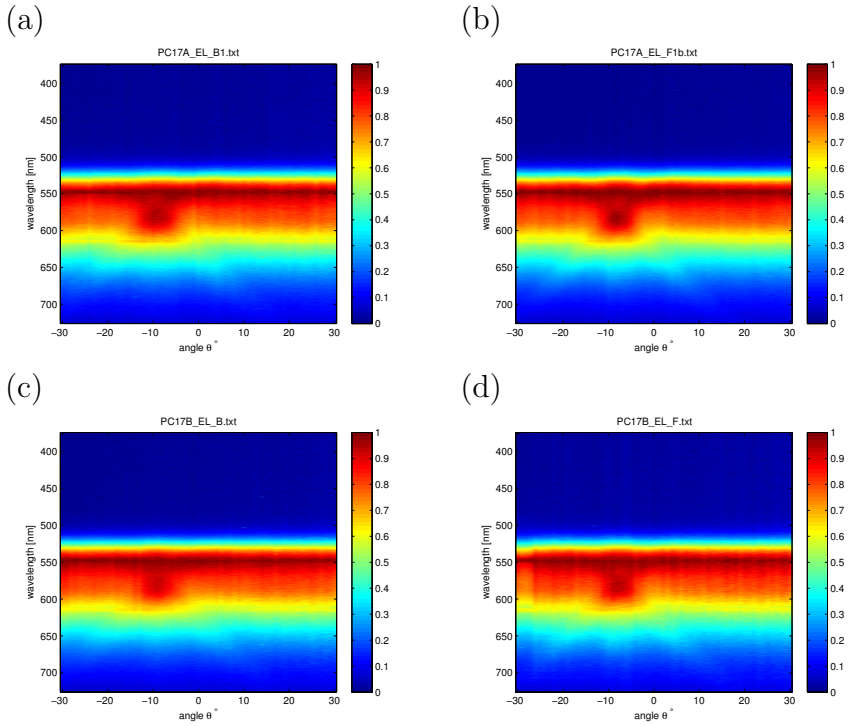

Figure C.1: Electroluminescence measurement with TE filter attached. SiO waveguide (a-d). (a,c). Concave condition (a,c). a.) $\Delta z = 2.09$ mm, b). $\Delta z = 0$, c.) $\Delta z = 2.09$ mm, and d.) $\Delta z = 0$.

C.2 Polycarbonate probe number 24

$\bigwedge$= 370 nm

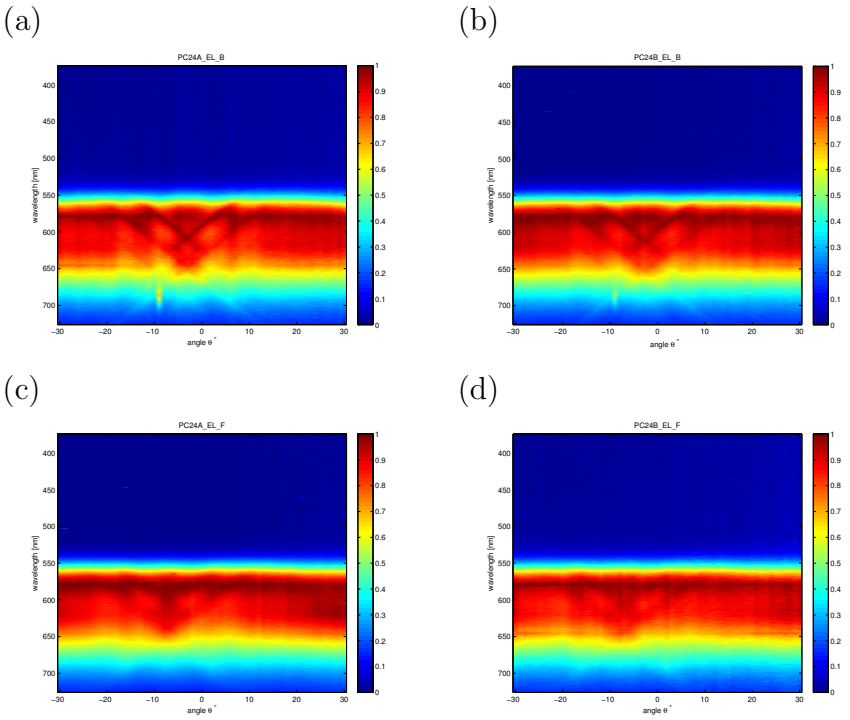

Figure C.2: Electroluminescence measurement without TE filter. (a-b) Concave condition ($\Delta z = 2.08$ mm, (c-d) Flat condition ($\Delta z = 0$).

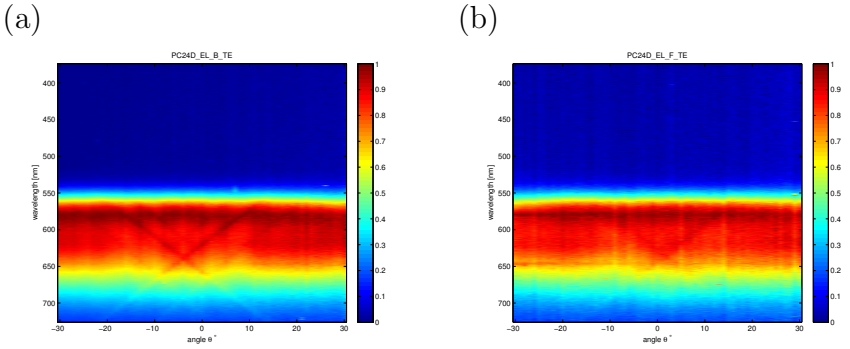

Figure C.3: Electroluminescence measurement with TE filter attached. Concave condition. a.) $\Delta z = 2.07$ mm, b). $\Delta z = 0$).

C.3 Polycarbonate probe number 25

$\bigwedge$= 370 nm

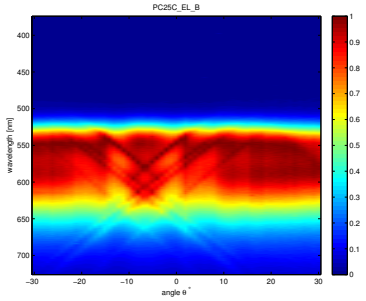

Figure C.4: Electroluminescence measurement without TE filter. Concave condition (Δz = 1.95 mm).

(a) (b)

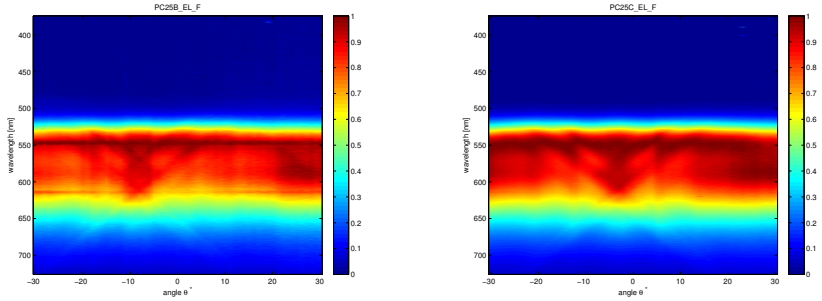

Figure C.5: Electroluminescence measurement without TE filter. Flat condition (Δz = 0).

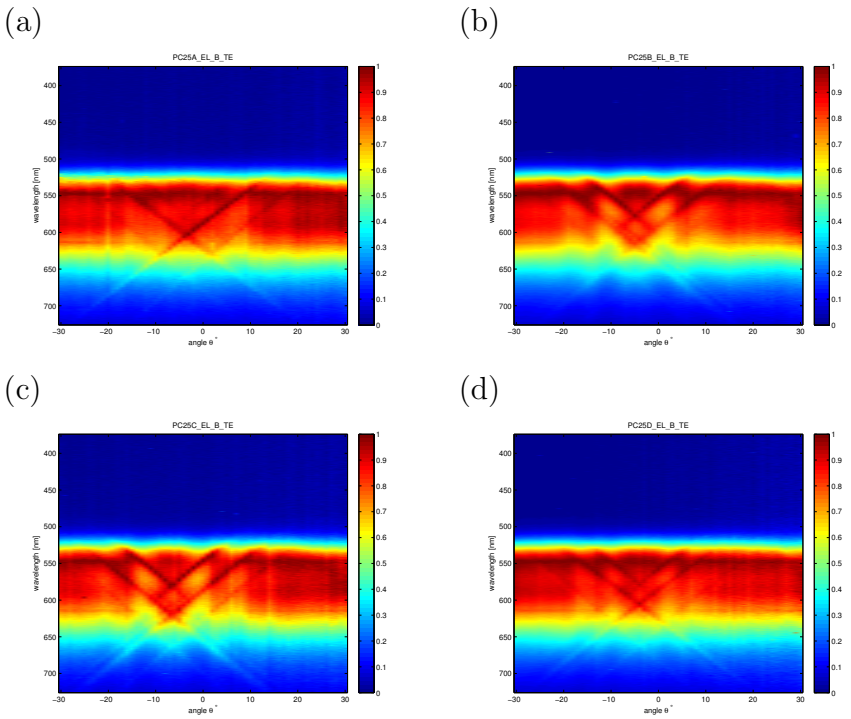

Figure C.6: Electroluminescence measurement with TE filter attached. Concave condition. a.) $\Delta z = 1.98$ mm, b). $\Delta z = 1.98$ mm, c.) $\Delta z = 1.95$ mm, and d.) $\Delta z = 2.01$ mm.

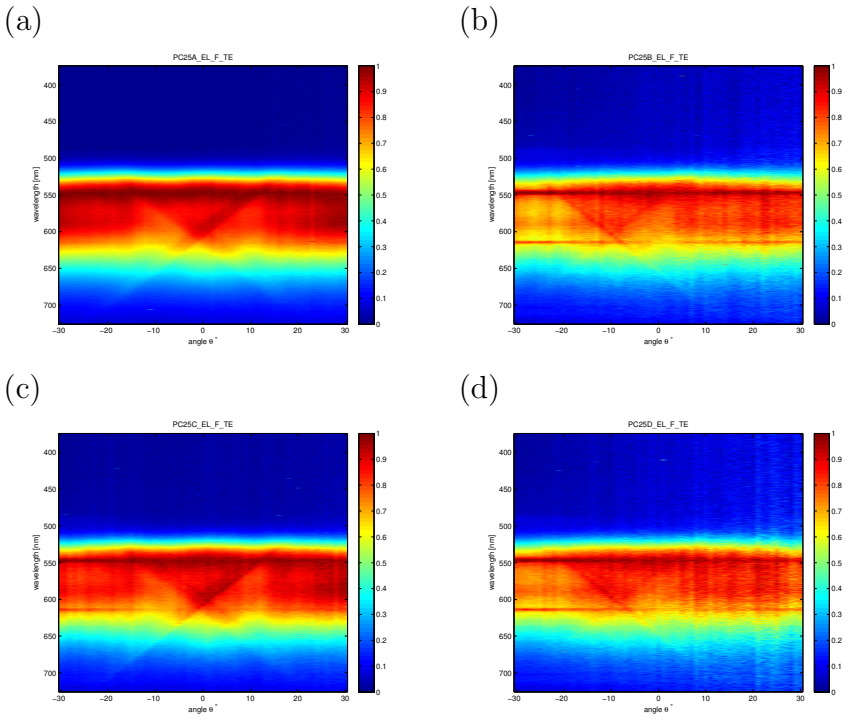

Figure C.7: Electroluminescence measurement with TE filter attached. Flat condition. ($\Delta z = 0$).

C.4 Polycarbonate probe number 26

$\bigwedge$= 370 nm

(a) (b)

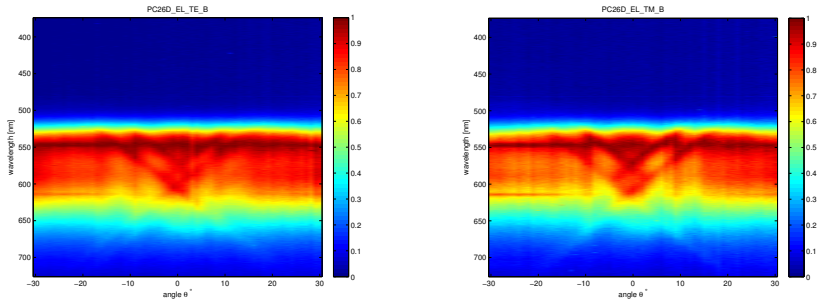

Figure C.8: Electroluminescence measurement with TE filter. Convex condition. (Δz = 1.6 mm).

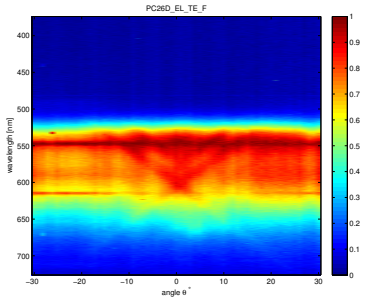

Figure C.9: Electroluminescence measurement with TE filter. Flat condition (Δz = 0).

C.5 Polycarbonate probe number 27

$\bigwedge$= 370 nm

(a)

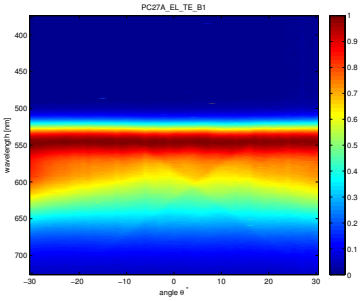

(b)

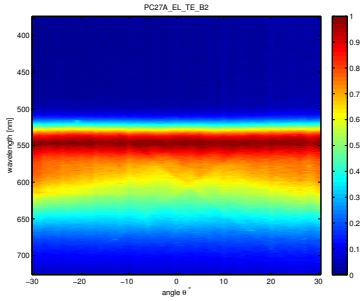

(c)

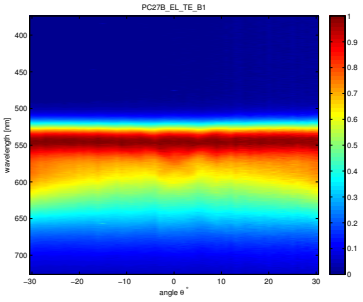

(d)

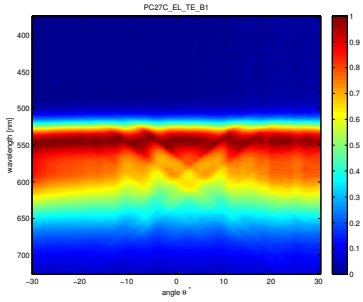

(e)

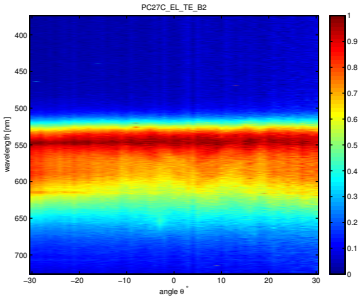

Figure C.10: Electroluminescence measurement with TE filter. Concave condition. a.) $\Delta z = 1.33$ mm, b.) $\Delta z = 2.14$ mm, c.) $\Delta z = 1.26$ mm, d.) $\Delta z = 2.14$ mm, and e.) $\Delta z = 1.26$ mm.

C.6 Polycarbonate probe number 30

$\bigwedge$= 460 nm

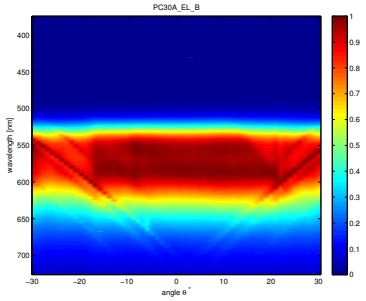

Figure C.11: Electroluminescence measurement without TE filter. Concave condition. (Δz = 2.14 mm).

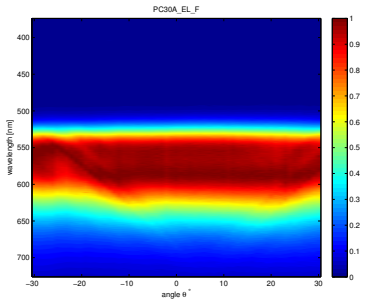

Figure C.12: Electroluminescence measurement without TE filter. Flat condition. (Δz = 0).

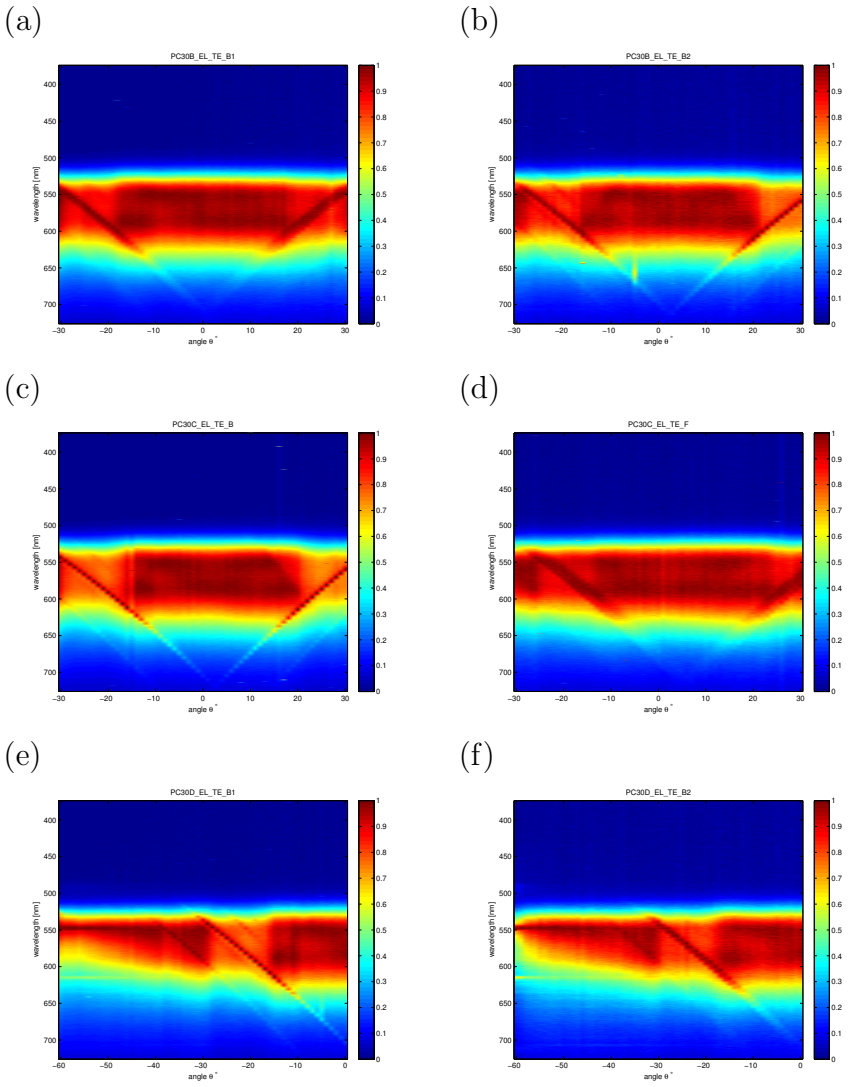

Figure C.13: Electroluminescence measurement with TE filter. Concave condition. a.) $\Delta z = 0.76$ mm, b.) $\Delta z = 2.02$ mm, c.) $\Delta z = 2.14$ mm, d.) $\Delta z = 0$, e.) $\Delta z = 2.02$ mm, and f.) $\Delta z = 1.25$ mm.

C.7 Polycarbonate probe number 31

$\bigwedge$= 460 nm

(a)

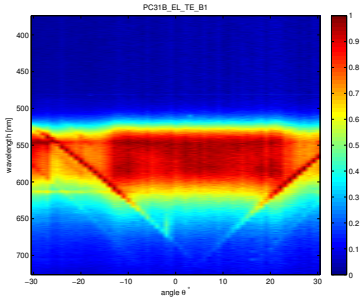

(b)

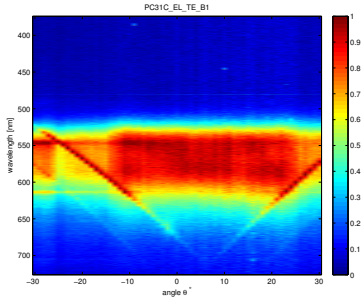

(c)

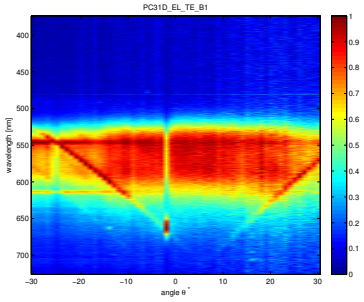

Figure C.14: Electroluminescence measurement with TE filter attached. Concave condition. a.) $\Delta z = 1.88$ mm, b). $\Delta z = 1.88$ mm, and c.) $\Delta z = 1.95$ mm.

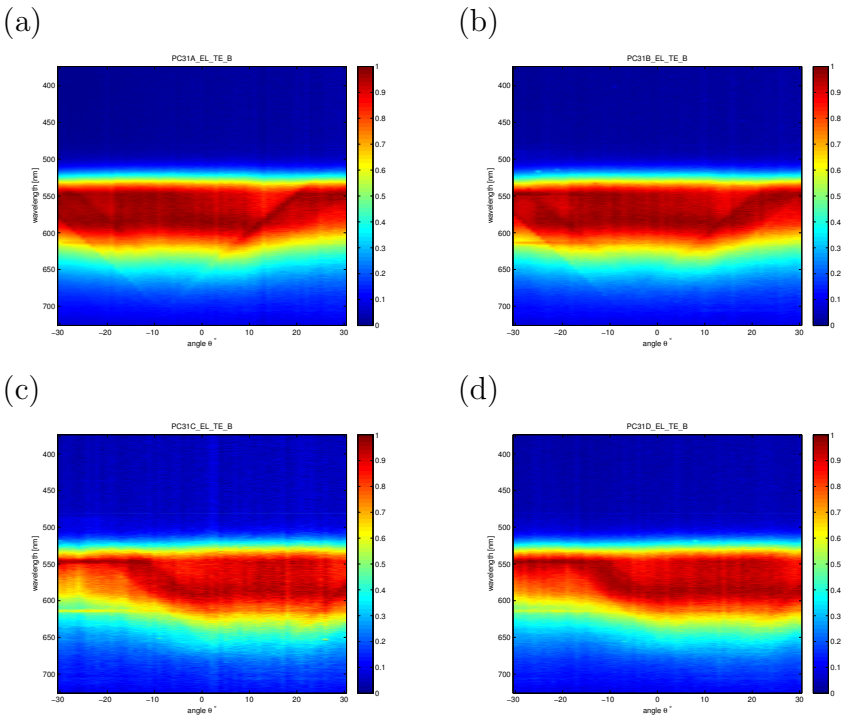

Figure C.15: Electroluminescence measurement with TE filter attached. Convex condition. a.) $\Delta z = 1.95$ mm, b). $\Delta z = 1.48$ mm, c.) $\Delta z = 1.76$ mm, and d.) $\Delta z = 1.95$ mm.

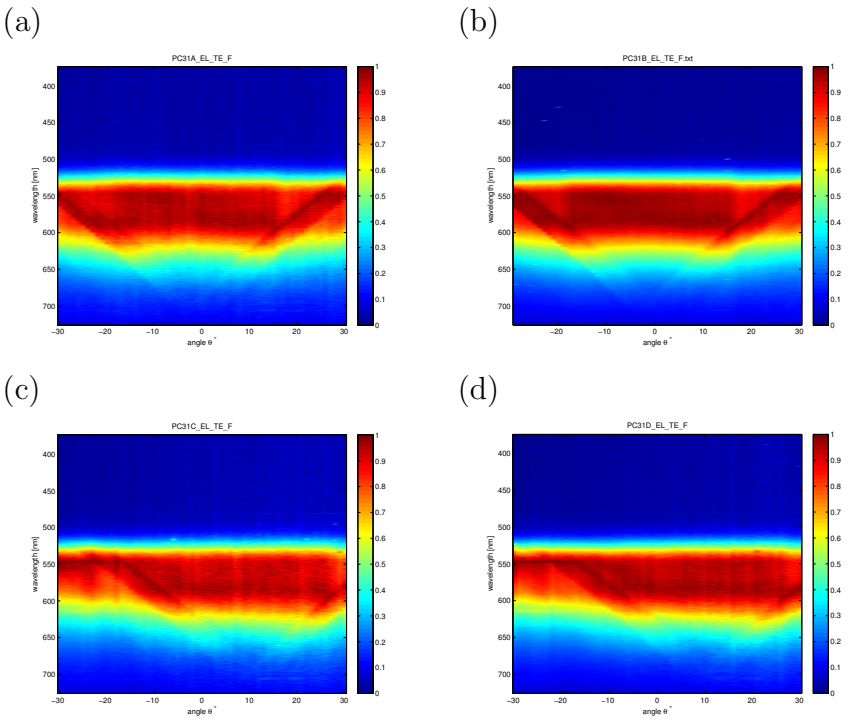

Figure C.16: Electroluminescence measurement with TE filter attached. Flat condition. ($\Delta z = 0$).

C.8 Polycarbonate probe number 33

$\bigwedge$= 460 nm

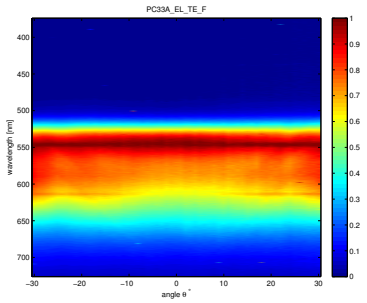

Figure C.17: Electroluminescence measurement without TE filter. Flat condition ($\Delta z = 0$).

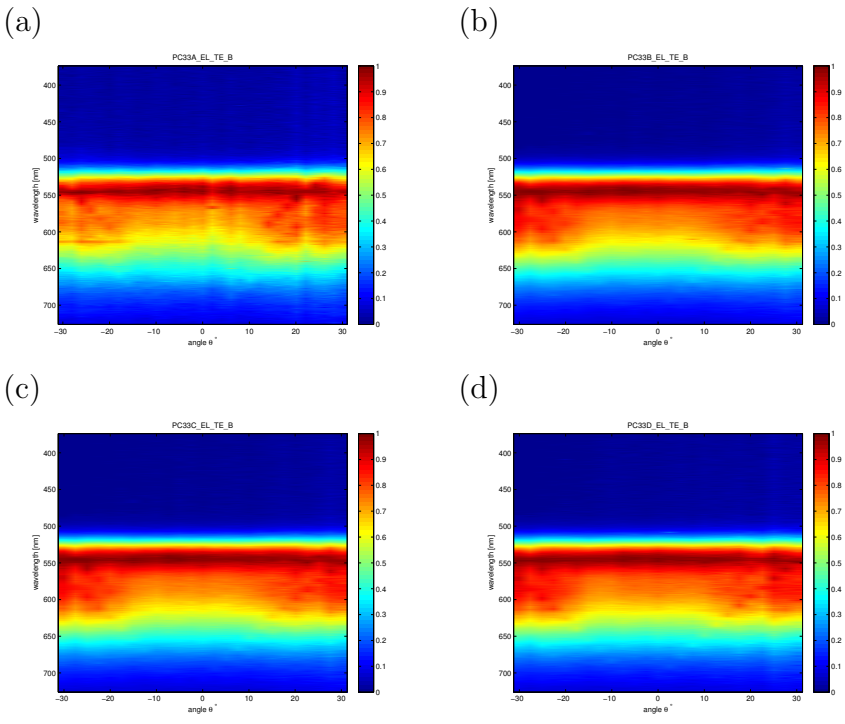

Figure C.18: Electroluminescence measurement with TE filter attached. Concave condition ($\Delta z = 2.14$ mm).

(a) (b)

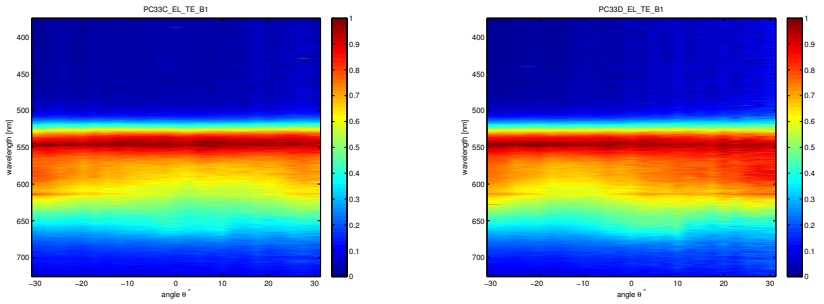

Figure C.19: Electroluminescence measurement with TE filter attached. Convex condition ($\Delta z = 1.53$ mm).

C.9 Polycarbonate probe number 34

$\bigwedge$= 460 nm

(a)

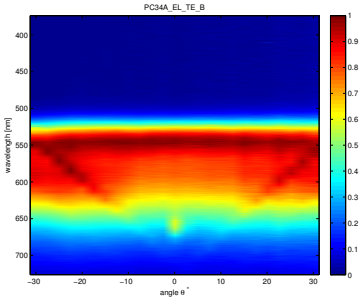

(b)

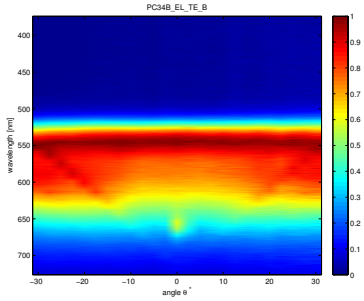

(c)

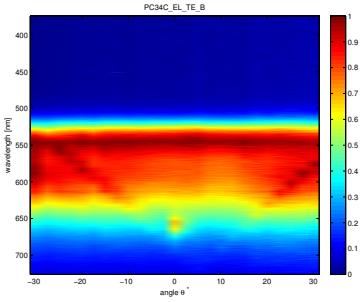

Figure C.20: Electroluminescence measurement with TE filter attached. Convex condition ($\Delta z = 1.67$ mm).

C.10 Polycarbonate probe number 35

$\bigwedge$= 460 nm

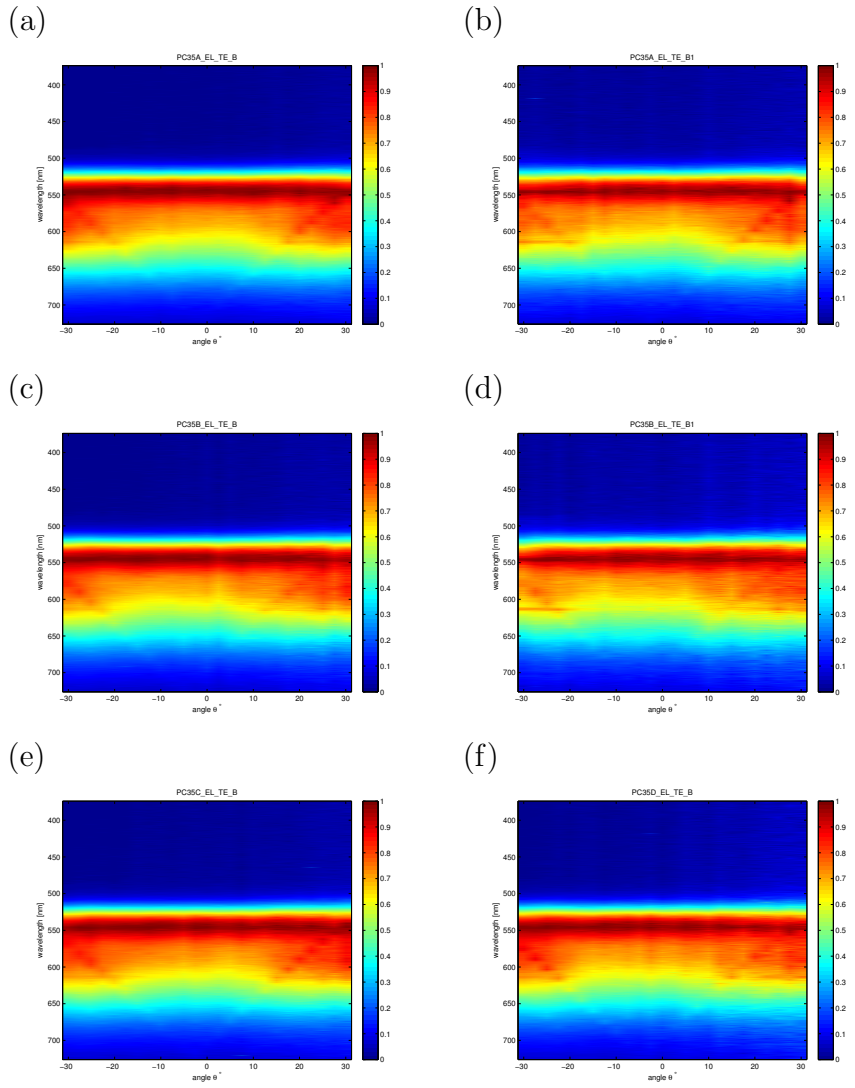

Figure C.21: Electroluminescence measurement with TE filter. Concave condition. a.) $\Delta z = 1.35$ mm, b.) $\Delta z = 1.5$ mm, c.) $\Delta z = 1.35$ mm, d.) $\Delta z = 1.5$ mm, e.) $\Delta z = 1.62$ mm, and f.) $\Delta z = 1.9$ mm.

C.11 Polycarbonate probe number 36

$\bigwedge$= 460 nm

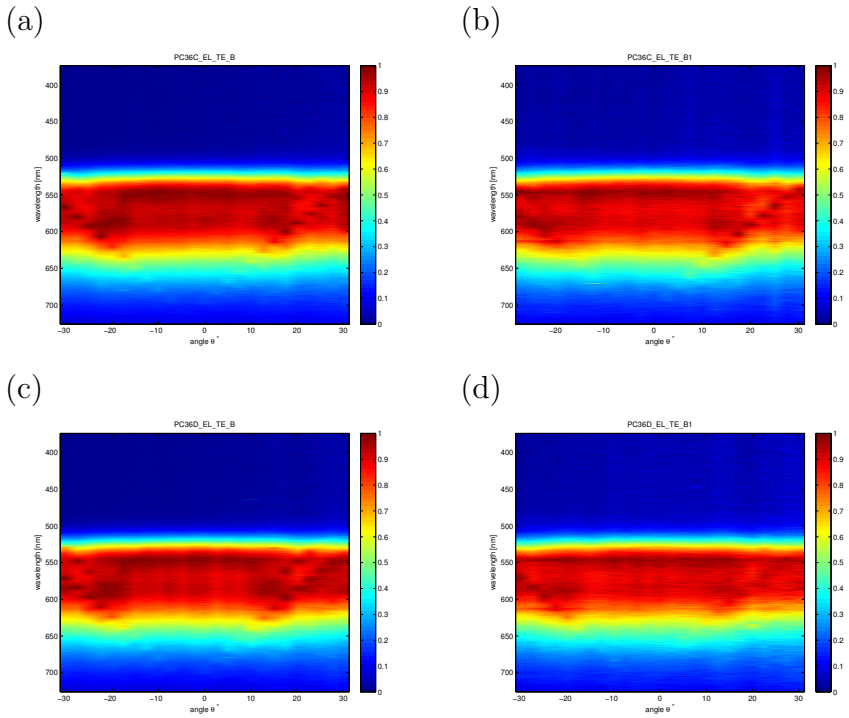

Figure C.22: Electroluminescence measurement with TE filter. Concave condition. a.) Δz = 2.16 mm, b.) Δz =1.7 mm, c.) Δz = 2.16 mm, and d.) Δz =1.7 mm.

C.12 Polycarbonate probe number 37

$\bigwedge$= 460 nm

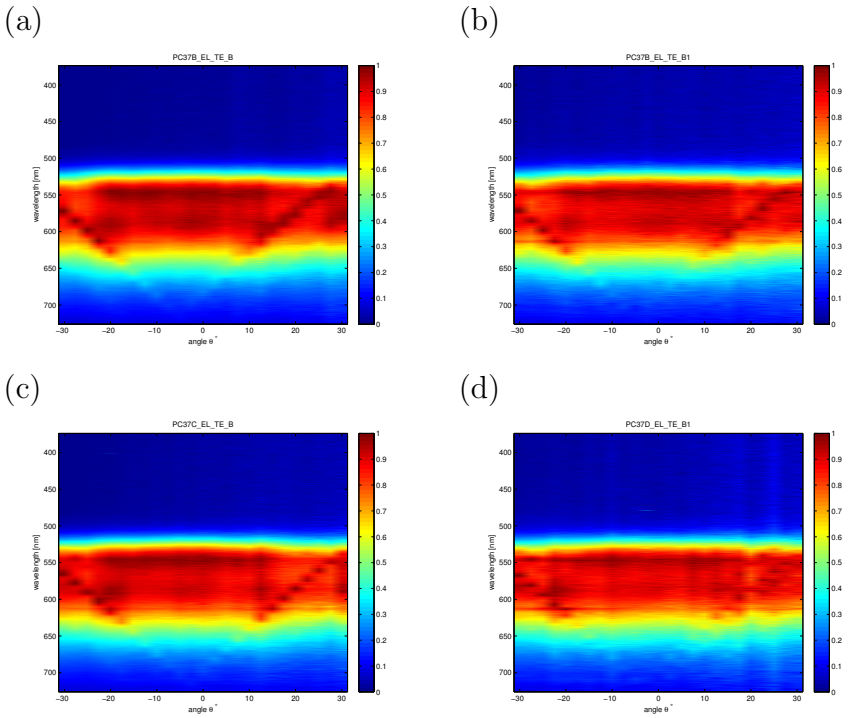

Figure C.23: Electroluminescence measurement with TE filter. Concave condition. a.) $\Delta z = 1.28$ mm, b.) $\Delta z = 1.68$ mm, c.) $\Delta z = 1.68$ mm, and d.) $\Delta z = 2.205$ mm.

C.13 Polycarbonate probe number 38

$\bigwedge$= 460 nm

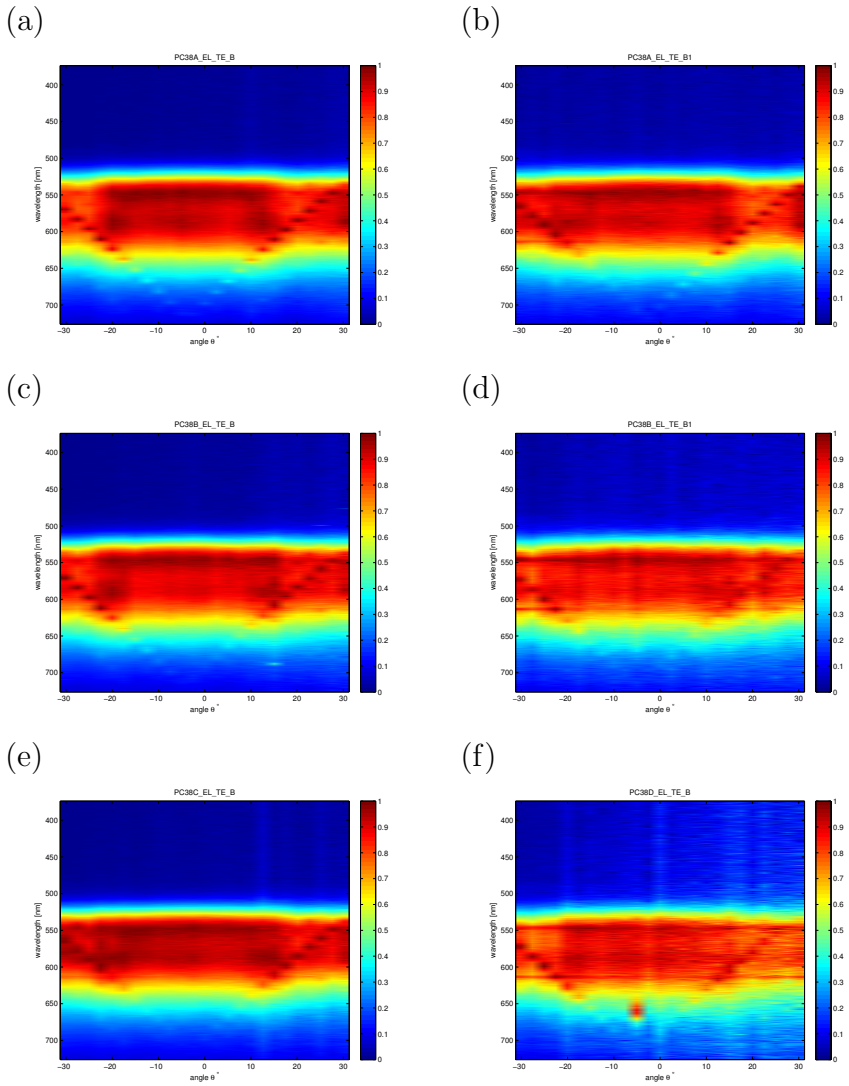

Figure C.24: Electroluminescence measurement with TE filter. Concave condition. a.) $\Delta z = 2.12$ mm, b.) $\Delta z = 1.72$ mm, c.) $\Delta z = 1.72$ mm, d.) $\Delta z = 1.56$ mm, e.) $\Delta z = 1.56$ mm, and f.) $\Delta z = 1.38$ mm.

C.14 Polycarbonate probe number 39

$\bigwedge$= 460 nm

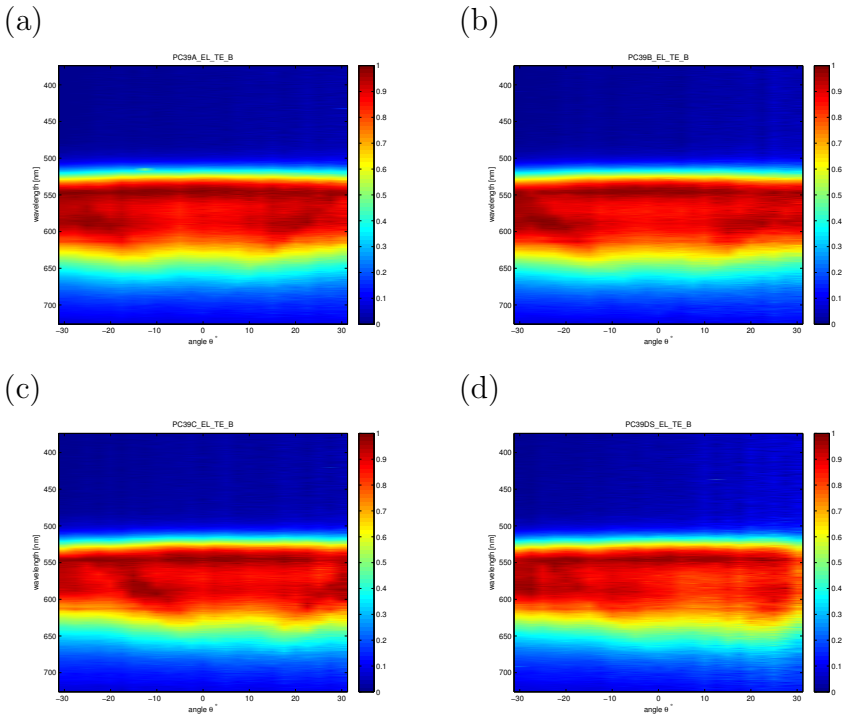

Figure C.25: Electroluminescence measurement with TE filter. Concave condition (Δz = 2.14 mm). Bend parallel to the gratings.

C.15 Polycarbonate probe number 40

$\bigwedge$= 460 nm

(a) (b)

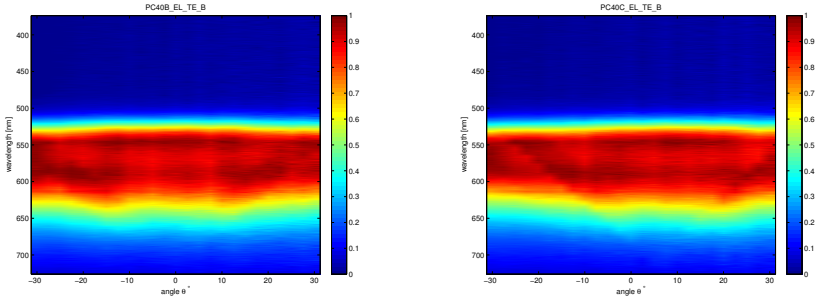

(c)

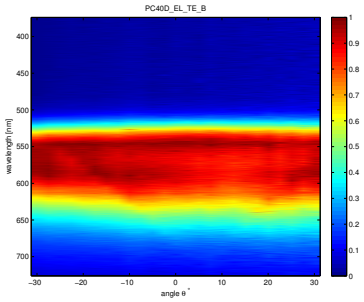

Figure C.26: Electroluminescence measurement with TE filter. Concave condition (Δz = 2.13 mm).

Appendix D

Photoluminescence measurements

D.1 Polycarbonate probe number 24

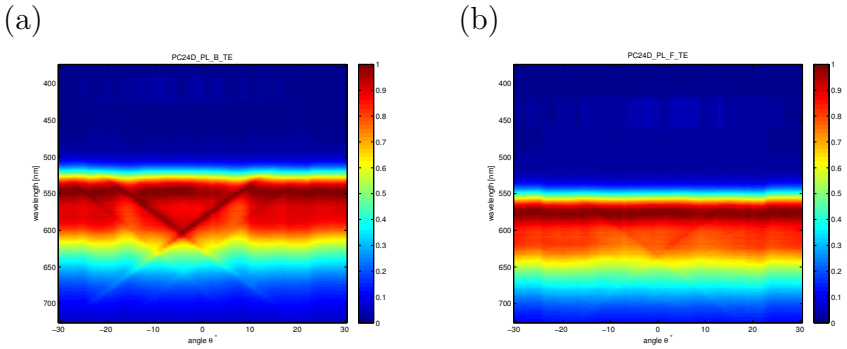

Figure D.1: Photoluminescence measurement with TE filter attached. Concave condition. a.) $\Delta z = 2.1$ mm and b.) $\Delta z = 0$.

D.2 Polycarbonate probe number 30

$\bigwedge$= 460 nm

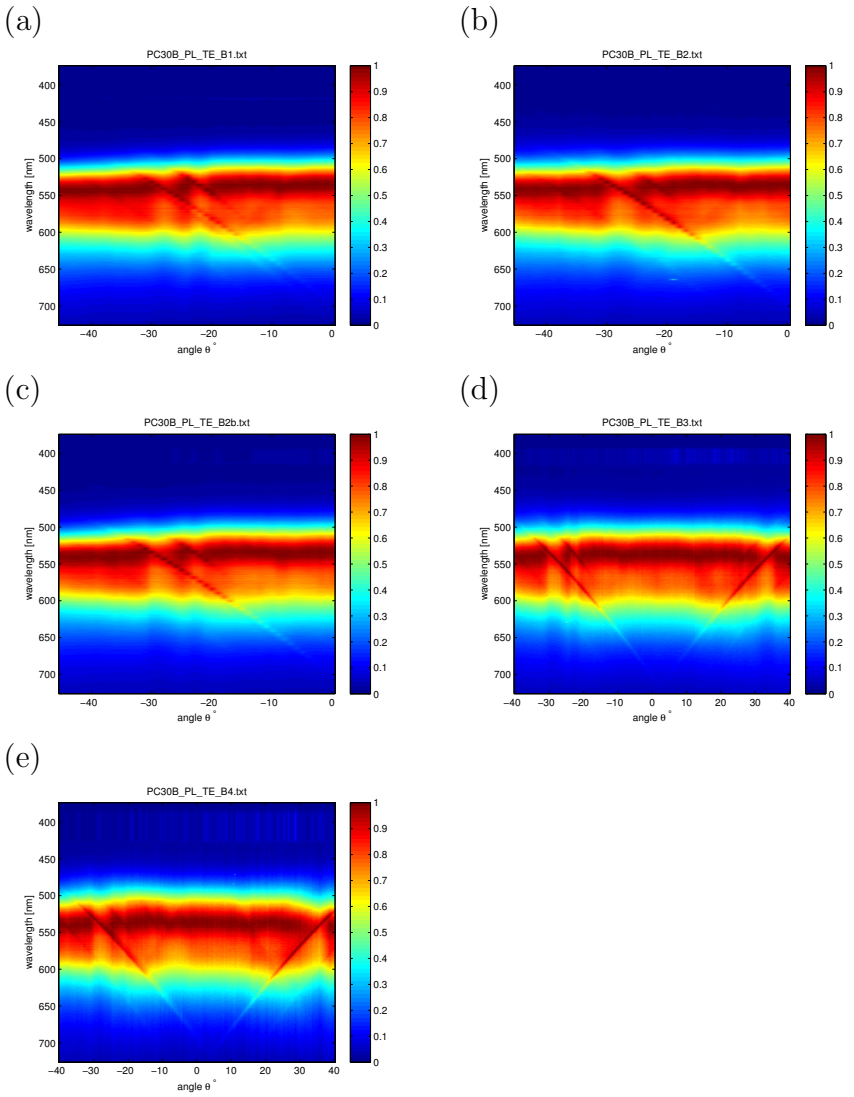

Figure D.2: Photoluminescence measurement with TE filter. Concave condition. a.) Δz = 2.12 mm, b.) Δz = 2.12 mm, c.) Δz = 1.51 mm, d.) Δz = 1.51 mm, and e.) Δz = 2.29 mm.

D.3 Polycarbonate probe number 31

$\bigwedge$= 460 nm

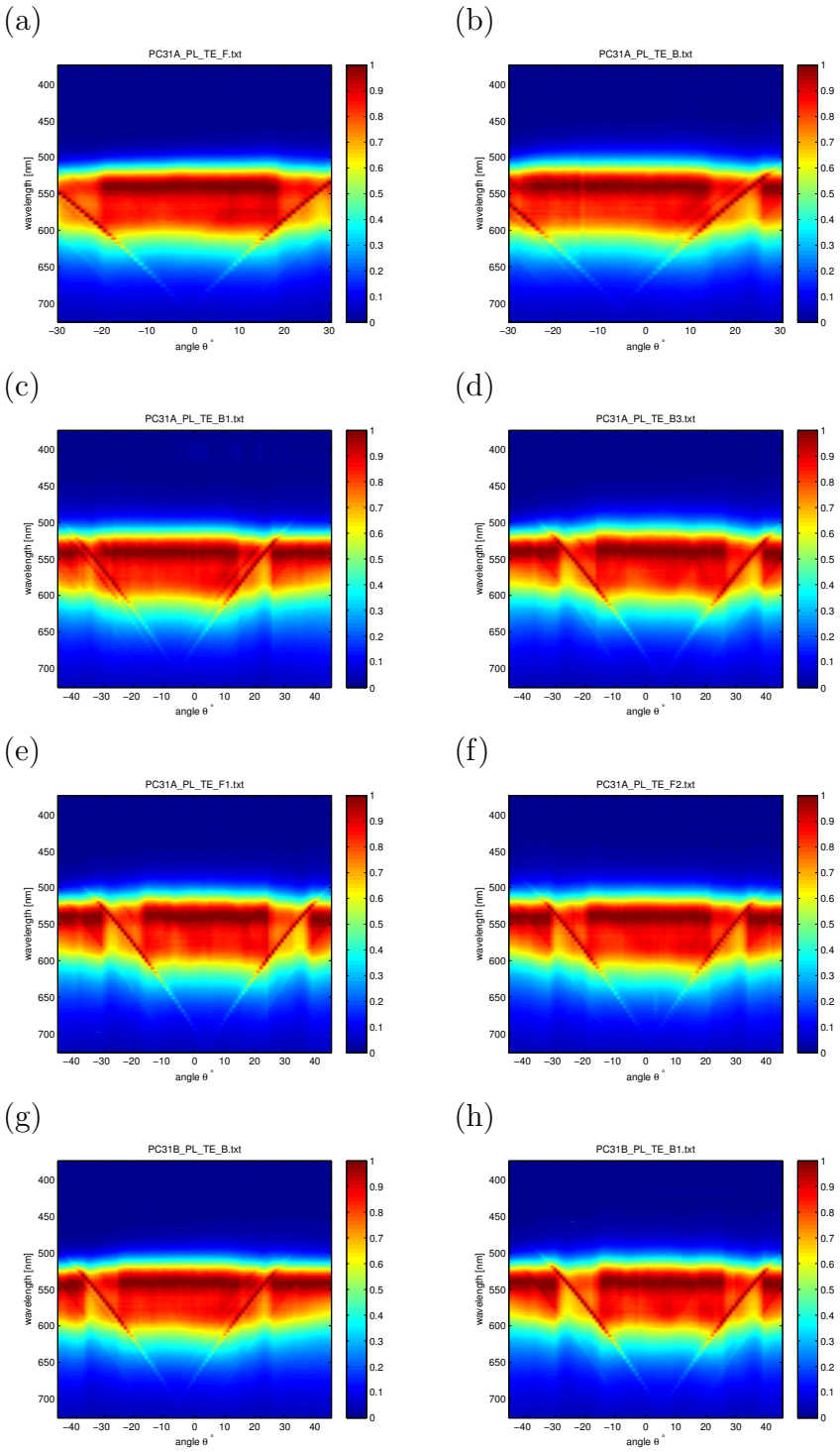

Figure D.3: Photoluminescence measurement with TE filter. Concave condition. a.) $\Delta z = 0$, b.) $\Delta z = 1.680$ mm, c.) $\Delta z = 1.680$ mm, d.) $\Delta z = 1.680$ mm, e.) $\Delta z = 0$, f.) $\Delta z = 0$), g.) $\Delta z = 1.680$ mm, and h.) $\Delta z = 1.680$ mm.

D.4 Polycarbonate probe number 37

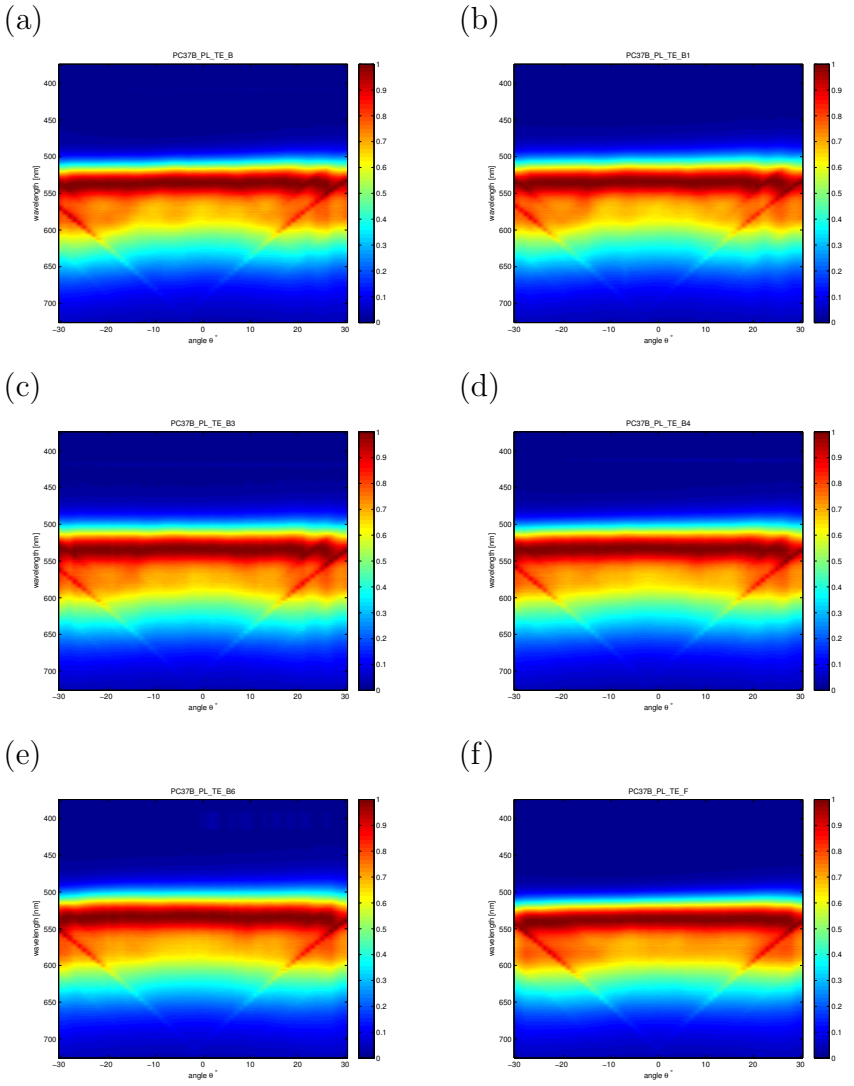

Figure D.4: Photoluminescence measurement with TE filter. Concave condition. a.) $\Delta z = 2.165$ mm, b.) $\Delta z = 2.01$ mm, c.) $\Delta z = 1.505$ mm, d.) $\Delta z = 1.23$ mm, e.) $\Delta z = 0.93$ mm, and d.) $\Delta z = 0$

D.5 Polycarbonate probe number 38

$\bigwedge$= 460 nm

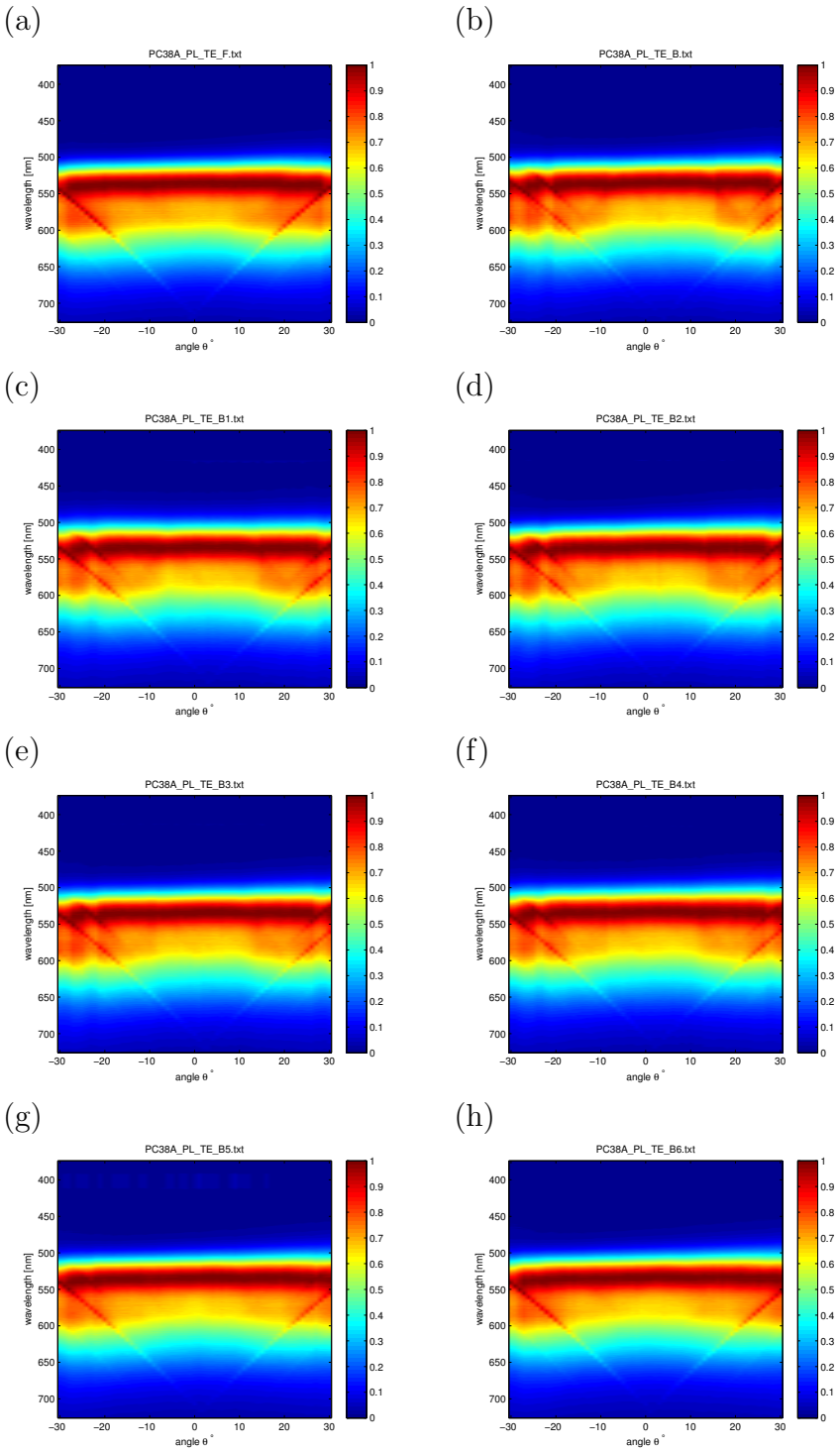

Figure D.5: Photoluminescence measurement with TE filter. Concave condition. a.) $\Delta z = 0$, b.) $\Delta z = 2.13$ mm, c.) $\Delta z = 2.035$ mm, d.) $\Delta z = 1.84$ mm, e.) $\Delta z = 1.66$ mm, f.) $\Delta z = 1.5$ mm, g.) $\Delta z = 1.33$ mm, and h.) $\Delta z = 1.14$ mm.

Bibliography

[1] Steven A. VanSlyke and Ching W. Tang. Organic electroluminescent devices having improved power conversion efficiencies, US Patent 4,539,507. 1985.

[2] Luiz Pereira, editor. *Organic Light-Emitting Diodes: The Use of Rare Earth and Transition Metals*. Pan Stanford Publishing Pte. Ltd., 2012.

[3] Joseph J. Shiang. Organic Light Emitting Devices for Lighting. *The Electrochemical Society Interface*, Winter:37–41, 2009.

[4] Sebastian Reineke, Frank Lindner, Gregor Schwartz, Nico Seidler, Karsten Walzer, Björn Lüssem, and Karl Leo. White organic light-emitting diodes with fluorescent tube efficiency. *Nature*, 459:234 – 238, 2009.

[5] Ulf Geyer, Julian Hauss, Boris Riedel, Sebastian Gleiss, Uli Lemmer, and Martina Gerken. Large-scale patterning of indium tin oxide electrodes for guided mode extraction from organic light-emitting diodes. *Journal of Applied Physics*, 104:093111, 2008.

[6] Boris Riedel, Julian Hauss, Ulf Geyer, Johanna Guetlein, Uli Lemmer, and Martina Gerken. Enhancing outcoupling efficiency of indium-tin-oxide-free organic light-emitting diodes via nanostructured high index layers. *Applied Physics Letters*, 96:243302, 2010.

[7] Marc J. Madou. *Fundamentals of Microfabrication and Nanotechnology.* CRC Press, Taylor and Francis Group, 2012.

[8] Hongbo Lan and Yucheng Ding. *Lithography.* InTech, 2010.

[9] Milton Ohring. *The Material Science of Thin Films.* Academic Press, 1992.

[10] Gernot Friedbacher and Henning Bubert, editors. *Surface and Thin Film Analysis.* Wiley-VCH Verlag GmbH & Co. KgaA, 2011.

[11] http://www.iap.tuwien.ac.at/www/atomic/instrumentation/afm.

[12] *Material Analysis Package for Autoprobe Operating Instruction.* Park Scientific Instruments, California USA, 1996.

[13] Tilo Peter. *Gas phase cluster aggregation and its application to the deposition of functional thin films.* PhD thesis, Christian-Albrechts-Universität zu Kiel, 2013.

[14] Tony Owen. *Fundamentals of UV-visible spectroscopy.* Hewlett-Packard Company, 1996.

[15] Wolfgang Brütting, editor. *Physics of Organic Semiconductors.* Wiley-VCH Verlag GmbH & Co. KgaA, 2005.

[16] Martin Klessinger and Josef Michl. *Excited States and Photochemistry of Organic Molecules.* VCH Publisher, Inc., 1995.

[17] M. A. Baldo, M. E. Thompson, and S. R. Forrest. Phosphorescent Materials for application to organic light emitting devices. *Pure Appl. Chem*, 71:2095–2106, 1999.

[18] Norman S. Allen, editor. *Photochemistry and Photophysics of Polymer Materials.* John Wiley and Sons, Inc, 2010.

[19] T. Förster. Transfer Mechanism of Electronic Excitation. *Disc. Faraday Soc.*, 27:7, 1959.

[20] D. L. Dexter. A Theory of Sensitized Luminescence in Solids. *Journal of Chemical Physics*, 21:836, 1953.

[21] Oleksandr Viktorovich Mikhnenko. *Dynamics of Singlet and Triplet Excitons in Organic Semiconductors.* PhD thesis, University of Groningen, the Netherlands, 2012.

[22] Hisao Ishii, Kiyoshi Sugiyama, Eisuke Ito, and Kazuhiko Seki. Energy Level Alignment and Interfacial Electronic Structures at Organic/Metal and Organic/Organic Interfaces. *Advanced Materials*, 11:605, 1999.

[23] L.S. Hung and C.H. CHen. Recent progress of molecular organic electroluminescenct materials and devices. *Materials Science & Engineering R*, 39:143–222, 2002.

[24] C. W. Tang and S. A. VanSlyke. Organic electroluminescent diodes. *Applied Physics Letters*, 51:913, 1987.

[25] Arno Kraft, Andrew C. Grimsdale, and Andrew B. Holmes. Electroluminescent Conjugated Polymers-Seeing Polymers in a New Light. *Angewandte Chemie, International Edition*, 37:402–428, 1998.

[26] Martin Grell and Donal D. C. Bradley. Polarized Luminescence from Oriented Molecular Materials. *Advanced Materials*, 11:895, 1999.

[27] R. H. Friend, R. W. Gymer, A. B. Holmes, J. H. Burroughes, R. N. Marks, C. Taliani, D. D. C. Bradley, D. A. Dos Santos, J. L. Bráedas, M. Lögdlund, and W. R. Salaneck. Electroluminescence in conjugated polymers. *Nature*, 397:121–128, 1999.

[28] Mukundan Thelakkat and Hans-Werner Schmidt. Low Molecular Weight and Polymeric Heterocyclics as Electron Transport/Hole-blocking Materials in Organic Light-emitting Diodes. *Polymers for Advanced Technologies*, 9:429–442, 1998.

[29] Tang C. W, S. A. VanSlyke, and C. H. Chen. Electroluminescence of doped organic thin films. *Journal Applied Physics*, 65:3610 – 3616, 1989.

[30] Jianmin Shi and C. W. Tang. Doped organic electroluminescent devices with improved stability. *Applied Physics Letters*, 70:1665, 1997.

[31] M. A. Baldo, M. E. Thompson, and S. R. Forrest. High-efficiency fluorescent organic light-emitting devices using a phosphorescent sensitizer. *Letters to nature*, 403:750, 2000.

[32] M. A. Baldo, D. F. O'Brien, Y. You, A. Shoustikov, S. Sibley, M. E. Thompson, and S. R. Forrest. Highly efficient phosphorescent emission from organic electroluminescent devices. *Letters to nature*, 395:151, 1998.

[33] D. F. O'Brien, M. A. Baldo, M. E. Thompson, and S. R. Forrest. Improved energy transfer in electrophosphorescent devices. *Applied Physics Letters*, 74:442, 1999.

[34] N. K. Patel, S. Cinà, and J. H. Burroughes. High-Efficiency Organic Light-Emitting Diodes. *IEEE Journal on Selected Topics in Quantum Electronics*, 8:346–361, 2002.

[35] J. S. Wilson, A. S. Dhoot, A. J. A. B. Seeley, M. S. Khan, A. Köhler, and R. H. Friend. Spin-dependent exciton formation in pi-conjugated compounds. *Nature*, 413:828, 2001.

[36] William R. Salaneck and Jean-Luc Brádas. The metal-on-polymer interface in polymer light emitting diodes. *Advanced Materials*, 8:48, 1996.

[37] M. Stoessel, G. Wittmann, J. Staudigel, F. Steuber, J. Blässing, W. Roth, H. Klausmann, W. Rogler, J. Simmerer, A. Winnacker, M. Inbasekaran, and E. P. Woo. Cathode-induced luminescence quenching in polyfluorenes. *Journal of Applied Physics*, 87:4467–4475, 2000.

[38] L. S. Hung, L. R. Zheng, and M. G. Mason. Anode modification in organic light-emitting diodes by low-frequency plasma polymerization of CHF_3. *Applied Physics Letters*, 78:673–675, 2001.

[39] D. J. Milliron, I. G. Hill, C. Shen, A. Kahn, and J. Schwartz. Surface oxidation activates indium tin oxide for hole injection. *Journal Applied Physics*, 87:572–576, 2000.

[40] A. J. Heeger, I. D. Parker, and Y. Yang. Carrier injection into semiconducting polymers: Fowler-Nordheim field-emission tunneling. *Synth. Met.*, 67:23–29, 1994.

[41] J.C. Scott, S.A. Carter, S. Karg, and M. Angelopoulos. Polymeric anodes for organic light-emitting diodes. *Synthetic Metals*, 85:1197, 1997.

[42] Michio Matsumura, Keiichi Furukawa, and Yukitoshi Jinde. Effect of Al/LiF Cathodes on emission efficiency of organic EL devices. *Thin Solid Films*, 331:96–100, 1998.

[43] Chihaya Adachi, Marc A. Baldo, Mark E. Thompson, and Stephen R. Forrest. Nearly 100% internal phosphorescence efficiency in an organic light-emitting device. *Journal of Applied Physics*, 90:5048, 2001.

[44] Chihaya Adachi, Marc A. Baldo, Stephen R. Forrest, Sergey Lamansky, and Mark E. Thompson. High-efficiency red electrophosphorescent devices. *Applied Physics Letters*, 78:1622, 2001.

[45] C. F. Madigan, M. H. Lu, and J. C. Sturm. Improvement of output coupling efficiency of organic light-emitting diodes by backside substrate modification. *Applied Physics Letters*, 76:1650, 2000.

[46] W. L. Barnes. Electromagnetic Crystals for Surface Plasmon Polaritons and the Extraction of Light from Emissive Devices. *Journal of Lightwave Technology*, 17:2170, 1999.

[47] M. H. Lu and J. C. Sturm. External coupling efficiency in planar organic light-emitting devices. *Applied Physics Letters*, 78:1927, 2001.

[48] Noriyuki Takada, Tetsuo Tsutsui, and Shogo Saito. Control of emission characteristics in organic thinfilm electroluminescent diodes using an opticalmicrocavity structure. *Applied Physics Letters*, 63:2032, 1993.

[49] Takahiro Nakayama, Yuzo Itoh, and Atsushi Kakuta. Organic photo and electroluminescent devices with double mirrors. *Applied Physics Letters*, 63:594, 1993.

[50] A. Dodabalapur, L. J. Rothberg, and T.M. Miller. Electroluminescence from organic semiconductors in patterned microcavities. *Electronics Letters*, 30:1000, 1994.

[51] U. Lemmer, R. Hennig, W. Guss, A. Ochse, and J. Pommerehne. Microcavity effects in a spincoated polymer twolayer system. *Applied Physics Letters*, 66:1301, 1995.

[52] M. Berggren, O. Inganäs, T. Granlund, S. Guo, Göran Gustafsson, and M. R. Andersson. Polymer light-emitting diodes placed in microcavities. *Synthetic Metals*, 76:121–123, 1996.

[53] R. H. Jordan, A. Dodabalapur, and R. E. Slusher. Efficiency enhancement of microcavity organic light emitting diodes. *Applied Physics Letters*, 69:1997, 1996.

[54] G. Gu, D. Z. Garbuzov, P. E. Burrows, S. Venkatesh, S. R. Forrest, and M. E. Thompson. High-external-quantum-efficiency organic light-emitting devices. *Optics Letters*, 22:396–398, 1997.

[55] Weixin Li, R. A. Jones, Steven C. Allen, J. C. Heikenfeld, and Andrew J. Steckl. Maximizing Alq/sub 3/ OLED internal and external efficiencies: charge balanced device structure and color conversion outcoupling lenses. *Journal of Display Technology*, 2:143, 2006.

[56] Toshitaka Nakamura, Naoto Tsutsumi, Noriyuki Juni, and Hironaka Fujii. Thinfilm waveguiding mode light extraction in organic electroluminescent device using high refractive index substrate. *Journal Applied Physics*, 97:054505, 2005.

[57] Brian W. D'Andrade and Julie J. Brown. Organic light-emitting device luminaire for illumination applications. *Applied Physics Letters*, 88:192908, 2006.

[58] Horst Greiner. Light Extraction from Organic Light Emitting Diode Substrates: Simulation and Experiment. *Japanese Journal of Applied Physics*, 46:4125–4137, 2007.

[59] Kanchan Saxena, V.K. Jain, and Dalip Singh Mehta. A review on the light extraction techniques in organic electroluminescent devices. *Optical Materials*, 32:221–33, 2009.

[60] Eli Yablonovitch. Inhibited Spontaneous Emission in Solid-State Physics and Electronics. *Physical Review Letters*, 58:2059–2062, 1987.

[61] E. Yablonovitch and T. J. Gmitter. Photonic Band Structure: The Face-Centered-Cubic Case. *Physical Review Letters*, 63:1950, 1989.

[62] John M. Lupton, Benjamin J. Matterson, Ifor D. W. Samuel, Michael J. Jory, and William L. Barnes. Bragg scattering from periodically microstructured light emitting diodes. *Applied Physics Letters*, 77:3340, 2000.

[63] Jonathan M. Ziebarth, Ameen K. Saafir, Shanhui Fan, and Michael D. McGehee. Extracting Light from Polymer Light-Emitting Diodes Using Stamped Bragg Gratings. *Advanced Functional Materials*, 14:451–456, 2004.

[64] Gregory P. Crawford, editor. *Flexible Flat Panel Displays*. John Wiley and Sons, Ltd, 2005.

[65] Y. Leterrier, L. Mdico, F. Demarco, J.-A.E. Mnson, M.F. Escol U. Betz, M. Kharrazi Olsson, and F. Atamny. Mechanical integrity of transparent conductive oxide films for flexible polymer-based displays. *Thin Solid Films*, 460:156–166, 2004.

[66] Y. Leterrier, C. Fischer, L. Mdico, F. Demarco, J.-A.E. Mnson, P. Bouten, J. DeGoede, and J.A. Nairn. Mechanical properties of transparent functional thin films for flexible displays. *Society of Vacuum Coaters*, 505:1–6, 2003.

[67] Jay Lewis, Sonia Grego, Erik Vick, Babu Chalamala, and Dorota Temple. Mechanical Performance of Thin Films in Flexible Displays. *Materials Research Society*, 814:189–198, 2004.

[68] Ralph Paetzold, Karsten Heuser, Debora Henseler, Stephan Roeger, and Georg Wittmann. Performance of flexible polymeric light-emitting diodes under bending conditions. *Applied Physics Letters*, 82:3342, 2003.

[69] Woohong Kim, Leonidas C. Palilis, Antti J. Mkinen, Heungsoo Kim, Manabu Uchida, and Zakya H. Kafafi. Polymer Electrodes for Flexible Organic Light-Emitting Devices. *Materials Research Society*, 814:343–353, 2004.

[70] G. Gustafsson, Y. Cao, G. M. Treacy, F. Klavetter, N. Colaneri, and A. J. Heeger. Flexible light emitting diodes made from soluble conducting polymers. *Nature*, 357:477–479, 1992.

[71] Zhiyuan Xie, Liang-Sun Hung, and Furong Zhu. A flexible top-emitting organic light-emitting diode on steel foil. *Chemical Physics Letters*, 381:691–696, 2003.

[72] Jin-Woo Park, Youngkyoo Kim, Hyuntaek Lim, Cheol Min Bae, Il Kim, Shinji Ando, and Chang-Sik Ha. Polyimide as a Plastic Substrate for the Flexible Organic Electroluminescent Device. *Materials Research Society*, 814:139–144, 2004.

[73] M. S. Weaver, L. A. Michalski, K. Rajan, M. A. Rothman, and J. A. Silvernail et al. Organic light-emitting devices with extended operating lifetimes on plastic substrates. *Applied Physics Letters*, 81:2929, 2002.

[74] Alexey N. Krasnov. High-contrast organic light-emitting diodes on flexible substrates. *Applied Physics Letters*, 80:3853, 2002.

[75] Sei-Yong Kim, Jeong-Hwan Lee, Jae-Hyun Lee, and Jang-Joo Kim. High contrast flexible organic light emitting diodes under ambient light without sacrificing luminous efficiency. *Organic Electronics*, 13:826–832, 2012.

[76] Yu-Hsuan Ho, Chung-Chun Liu, Shun-Wei Liu, Hsun Liang, Chih-Wei Chu, and Pei-Kuen Wei. Efficiency enhancement of flexible organic light-emitting devices by using antireflection nanopilars. *Optics Express*, 19:295–302, 2011.

[77] http://www.oled-info.com/flexible-oled.

[78] Boris Riedel. *Effizienzsteigerung in Organischen Leuchtdioden.* PhD thesis, Karlsruher Institut für Technologie (KIT), 2011.

[79] Peter A. Levermore, Rui Jin, Xuhua Wang, Lichun Chen, Donal D. C. Bradley, and John C. de Mello. High-Efficiency organic light-emitting diodes with PEDOT-based conducting polymer anodes. *Journal of Materials Chemistry*, 18:4414–4420, 2008.

[80] A. M. Nardes, M. Kemerink, M. M. de Kok, E. Vinken, K. Maturova, and R. A. J. Janssen. Conductivity, work function, and environmental stability of PEDOT:PSS thin films treated with sorbitol. *Organic Electronics*, 9:727–734, 2008.

[81] *Heraeus Clevios GmbH, database:Clevios PH500 (2013).*

[82] Karsten Fehse, Karsten Walzer, Karl Leo, Wilfried Lvenich, and Andreas Elschner. Highly Conductive Polymer Anodes as Replacements for Inorganic Materials in High-Efficiency Organic Light-Emitting Diodes. *Advanced Materials*, 19:441–444, 2007.

[83] Manisha Bajpai, Kusum Kumari, Ritu Srivastava, M.N. Kamalasanan, R.S. Tiwari, and Suresh Chand. Electric field and temperature dependence of hole mobility in electroluminescent PDY-132 polymer thin films. *Solid State Communications*, 150:581–584, 2010.

[84] Hubert Spreitzer, Heinrich Becker, Edgar Kluge, Willi Kreuder, Herman Schenk, Rob Demandt, and Herman Schoo. Soluble Phenyl-Substitude PPVs-New Materials for Highly Efficient Polymer LEDs. *Advanced Materials*, 10:1340, 1998.

[85] E.W. Snedden, L.A. Cury, K.N. Bourdakos, and A.P. Monkman. High photoluminescence quantum yield due to intramolecular energy transfer in the Super Yellow conjugated copolymer. *Chemical Physics Letters*, 490:76–79, 2010.

[86] L. S. Hung, C. W. Tang, and M. G. Manon. Enhanced electron injection in organic electroluminescence devices using an Al/LiF electrode. *Applied Physics Letters*, 70:152, 1997.

[87] Yu-Fan Chang, Chun-Yu Chen, Fang-Tsai Luo, Yu-Chiang Chao, Hsin-Fei Meng, Hsiao-Wen Zan, Hao-Wu Lin, Sheng-Fu Horng, Teng-Chih Chao, Han-Cheng Yeh, and Mei-Rurng Tseng. Vacuum-free lamination of low work function cathode for efficient solution-processed organic light-emitting diodes. *Organic Electronics*, 13:388–393, 2012.

[88] M. Hansen, M. Ziegler, H. Kohlstedt, A. Pradana, M. Raedler, and M. Gerken. Uv capillary force lithography for multiscale structures. *J. Vac. Sci. Technol. B,*, 30:3, 2012.

[89] Patrick Carlberg, Lars Montelius, and Jonas Tegenfeldt. Nanoimprint in PDMS on glass with two-level hybrid stamp. *Microelectronic Engineering*, 85:210–213, 2008.

[90] Jung-Gyu Lim, Sang-Shin Lee, and Ki-Dong Lee. Polymeric arrayed waveguide grating using imprint method incorporating a flexible PDMS stamp. *Optics Communications*, 272:97–101, 2007.

[91] Namil Koo, Markus Bender, Ulrich Plachetka, Andreas Fuchs, Thorsten Wahlbrink, Jens Bolten, and Heinrich Kurz. Improved mold fabrication for the definition of high quality nanopatterns by soft UV-nanoimprint lithography using diluted PDMS material. *Microelectronic Engineering*, 84:904–908, 2007.

[92] Jinook Kim, Mikyung Park, Gee Sung Chae, and In-Jae Chung. Influence of uncured PDMS chains in stamp using PDMS-based lithography. *Applied Surface Science*, 254:5266–5270, 2008.

[93] *Amonil MMS4, AMO GmbH, Germany.*

[94] T. D. Flaim, Yubao Wang, and Ramil Mercado. High Refractive Index Polymer Coatings for Optoelectronics Applications. *PROCEEDINGS OF SPIE: Advances in Optical Thin Films*, 5250:423, 2004.

[95] Helmut Schift. Nanoimprint lithography: An old story in modern times? A review. *Journal of Vacuum Science & Technology B*, 26:458, 2008.

[96] Ulrich Plachetka, Markus Bender, Andreas Fuchs, Thorsten Wahlbrink, Thomas Glinsner, and Heinrich Kurz. Comparison of multilayer stamp concepts in UV-NIL. *Microelectronic Engineering*, 83:944–947, 2006.

[97] Kaiqing Luo, Shuxue Zhou, and Limin Wu. High refractive index and good mechanical property UV-cured hybrid films containing zirconia nanoparticles. *Thin Solid Films*, 517:5974–5980, 2009.

[98] Yifei Liu, Changli L, Minjie Li, Liang Zhang, and Bai Yang. High refractive index organic-inorganic hybrid coatings with TiO_2 nanocrystals. *Colloids and Surfaces A: Physicochemical and Engineering Aspects*, 328:67–72, 2008.

[99] Yusuke Imai, Atsushi Terahara, Yukiya Hakuta, Keitaro Matsui, Hiromichi Hayashi, and Nobuhiko Ueno. Transparent poly(bisphenol a carbonate)-based nanocomposites with high refractive index nanoparticles. *European Polymer Journal*, 45:630–638, 2008.

[100] CHAO-CHING CHANG and WEN-CHANG CHEN. High refractive index thin films prepared from aminoalkoxysilane-capped pyromellitic dianhydride-titania hybrid materials. *Journal of Polymer Science: Part A: Polymer Chemistry*, 39:3419–3427, 2001.

[101] Bo-Tau Liu and Pei-Shan Li. Preparation and characterization of high-refractive-index polymer/inorganic hybrid films containing TiO_2 nanoparticles prepared by 4-aminobenzoic acid. *Surface & Coatings Technology*, 2012.

[102] Masayuki FUJITA, Kuniaki ISHIHARA, Tetsuyo UENO, Takashi ASANO, Susumu NODA, Hiroshi OHATA, Taishi TSUJI, Hitoshi NAKADA, and Noriyuki SHIMOJI. Optical and Electrical Characteristics of Organic Light-Emitting Diodes with Two-Dimensional Photonic Crystals in Organic/Electrode layers. *Japanese Journal of Applied Physics*, 44:3669–3677, 2005.

[103] Diana Mardare and Peter Hones. Optical dispersion analysis of TiO_2 thin films based on variable-angle spectroscopic ellipsometry measurements. *Material Science and Engineering B*, 68:42–47, 1999.

[104] Sea-Fue Wang, Yung-Fu Hsu, and Yi-Shiang Lee. Microstructural evolution and optical properties of doped TiO_2 films prepared by RF magnetron sputtering. *Ceramics Internationals*, 32:121–125, 2006.

[105] R Swanepoel. Determination of the thickness and optical constants of amorphous silicon. *Journal of Physics E: Scientific Instruments*, 16:1214, 1983.

[106] Ginés Lifante, editor. *Integrated Photonics: Fundamentals*. Wiley, 2003.

[107] Dietmar Gross, Werner Hauger, Jörg Schröder, Wolfgang A. Wall, and Javier Bonet. *Engineering Mechanics 2*. Springer, 2010.

[108] http://refractiveindex.info/.

[109] B. Gruska and S. Peters. Organic Light Emitting Diodes. Technical report, Sentech Application Bulletin.

[110] Michael Vosgueritchian, Darren J. Lipomi, and Zhenan Bao. Highly Conductive and Transparent PEDOT:PSS Films with a Fluorosurfactant for Stretchable and Flexible Transparent Electrodes. *Advanced Functional Materials*, 22:421–428, 2012.

[111] Jiajie Liang, Lu Li, Xiaofan Niu, Zhibin Yu, and Qibing Pei. Elastomeric polymer light-emitting devices and displays. *Nature Photonics*, 7:817–824, 2013.

Eidesstattliche Erklärung

Die Dissertation in vierfacher Ausfertigung, in die eine unterschriebene Erklärung eingebunden ist, die folgende Angaben enthält:

1. dass die Abhandlung, abgesehen von der Beratung durch die Betreuerin oder den Betreuer, nach Inhalt und Form die eigene Arbeit ist;

2. ob die Arbeit ganz oder zum Teil schon einer anderen Stelle im Rahmen eines Prüfungsverfahrens vorgelegen hat, veröffentlicht worden ist oder zur Veröffentlichung eingereicht wurde;

3. dass die Arbeit unter Einhaltung der Regeln guter wissenschaftlicher Praxis der Deutschen Forschungsgemeinschaft entstanden ist.

.

Kiel, am Mai 2014

(Arfat Pradana)